

Diffuse correlation spectroscopy for tissue blood flow assessment: methodological advancements and MRI based validation

By

Neda Mogharari

Submitted to

Nalecz Institute of Biocybernetics and Biomedical Engineering

of the

Polish Academy of Sciences

for the degree of Doctor of Technical Sciences

in the discipline of biomedical engineering

April 2026

Supervised by:

Prof. Adam Liebert

Thesis supervisor

Dr. Michal Kacprzak

Thesis auxiliary supervisor

Contents

Abstract (Polish) v

Abstract (English) ix

Publications xi

List of Acronyms xiii

List of Figures xvii

1 Introduction 1

1.1 Context 1

1.2 Research gaps, aims and hypothesis 6

1.3 Thesis outline 7

2 Methods 9

2.1 Basics of tissue optics 9

2.1.1 Photon Propagation in Tissue 9

2.1.2 Time domain near infrared spectroscopy 10

2.1.3 Diffuse correlation spectroscopy 14

2.2 Instrumentation 21

2.3 Data acquisition 24

2.3.1 Optical data acquisition 24

2.3.2 MRI data acquisition 28

2.4 Experimental protocols 29

2.4.1 Physical phantom 29

2.4.2 In vivo experiments protocol 33

2.5 Data analysis approaches 40

2.5.1 Derivation of optical properties 40

2.5.2 DCS techniques 41

2.5.3 Blood Oxygenation Level-Dependent MRI 48

2.5.4 Intravoxel Incoherent Motion MRI 50

2.5.5 Cross-analysis of the signals obtained by DCS, BOLD-MRI and IVIM-MRI 52

3 Results 55

3.1 Comparison of td-DCS performance at shorter and larger SDSs 55
3.2 Correlation of Hemodynamic Responses Measured by DCS and BOLD-MRI..... 77
3.3 Cross evaluation of IVIM-MRI and DCS in measuring tissue perfusion/blood flow 93
4 Discussions and conclusions 101
4.1 Discussions 101
4.2 Conclusions..... 111

Abstract (Polish)

Przepływ krwi jest uznawany za istotny biomarker stanu zdrowia oraz prawidłowego funkcjonowania narządów. Nieinwazyjne techniki umożliwiające jego pomiar mają kluczowe znaczenie w wielu zastosowaniach klinicznych. Dyfuzyjna spektroskopia korelacyjna (ang. Diffuse Correlation Spectroscopy, DCS) stanowi nieinwazyjną metodę optyczną służącą do monitorowania zmian przepływu krwi w tkankach. Umożliwia ona ocenę przepływu krwi na podstawie analizy czasowych fluktuacji plamek interferencyjnych (speckle) światła koherentnego, wywołanych ruchem erytrocytów.

Dyfuzyjna spektroskopia korelacyjna (DCS) obejmuje technikę fali ciągłej (continuous-wave DCS, cw-DCS) oraz technikę czasowo-rozdzielczą (time-domain DCS, td-DCS). cw-DCS jest metodą starszą, dobrze ugruntowaną i szeroko stosowaną zarówno w badaniach prowadzonych u osób zdrowych, jak i w zastosowaniach klinicznych u pacjentów. Jej istotnym ograniczeniem pozostaje jednak brak możliwości rozróżnienia zmian przepływu krwi zachodzących w warstwach powierzchownych i głębszych badanych tkanek. W ostatnich latach coraz większą uwagę poświęca się rozwojowi techniki td-DCS, która dzięki wykorzystaniu szybkiej optoelektroniki oraz laserów impulsowych umożliwia różnicowanie rejestrowanych fotonów na podstawie czasu ich przelotu (ang. Time of Flight, TOF), a tym samym pośrednie szacowanie głębokości penetracji światła w tkance. Pozwala to na lepsze rozróżnienie zmian przepływu krwi zachodzących na różnych głębokościach badanej tkanki. Jednocześnie istotnym wyzwaniem w pomiarach td-DCS pozostaje uzyskanie odpowiednio wysokiego stosunku sygnału do szumu, ponieważ analiza opiera się na fotonach rejestrowanych wyłącznie w ściśle określonych oknach czasowych. Analiza danych w td-DCS jest zatem bardziej złożona, a konfiguracja eksperymentalna znacznie kosztowniejsza niż w przypadku cw-DCS.

1. Zwiększenie odległości źródło-detektor (SDS) poprawia czułość czasowo-rozdzielczej dyfuzyjnej spektroskopii korelacyjnej (td-DCS) w monitorowaniu zmian przepływu krwi zachodzących w głębszych warstwach tkanek.

2. Odpowiedzi hemodynamiczne mierzone techniką DCS wykazują dobrą korelację z odpowiedziami uzyskiwanymi metodami opartymi na rezonansie magnetycznym (MRI), co

wskazuje na możliwość wykorzystania DCS jako narzędzia optycznego do oceny zmian przepływu krwi w mikrokrążeniu.

W pierwszej części pracy oceniono wydajność techniki td-DCS przy mniejszych i większych odległościach od źródła do detektora (SDS) w monitorowaniu zmian przepływu krwi zachodzących w głębszych warstwach tkanek. W tym celu zastosowano metryki jakości, takie jak współczynnik zmienności oraz stosunek kontrastu do szumu, w celu wyznaczenia optymalnego czasu przelotu fotonów (TOF) do estymacji zmian dynamiki rozpraszaczy w badanym medium. Następnie zdefiniowano metryki czułości służące ocenie zdolności td-DCS do wykrywania zmian ruchu rozpraszaczy w warstwach powierzchownych i głębokich z wykorzystaniem fantomów dwuwarstwowych. W dalszej części, w celu oceny zdolności td-DCS do monitorowania wskaźnika przepływu krwi (BFI), przeprowadzono serię testów obejmujących okluzję przedramienia oraz próby oddechowe, tj. wstrzymanie oddechu (BH) i hiperwentylację (HV), u zdrowych dorosłych ochotników. Uzyskane wyniki stanowią podstawę opracowania metodologii i optymalizacji konfiguracji eksperymentalnej td-DCS oraz opracowania metod analizy danych.

W drugiej części pracy oceniono korelację odpowiedzi hemodynamicznych rejestrowanych na głowie człowieka za pomocą technik cw-DCS i td-DCS z sygnałem zależnym od poziomu utlenowania krwi (*blood oxygen level-dependent*, BOLD) w obrazowaniu metodą rezonansu magnetycznego (MRI). Zaobserwowano dodatnią korelację pomiędzy wartościami wskaźnika przepływu krwi (BFI) a zmianami sygnału BOLD w odpowiedzi na próby oddechowe, tj. wstrzymanie oddechu (BH) i hiperwentylację (HV). Analiza pętli histerezy pomiędzy BFI a sygnałem BOLD podczas tych prób ujawniła wyraźne zależności czasowe między zmianami przepływu krwi a zmianami poziomu utlenowania. Wyniki te potwierdzają potencjał techniki DCS w monitorowaniu zmian mózgowego przepływu krwi (CBF) z wysoką rozdzielczością czasową. Ponadto wskazują, że DCS może stanowić narzędzie komplementarne względem BOLD-MRI w ocenie hemodynamiki mózgowej, w tym parametrów metabolicznych, takich jak mózgowy wskaźnik zużycia tlenu ($CMRO_2$).

W trzeciej części pracy przeprowadzono porównawczą ocenę perfuzji w mikrokrążeniu tkanek. Zastosowano metodę IVIM MRI (ang. *intravoxel incoherent motion*, IVIM), umożliwiającą ocenę dyfuzji i składowej perfuzyjnej sygnału MR oraz wskaźnika przepływu krwi (BFI) mierzonego metodą cw-DCS. Perfuzja w mikrokrążeniu wyznaczana metodą IVIM opiera się

na analizie średniokwadratowego przemieszczenia cząsteczek wody w czasie. Z kolei BFI mierzony metodą cw-DCS jest proporcjonalny do średniokwadratowego przemieszczenia erytrocytów w czasie, co stwarza potencjalną możliwość bezpośredniego porównania obu metod. Nie zaobserwowano jednak korelacji pomiędzy BFI mierzonym metodą cw-DCS a parametrami perfuzji mikrokrążeniowej wyznaczonymi metodą IVIM-MRI podczas testów okluzji kończyn, obejmujących przedramię i kończynę dolną, co można wiązać z dużym błędem estymacji tych parametrów. Wskazuje to, że ograniczona dokładność metody IVIM-MRI w ilościowej ocenie perfuzji mikrokrążeniowej może istotnie ograniczać jej zastosowanie kliniczne. Jednocześnie w badaniach przeprowadzonych z wykorzystaniem fantomów tkanko-podobnych zaobserwowano dodatnią korelację pomiędzy wskaźnikiem przepływu mierzonym metodą cw-DCS a parametrem perfuzji wyznaczonym metodą IVIM-MRI.

Wyniki przedstawione w niniejszej rozprawie wpisują się w rozwój techniki DCS, szczególnie w jej czasowo-rozdzielczą, nowoczesną odmianę. Uzyskane rezultaty przyczyniają się do poszerzenia możliwości zastosowania tej metody w monitorowaniu zmian przepływu krwi w mikrokrążeniu.

Abstract (English)

Blood flow is considered as an important biomarker of organ health and function. Noninvasive technologies that measure blood flow are essential in many clinical applications. Diffuse correlation spectroscopy (DCS) is a noninvasive optical technique to monitor tissue blood flow changes. This technique monitors the tissues blood flow changes by evaluating the temporal speckle fluctuations of the coherent light caused by displacement of the red blood cells (RBC) in time. DCS is applied in a reflectance geometry with a source-detector separation (SDS) of few centimeters.

DCS is classified as continuous wave DCS (cw-DCS) and time-domain DCS (td-DCS). cw-DCS is a more common technique, to monitor tissue blood flow changes. However, this technique does not provide depth discrimination of the blood flow of superficial and deeper layers of tissue. Although some improvements over data analyses and experimental setup has been suggested, such improvements increase the complication and the cost of using this technique. td-DCS technique allows differentiation of the detected photons based on their time-of-flight (TOF) and pathlength through the tissue, enabling depth discrimination of blood flow changes across tissue layers. However, the data analysis of this technique is more complex, and the experimental setup is costlier compared to cw-DCS.

Two hypotheses were formulated for this dissertation.

1) Increasing the source detector separation improves the sensitivity of time domain DCS to monitor blood flow changes appearing in deeper tissue layers.
2) Hemodynamic responses measured by DCS technique correlate well with those measured by MRI-based techniques, allowing DCS to serve as an optical tool for assessing microvascular blood flow changes.

In first part of this study, the performance of td-DCS at shorter and larger SDS, to monitor blood flow changes appearing in deeper tissue layers were evaluated. To do that, quality metrics such as coefficient of variation and contrast-to-noise ratio were employed to identify the optimal TOF to estimate the changes in displacement of scatterers. Subsequently, sensitivity metrics were defined to evaluate the performance of td-DCS to assess the changes in displacements of scatterers in superficial and deeper layers of the two-layered phantoms. Then to evaluate the performance of td-DCS in monitoring BFI, series of forearm occlusion test as well as breath hold (BH) and hyperventilation (HV) respiratory challenges were performed by

healthy adult volunteers. These findings can provide a comprehensive methodology to optimize the td-DCS experimental set up and data analayses.

In the second part of the study, the correlation of the hemodynamic responses measured on the human head by cw-DCS and td-DCS modalities with blood oxygenation level–dependent (BOLD) magnetic resonance imaging (MRI) were evaluated. I observed positive correlations between the BFIs and BOLD signal changes in response to BH and HV respiratory challenges. The hysteresis loops between the BFI and BOLD signal during respiratory challenges revealed distinct temporal relationships between the blood flow and blood oxygenation level changes. These results support the potential of DCS technique to monitor CBF changes with good temporal resolution. Moreover, the results suggest that DCS can be served as a complementary tool to BOLD-MRI for assessing cerebral hemodynamics (e.g. $CMRO_2$).

In third part of this study, the microvascular perfusion-related measured by intravoxel incoherent motion (IVIM) MRI and BFI measured by cw-DCS were cross evaluated. The IVIM-derived microvascular perfusion-related is measured based on the mean square displacement of water molecules in time. The BFI measured by cw-DCS is proportional to mean square displacement of the red blood cells in time, which provides a potential for direct cross evaluation with the microvascular perfusion-related motion measured by IVIM-MRI. No correlation was observed between the BFI measured by cw-DCS and the microvascular perfusion-related motion parameters measured by IVIM-MRI during leg and forearm occlusion test, due to the high error in the estimation of the latest parameter. Thus, the misestimation of IVIM-MRI technique to quantify the microvascular perfusion-related motion may limits its clinical application. However, I observed positive correlation between the flow index measured by cw-DCS and perfusion-related motion parameter measured by IVIM-MRI on tissue mimicking phantom.

The work presented in this thesis lays on the continued development of DCS technique. The findings of this study contribute to enhancing DCS applicability in monitoring the microvascular blood flow changes.

Publications

Articles:

1) **Neda Mogharari**, Stanisław Wojtkiewicz, Dawid Borycki, Adam Liebert, and Michał Kacprzak, “Time-domain diffuse correlation spectroscopy at large source detector separation for cerebral blood flow recovery”, Biomedical Optics Express Vol. 15, Issue 7, pp. 4330-4344 (2024). Published.
2) **Neda Mogharari**, Michał Kacprzak, Kamil Lipinski, Adam Liebert, and Stanisław Wojtkiewicz, “Correlation of Hemodynamic Responses Measured on Human Head by Diffuse Correlation Spectroscopy and BOLD MRI”, IEEE Journal of Selected Topics in Quantum Electronics, Vol: 31 Issue: 4: Adv. in Neurophotonic. for Non-Inv. Brain Mon, (2025). Published.
3) **Neda Mogharari**, Kamil Lipinski, Stanislaw Wojtkiewicz, Adam Liebert, and Michał Kacprzak, “Cross evaluation of IVIM-MRI based tissue perfusion-related motion with blood flow index measured with diffusion correlation spectroscopy”, To be submitted.

Conference Proceedings

1) **Neda Mogharari**, Saeed Samaei, Stanislaw Jutkiewicz, Adam Liebert, Michał Kacprzak, “Hybrid diffuse optical system for the tissue perfusion and oxygenation assessment”, Polish Conference on Biocybernetics and Biomedical Engineering, 19-21 May 2021, Warsaw, Poland, Online. Poster presenter: Neda Mogharari.
2) Saeed Samaei, **Neda Mogharari**, Dawid Borycki, Adam Liebert, Michał Kacprzak, “Noninvasive brain perfusion assessment with combined use of time-domain diffuse correlation spectroscopy and time-domain near-infrared spectroscopy”, Polish Conference on Biocybernetics and Biomedical Engineering, 19-21 May 2021, Warsaw, Poland, Online. Coauthor.
3) Saeed Samaei, **Neda Mogharari**, Dawid Borycki, Adam Liebert, Michał Kacprzak, “New Hybrid Time-domain Device for Diffuse Correlation Spectroscopy and Near-

infrared Spectroscopy for Brain Hemodynamic Assessment", European Conferences on Biomedical Optics, 21-24 June 2021, Munich, Germany, Online. Coauthor.

4) **Neda Mogharari**, Saeed Samaei, Stanislaw Wojtkiewicz, Adam Liebert, Michal Kacprzak "Characterization of a physical liquid phantom using hybrid diffuse optical system" Functional near infrared spectroscopy conference fNIRS, October 18-22, 2021, Online. Oral presenter: Neda Mogharari.
5) **Neda Mogharari**, Saeed Samaei, Stanislaw Wojtkiewicz, Adam Liebert, Michal Kacprzak, "Time-domain diffuse correlation spectroscopy performance at different source-detector separation", European Conferences on Biomedical Optics, 21-24 June 2023, Munich, Germany. Oral presenter: Neda Mogharari.
6) **Neda Mogharari**, Stanislaw Wojtkiewicz, Adam Liebert, Michal Kacprzak, "Hemodynamic changes measured using time domain diffuse correlation spectroscopy during Valsalva maneuver on healthy subjects". Polish Conference on Biocybernetics and Biomedical Engineering, September 2023, Lodz, Poland. Poster presenter: Neda Mogharari.
7) **Neda Mogharari**, Kamil Lipinski, Adam Liebert, Stanislaw Wojtkiewicz, Michał Kacprzak "Cross evaluation of diffuse correlation spectroscopy and intravoxel incoherent motion MRI in measuring tissue blood flow", Polish Conference on Biocybernetics and Biomedical Engineering, June 2025, Warsaw, Poland. Oral presenter: Neda Mogharari.

List of Acronyms

ASL-MRI: Arterial-Spin-Labelled Magnetic Resonance Imaging

BFI: Blood flow Index

BE: Beam Expander

BH: Breath Hold

BOLD: Blood-Oxygenation-Level-Dependent

CBF: Cerebral Blood Flow

CBV: Cerebral Blood Volume

$CMRO_2$: Cerebral Metabolic Rate of Oxygen

CNR: Contrast-to-Noise Ratio

CV: Coefficient of Variation

CW: Continuous Wave

CSF: Cerebrospinal Fluid

DCS: Diffuse Correlation Spectroscopy

DL: Deep layer

DOS: Diffuse Optical Spectroscopy

DTOF: Distribution of Time of Flights

DWI: Diffusing Weighting Imaging

FOV: Field Of View

FWHM: Full width at half-maximum

Hb: Deoxy Hemoglobin

HbO2: Oxy Hemoglobin

HV: Hyperventilation

IRF: Instrument Response Function

IVIM: Intravoxel Incoherent Motion

MM: Multi Mode

MSD: Mean Squared Displacement

MRI: Magnetic Resonance Imaging

NIRS: Near Infrared Spectroscopy

NA: Numerical Aperture

ND: Natural Density

RBC: Red blood Cells

rBFI: Relative Blood Flow Index

SDS: Source Detector Separation

SL: Superficial Layer

SM: Single Mode Fiber

SNR: Signal to Noise Ratio

SPAD: Single Photon Avalanche Diode

SpO2: Peripheral oxygen saturation

TCSPC: Time Correlated Single Photon Counting

td-DCS: Time Domain Diffuse Correlation Spectroscopy

td-NIRS: Time Domain Near Infrared Spectroscopy

TE: Echo Time

TOF: Time Of Flight

TR: Repetition Time

S: Power distribution

φ: Fluence function of the radiation source

P: Normalized path length distribution of photons propagating trough the medium

l_{tr}: Transport mean free path of photons

g: Anisotropy factor

v: Speed of light in a medium

c: Speed of light in vacuum

I: Light intensity

λ: Wavelength

R_{eff}: Effective Fresnel reflection coefficient

μ_{s}'= Reduced scattering coefficient

μ_{a}: Absorption coefficient

D: Diffusion coefficient in solution of diffusion equations

D_b: Diffusion coefficient of scatterers derived by DCS

D_B: Diffusion coefficient of water molecules in a solution

D_{slow}: Diffusion coefficient of Brownian-related motion of water molecules in extravascular structure of tissue derived by IVIM-MRI

D_{fast}: Pseudo-diffusion coefficient referring to microvascular perfusion-related motion in intravascular structure of tissue derived by IVIM-MRI

t: Absolute arrival time

t_s: Time of flight

n: The refractive index of a medium

g_2: Intensity autocorrelation function

g_1: Electric fielded autocorrelation function

β: Coherence parameter

α: Fraction of moving scatterers to total number of scatterers

F_{pump}: Pump flow rates

A_{cs}: Cross-sectional area of the tube

V_{pump}: Pump velocity respectively

f: Perfusion fraction derived by IVIM-MRI

r: Pearson correlation coefficient

BFI_{DCS}: Blood flow index derived by cw-DCS

FI_{DCS}: Flow index derived by cw-DCS

BF_{IVIM}: Blood flow derived by IVIM-MRI

F_{IVIM}: Flow derived by IVIM-MRI

List of Figures

Figure 1.1 Schematics of diffuse light measurement in reflectance geometry, where a laser source is used to illuminate the tissue, and the scattered light is detected a few centimetres away from the fiber tip of the laser source. The colorbar present the photon counts. The figure was obtained using NIRfast package for a turbid medium, where the distance between the source and detector is 2 cm. The optical properties of tissue was considered to be $\mu_a = 0.01\ cm - 1$and $\mu_s' = 1\ cm - 1$ [16]. 3
Figure 1.2 Schematics of simplified model of different layers of a) tissue muscle and b) human head. The figures were modified from https://www.gettyimages.com/. 4
Figure 2.1 Photons trajectories between source and detector in a highly scattering medium forms a banana-shaped sensitivity profile. When photons propagate through the tissue, some are absorbed (see events in red circles) and some undergo multiple scattering events. Black circles mark scatterers and green circles mark absorbers. 10
Figure 2.2 The schematic of extrapolated boundary model for photon diffusion in semi-infinite geometry [58]. 12
Figure 2.3 a) A narrow Gaussian profile laser pulse (FWHM of 0.1 ns) (red), and the DTOF curve in diffuse reflectance geometry (blue), describing the number of detected photons as a function of their travel time through the tissue (SDS=5 mm, μ_a = 0.08 mm^{-1},μ_s' = 0.8 mm^{-1}). b) DTOFs for varying SDS = 10–30 mm, in 5 mm increments with a fixed absorption coefficient (μ_a = 0.1 mm^{-1}) and reduced scattering coefficient (μ_s' = 1.0 mm^{-1}). c) DTOFs at a fixed SDS (15 mm) and fixed reduced scattering coefficient (μ_s' = 1.0 mm^{-1}) for varying absorption coefficients (μ_a = 0.08–0.12 mm^{-1}, in increments of 0.01 mm^{-1}). d) DTOFs at a fixed SDS (15 mm) and fixed absorption coefficient (μ_a = 0.01 mm^{-1}) for varying reduced scattering coefficients (μ_s' = 0.8–1.2 mm^{-1}, in increments of 0.1 mm^{-1}). The DTOF curves have been calculated using NIRFAST 9.1 [16]. 14
Figure 2.4 The displacement of scatterers causes fluctuations of the scattered light over time t or so-called speckle pattern. The blue circle is considered as the position of the single mode detection fiber's tip which collects the scattered photons. 15
Figure 2.5 a) Photon trajectories between source and detection points in a two-layered highly scattering medium forms a banana-shaped sensitivity profile. The solid and dashed red arrows present the scattered photon's path at time t and $t + \tau$, respectively. The green arrows present

the displacements of scatterers between time t and $t + \tau$. The blue and green dots present the scatterers at time t and $t + \tau$, respectively. b) The light intensity fluctuations detected from a continuous wave laser contained scattered photons from both superficial and deeper layers. c) The intensity autocorrelation function g_2 calculated from theory (black solid line) is fitted to g_2 calculated from the photons that travelled different path through the medium (orange circle marks) to estimate the mean squared displacement of scatterers in time..... 16
Figure 2.6 a) Photon trajectories in a two-layered highly scattering medium, where the mean squared displacement of scatterers in time in deeper layer is more than superficial layer. The illustration shows photon paths (red and blue), photon traveling through more superficial layers (solid arrows with red paths) has a shorter TOF than photons penetrating deeper into the tissue (solid arrows with blue paths). The dashed arrows present the scattered photon's path at time t and $t + \tau$ respectively. The green dashed arrows present the displacements of scatterers between time t and $t + \tau$. The dark blue and light blue dots present the scatterers at time t and $t + \tau$, respectively. b) Time-gating strategy, enables to distinguish photons based on their time of flight, which facilitates c) calculating the autocorrelation function of photons travelled shorter (early time gate, red) and longer (late time gate, blue) paths through the tissue. 19
Figure 2.7 Effect of a) changes in mean squared displacements of scatterers in time, b) source-detector separation (SDS), c) absorption coefficient (μ_a), and d) reduced scattering coefficient (μ_s') on the decay of electric field autocorrelation curve $g1$. The $g1$ has been calculated using NIRFAST 9.1 [16]..... 21
Figure 2.8 Schematics of the DCS system. SPAD: single-photon avalanche photodiodes, TCSPC: time-correlated single-photon counting. SM fiber: single-mode fiber, MM: multi-mode fiber. ND filter: Natural density filter. 22
Figure 2.9 The 8-meter optical fibers were routed from control room to scanner room, mounted on a non-magnetic holder and were placed on the subjects' head. The pulse oximeter sensor was attached to the index finger of volunteers. 24
Figure 2.10 a) The position of the collimator (F810SMA-780) used as beam expander in the fiber holder. Here the SDS is 1.5cm. b) The top view of the fiber holder showing the fibers' position. The distances from source to detector are 1.5, 2 and 2.5 cm. The distance between the SM fibres' tips is 3.5mm which is the shortest possible distance due to the diameter of outside jacket of the fiber's. 26
Figure 2.11 a) The side view of designed cw-DCS and td-DCS beam expander. b) The schematics of cw-DCS and td-DCS optical probe with the fibers' position in the optical fiber holder. c) The SDS was 2 cm and calculated from the center of the expanded beam to the tip of

the detection fibers. In td-DCS probe, three SM fibers were located at the same SDS. The distance between the SM fibers was 3.5 mm which is the shortest possible distance due to the diameter of outside jacket of the fiber's. The length and width of the optical probes are $6 \times 3.5\ cm$ and the thickness is 2 mm. 27
Figure 2.12 Schematics of the optical probe for simultaneous measurements of IVIM-MRI and cw-DCS. The SDSs were 2 cm and calculated from the center of the expanded beam to the tip of the detection fibers. Two SM fibers were located at the same SDS. The distance between the SM fibers was 3.5 mm which is the shortest possible distance due to the diameter of outside jacket of the fiber's. TRS: time resolved spectroscopy. DCS: diffusion correlation spectroscopy. 27
Figure 2.13 Schematic of containers used for a) homogenous phantom and b) two-layered phantom with possibility to put the optical probe in various distance from the Mylar sheet, to mimic upper layers with different thicknesses. The container was filled with mixture to match the level of fluid with the upper surface of the optical probe..... 30
Figure 2.14 a) The tissue mimicking phantom has the dimension of dimension of $16 \times 14 \times 5.5$ cm in length, width, and depth respectively. b) The top view of the container filled with the agar-gel mixture doped with $NiCl_3$. The mixture filled the container to match the level of fluid with the lower surface of the optical probe. 32
Figure 2.15 The schematics of measurement protocols for a) forearm occlusion test, b) BH test, c) HV test, and d) Valsalva used for evaluation of the td-DCS performance in monitoring the tissue blood flow changes at different SDSs. 35
Figure 2.16 measurements protocols performed by volunteers a) BH and b) HV to evaluate the correlation of the hemodynamics responses measured by cw-DCS and td-DCS with BOLD-MRI. 36
Figure 2.17 A volunteer in supine position on the MRI bed. Both cw-DCS and td-DCS parts were housed in one instrument rack and placed out of the scanner room. 37
Figure 2.18 The schematics of protocol for leg and forearm occlusion used for cross-evaluation of the IVIM-derived parameters with BFI measured by cw-DCS. 38
Figure 2.19 The position of td-DCS optical probes a) on the flexor compartment of volunteer's forearm and b) forehead. c) Position of optical probes on the volunteer's forehead while simultaneous measurements of cw-DCS and td-DCS with BOLD-MRI technique. d) The white circles in the MRI image refers to the vitamin E as a marker to determine the place of optical fibres. The vitamin E were located between the source and detection fibres on each optical probe of cw-DCS and td-DCS. Position of optical probes on the e) gastrocnemius compartment

of the leg and f) extensor compartment of forearm while simultaneous measurements of cw-DCS and IVIM-MRI. 39
Figure 2.20 Sketch of the td-DCS data pre-processing approach. a) The temporal positions of the detected photons (orange asterisks) shown together with the trigger pulses generated by the laser driver, the rectangular green area shows the position of the gate, limited by specific times of flight photons between t_{s1} and t_{s2}. b) The DTOF is obtained by building a histogram of photon counts as a function of t_s, same as in (a) the rectangular green area shows the position of the gate limited by specific times of flight photons between t_{s1} and t_{s2}. c) The number of photons counted during the measurement. The rectangular blue area shows a 3 s integration time (between absolute arrival times of t_1 and t_2). d) The intensity autocorrelation function is obtained from the photons detected within the specific time of flight (between t_{s1} and t_{s2}), and specific absolute arrival time (t_1 and t_2), where τ is the lag time. 42
Figure 2.21 Two fitting scenarios were used to estimate the αD_b and BFI. a) Fitting the theoretical $g_1\tau$ the whole measured $g1\tau$, b) Fitting the theoretical $g_1\tau$ only to the early portion of the measured $g_1\tau$ (i.e. for $g_1\tau > 0.7$). 43
Figure 2.22 a) The defined early and late gates. Early gate starts with the width of FWHM/2 before the DTOF peak on its rising edge and ends at the DTOF peak. The late gate starts at the DTOF peak and ends with the width of FWHM/2 on the falling edge. b) Considering higher αDb in deeper layer comparing to superficial layer, the signals obtained from photons detected in early gate are expected to be more sensitive to changes in αDb of scatterers appearing in the superficial layer and the corresponding autocorrelation function decays slower; the signals obtained from photons detected at late gate are expected to be more sensitive to changes in αDb of scatterers appearing in the deeper layer and the corresponding autocorrelation function decays faster. 45
Figure 3.1 The IRF as well as the DTOFs measured on homogenous phantoms with a) 40% Glycerol concentration and b) no Glycerol. Time zero refers to 5% of the IRF on rising edge. The figure was adapted from N. Mogharari et al. [39]..... 56
Figure 3.2 a) Estimated $\beta(t,t_s)$ and c) $\alpha D_b(t,t_s)$ as a function of time of flight for homogeneous phantoms containing 40% glycerol, b) Estimated $\beta(t,t_s)$ and d) $\alpha D_b(t,t_s)$ as a function of time of flight for homogeneous phantoms containing 0% glycerol, measured at source-detector separations of 1.5, 2.0, and 2.5 cm. Error bars represent the standard deviation. Time zero was defined as the time point corresponding to 5% of the IRF maximum on the rising edge of the DTOF. 57

Figure 3.3, $\beta(t,t_s)$ at different time of flight of photons (t_s) and SDSs of a) 1.5cm, b) 2cm and c) 2.5cm. Time 0 is set at the maximum value of the DTOF. Each data points have been calculated within windows of 100 ps from 120 $g_2(t,\tau)$ collected with 2 s integration time. The rectangular red and blue areas refer to the early and late gates, respectively. DL – deep layer, SL – superficial layer. The figure was adapted from N. Mogharari et al. [39]..... 59
Figure 3.4 The calculated coefficient of variation $CV_\beta(t,t_s)$ metrics at different time of flight of photons (t,t_s) and SDSs of a) 1.5 cm, b) 2cm and c) 2.5cm. Each data points have been calculated within windows of 100 ps from 120 g_2 (t,τ) collected with 2 s integration time. The rectangular red and blue areas refer to the early and late gates. The time 0 refers to the DTOF peak. DL – deep layer, SL – superficial layer. The figure was adapted from N. Mogharari et al. [39]. 60
Figure 3.5 The calculated contrast to noise ratio $CNR_\beta(t, ts)$ metrics at different time of flight of photons (t,t_s) and SDSs of a) 1.5, b) 2 and c) 2.5 cm. Each data points have been calculated within windows of 100 ps from 120 $g_2(t,\tau)$ collected with 2 s integration time. The rectangular red and blue areas refer to the early and late gates. The time 0 refers to the DTOF peak. DL – deep layer, SL – superficial layer. The figure was adapted from N. Mogharari et al. [39]. ... 61
Figure 3.6 The recovered $\alpha D_b(t,t_s)$ parameter as a function of time of flight of photons for different SDSs of a) 1.5, b) 2 and c) 2.5 cm. Time 0 is set at the maximum of the DTOF. Each data points have been calculated within windows of 100 ps from 120 autocorrelation functions $g_2(t,t_s,\tau)$, collected with 2 s integration time each. The red and blue shaded areas refer to the early and late gates, respectively. DL – deep layer, SL – superficial layer. The figure was adapted from N. Mogharari et al. *[39]*. 63
Figure 3.7 The recovered coefficient of variation $CV_{\alpha Db}(t,t_s)$quality metric at varying time of flight of photons and SDS of a) 1.5, b) 2 and c) 2.5 cm. Time zero is set at the maximum of the DTOF. Data point calculated within windows of 100 ps from 120 autocorrelation functions $g_2(t,t_s,\tau)$, collected with 2 s integration time each. The red and blue shaded areas refer to the early and late gates, respectively. The time zero refers to the DTOF peak. DL – deep layer, SL – superficial layer. The figure was adapted from N. Mogharari et al. [39]..... 64
Figure 3.8 The recovered contrast to noise ratio $CNR_{\alpha Db}(t,t_s)$ quality metric at varying time of flight of photons and SDS of 1.5 (a), 2 (b) and 2.5 (c) cm. Time 0 is set at the maximum of the DTOF. Data point calculated within windows of 100 ps from 120 autocorrelation functions $g_2(t,t_s,\tau)$ collected with 2 s integration time each. The rectangular red and blue areas refer to the early and late gates. The zero time refers to the DTOF peak. DL – deep layer, SL – superficial layer. The figure was adapted from N. Mogharari et al. [39]..... 65

Figure 3.9 The $r\alpha D_b=\alpha D_{b\ fast}(t,t_s)/\alpha D_{b\ slow}(t,t_s)$ measured a) without the beam expander and b) with the beam expander at tip of detection fiber. The boxplots were calculated from the data acquired within early and late gates from 120 autocorrelation functions $g_2(t,t_s,\tau)$ collected with 2 s integration time each. In each boxplot, the central line represents the median, the lower and upper edges indicate the 25th and 75th percentiles, respectively. Whiskers extend to the most extreme data points, not considering outliers. Outliers are indicated by plus signs. The figure was adapted from N. Mogharari et al. [39]. 66
Figure 3.10 Sensitivity of the td-DCS to monitor the $\alpha D_b(t,t_s)$ of scatterers in deep layer ($S_{DL}(t,t_s)$) at SDS of a) 1.5, b) 2 and c) 2.5 cm for various top layer thickness. The data were calculated within early and late gates from 120 $g_2(t,t_s,\tau)$ collected with 2 s integration time each. In each boxplot, the central line represents the median, and the lower and upper edges indicate the 25th and 75th percentiles. The whiskers extend to the most extreme data points, not considering outliers. Outliers are indicated by plus signs. The figure was adapted from N. Mogharari et al. [39]..... 68
Figure 3.11 Sensitivity of the td-DCS to monitor the $\alpha D_b(t,t_s)$ of scatterers in superficial layer ($S_{SL}(t,t_s)$) at SDS of a) 1.5, b) 2 and c) 2.5 cm for various top layer thickness. The data were calculated within early and late gates from 120 $g_2(t,t_s,\tau)$ collected with 2 s integration time each. In each boxplot, the central line represents the median, and the lower and upper edges indicate the 25th and 75th percentiles. The whiskers extend to the most extreme data points, not considering outliers. Outliers are indicated by plus signs. The figure was adapted from N. Mogharari et al. [39]..... 69
Figure 3.12 a) Schematic of the hemodynamic changes in response to the arterial occlusion (180 mmHg) measured at SDS = 2 cm on a healthy adult volunteer. b) The rBFI change (from baseline to arterial occlusion). c) The PORH peak at three SDSs. The statistics (b, c) are calculated from 16 datasets. In each boxplot, the central line represents the median, and the lower and upper edges indicate the 25th and 75th percentiles. The whiskers extend to the most extreme data points, not considering outliers. Outliers are indicated by plus signs. The figure was adapted from N. Mogharari et al. [39]. 71
Figure 3.13 rBFI changes during BH at shorter (1.5 cm) and larger (2 and 2.5 cm) SDSs. Solid line and shaded area refer to mean value and standard deviation of the data calculated from 12 datasets at a) SDS = 1.5 and b) SDS=2 cm, and c) 8 datasets at SDS = 2.5 cm (Data from two subjects at SDS=2.5 cm was collected with a significant noise level. This data was excluded from further averaging and statistical analysis). Shaded areas indicate the task period. The figure was adapted from N. Mogharari et al. [39]..... 73

Figure 3.14 rBFI changes during HV at shorter (1.5 cm) and longer (2 and 2.5 cm) SDSs. Solid line and shaded area refer to mean value and standard deviation of the data calculated from 12 datasets at a) SDS = 1.5 and b) SDS=2 cm, and c) 8 datasets at SDS = 2.5 cm (Data from two subjects at SDS=2.5 cm was collected with a significant noise level. This data was excluded from further averaging and statistical analysis). Shaded areas indicate the task period. The figure was adapted from N. Mogharari et al. [39]. 74
Figure 3.15 The distribution of rBFI changes caused by a) BH and b) HV at three SDSs of 1.5, 2 and 2.5 cm. Each boxplot calculated from 12 datasets at SDS = 1.5 and 2 cm, and 8 datasets at SDS = 2.5 cm (Data from two subjects at SDS of 2.5 cm was collected with a significant noise level and excluded from further averaging and statistical analysis). rBFI change refers to differences between the average rBFI of the baseline and the average rBFI in response to each task (from 10 seconds after the start time to 10 seconds after the completion of the task). In each boxplot, the central line represents the median, the lower and upper edges indicate the 25th and 75th percentiles, respectively. The whiskers extend to the most extreme data points, not considering outliers. Outliers are indicated by plus signs. The figure was adapted from N. Mogharari et al. [39]. 75
Figure 3.16 rBFI changes during Valsalva manoeuvre (VM) at SDS of a) 1.5, b) 2 (b) and c) 2.5 cm. Solid line and shaded area refer to mean value and standard deviation of data calculated from 8 datasets at SDS = 1.5 and 2 cm, and 6 datasets at SDS = 2.5 cm (Data from one subject at SDS 2.5 cm was collected with a significant noise level. This data was excluded from further averaging and statistical analysis). 76
Figure 3.17 a) Calculated β for the homogenous phantom with 40% and 0% Glycerol concentrations. $n\alpha D_b$ represents the sensitivity to detect αD_b changes in b) deep and c) superficial layers measured by cw-DCS and td-DCS techniques on two-layered phantom. For cw-DCS, the metrics have been calculated by fitting the whole g_1 curve as well as $g_1 > 0.7$. For td-DCS the metrics have been calculated from detected photons in defined early and late gates. Each boxplot acquired within 120 g_2 curve with 2.5 s integration time. In each boxplot, the central line represents the median, the lower and upper edges indicate the 25th and 75th percentiles, respectively. The whiskers extend to the most extreme data points, not considering outliers. Outliers are indicated by plus signs. The figure was adapted from N. Mogharari et al. [175]. 79
Figure 3.18 Panels a and b show the averaged BOLD signal maps from fourteen subjects during BH and HV respiratory challenges, respectively. The color bar represents the intensity of BOLD signal changes, where green indicates baseline, and red and blue regions correspond to

significant increases and decreases in BOLD signal, respectively. The color scale applies exclusively to panels (a) and (b). Panel c displays the segmented tissue masks used for analysis: scalp (blue), skull (green), and gray matter (red). BOLD signals from the intracerebral layer were extracted specifically from the gray matter regions. The image slices were reconstructed with a thickness of 2.5 mm and were spaced at 12.5 mm intervals. The figure was adapted from N. Mogharari et al. [175]. 80
Figure 3.19 The group averaged signals of a) BOLD, b) heart rate (HR) and oxygen saturation (SpO_2), BFI measured by c) cw-DCS and d) td-DCS during BH (breath hold). The mean values (solid lines) and corresponding standard deviations (shaded areas) were obtained over 28 datasets measured from fourteen individual subjects. The vertical lines show the beginning and the end of BH respiratory challenge. The figure was adapted from N. Mogharari et al. [175]. 82
Figure 3.20 The group averaged signals of a) BOLD, b) heart rate (HR) and oxygen saturation (SpO_2), BFI measured by c) cw-DCS and d) td-DCS during HV (Hypertension). The mean values (solid lines) and corresponding standard deviations (shaded areas) were obtained over 28 datasets measured from fourteen individual subjects. The vertical lines show the beginning and the end of respiratory challenge. The figure was adapted from N. Mogharari et al. [175]. 83
Figure 3.21 a, b) Mean BOLD signal changes and c, d) mean BFI changes calculated for breath hold and hyperventilation respiratory challenges. Each boxplot has been obtained from 28 data point. In each boxplot, the central line represents the median, the lower and upper edges indicate the 25th and 75th percentiles, respectively. The whiskers extend to the most extreme data points, not considering outliers. The figure was adapted from N. Mogharari et al. *[175]*..... 85
Figure 3.22 The hysteresis loops of the normalized BFIs versus BOLD signal changes during a, b) BH and c, d) HV tasks averaged over fourteen subjects. The arrows represent the loop's direction (clockwise and counter clockwise). The figure was adapted from N. Mogharari et al. [175]. 87
Figure 3.23 Histograms of delays between the hemodynamic responses measured by DCSs and BOLD-MRI techniques calculated for individual subjects. The negative and positive delays refer to the earlier and later appearance of the BFI response versus BOLD signal. The black lines show the center of the histogram and the averaged value of the delay between BFI and BOLD signal. The figure was adapted from N. Mogharari et al. [175]. 89
Figure 3.24 Scatterplot to compare the hemodynamic responses measured by a, b) cw-DCS and c, d) td-DCS versus BOLD-MRI techniques in response to BH and HV respiratory challenges.

Each regression plot has been calculated for the acquired data from the beginning of the challenges to 20 s and 40 s after the end of the BH and HV, respectively. Y and X axis show percentage changes both from 0 to 100. The figure was adapted from N. Mogharari et al. [175]. 91
Figure 3.25 The group-averaged signals of $CMRO_2$ obtained in response to a) BH and b) HV. The green line represents the $CMRO_2$ changes calculated from BFI measured by cw-DCS when fitting $g_1 > 0.7$, and the blue line corresponds to BFI calculated from the late gate of td-DCS. The mean values (solid lines) and corresponding standard deviations (shaded areas) were obtained over 28 datasets measured from fourteen individual subjects. The vertical lines show the beginning and the end of respiratory challenges. 92
Figure 3.26 The DWI image of tissue mimicking phantom at pump flow rate (F_{pump}) of 2 mm^3/s. The color bars represent the signal amplitudes. The tissue mimicking phantom has the dimension of $16 \times 14 \times 5.5$ cm in length, width, and depth respectively. 94
Figure 3.27 a) FI_{DCS} (DCS-derived flow index), b) D_{fast} (IVIM-derived pseudo diffusion coefficient), c) D_{slow} (IVIM-derived diffusion coefficient), d) f (IVIM-derived perfusion fraction), and e) F_{IVIM} (IVIM-derived flow) measured on tissue mimicking phantom at baseline and six F_{pump} (pump flow rate) from 1 to 6 mm^3/s. Each boxplot has been calculated from five data points. In each boxplot, the central line represents the median. The lower and upper edges indicate the 25th and 75th percentiles, respectively. The whiskers extend to the most extreme data points, not considering outliers. 95
Figure 3.28 Correlation of a) D_{fast} (IVIM-derived pseudo diffusion coefficient), and b) $F_{IVIM}=f \cdot D_{fast}$ (IVIM-derived flow) with the FI_{DCS} (DCS-derived flow index) measured on tissue mimicking phantom at baseline and at six F_{pump} (pump flow rate) from 1 to 6 mm^3/s with the step of 1. Each color represents one series of measurements. Due to the small values of the measured FI_{DCS} and IVIM-derived parameters at baseline and the F_{pump} of 1-2 mm^3/s, the corresponding data points overlap. 96
Figure 3.29 The DWI image of a volunteer's a) leg and b) forearm during the baseline. The highlighted area indicates the masks, used to calculate the IVIM-derived parameters. The black-white and colored bars represent the MR signal amplitudes of the entire tissue and the region of interest respectively. Arterial and venous vessels with active blood perfusion show greater signal attenuation and are displayed in dark gray. In contrast, the areas with restricted water molecular motion, such as bones and muscles, exhibit less MR signal attenuation and appear in light gray [30, 127]. Bright spots correspond to voxels occupied mostly by veins or arteries.

These voxels were excluded from analayses. To improve image contrast, the MR signal from fat tissue (surrounding the muscles) was suppressed. 97
Figure 4.30 a) BFI_{DCS} (DCS-derived blood flow index), b) D_{fast} (IVIM-derived pseudo diffusion coefficient), c) D_{slow} (IVIM-derived diffusion coefficient), d) f (IVIM-derived perfusion fraction) and e) $BF_{IVIM}=f \cdot D_{fast}$ (IVIM-derived blood flow), during baseline, venous, and arterial occlusion measured on 5 healthy adult volunteers' leg. In each boxplot, the central line represents the median. The lower and upper edges indicate the 25th and 75th percentiles, respectively. The whiskers extend to the most extreme data points, not considering outliers. 99
Figure 4.31 a) BFI_{DCS} (DCS-derived blood flow index), b) D_{fast} (IVIM-derived pseudo diffusion coefficient), c) D_{slow} (IVIM-derived diffusion coefficient), d) f (IVIM-derived perfusion fraction) and e) $BF_{IVIM}=f \cdot D_{fast}$ (IVIM-derived blood flow), during baseline, venous, and arterial occlusion measured on 4 healthy adult volunteers' forearm. In each boxplot, the central line represents the median. The lower and upper edges indicate the 25th and 75th percentiles, respectively. The whiskers extend to the most extreme data points, not considering outliers. 100

1 Introduction

1.1 Context

Blood flow is responsible for distributing nutrients and oxygen to all organs in the body and for removing metabolic waste products. Insufficient blood flow leads to tissue damage, impaired metabolism. Thus, blood flow is considered as an important clinical biomarker for tissue health [1].

Skeletal muscle is the largest organ system in the human body and has a high metabolic demand. Alterations in muscle perfusion is associated with a wide range of conditions. For example, reduced blood flow to skeletal muscle is considered a contributing factor to the decline in muscle mass, strength, and functional capacity associated with aging [2]. Similarly, impaired microvascular perfusion and dysregulated blood flow are signs of metabolic disorders such as diabetes mellitus. In this condition reduced muscle blood flow can lead to intense insulin resistance and delay the tissue recovery [3]. Given the critical role of skeletal muscle blood flow, there is a need for reliable, non-invasive techniques capable of continuously monitoring muscle perfusion. Moreover, careful assessment of muscle blood flow provides valuable insight into underlying muscle health and vascular function.

Brain hemodynamic response refers to changes in blood flow, blood volume, and oxygen delivery within the brain tissue following the brain activities [4]. Cerebral blood circulation, through cerebral blood flow (CBF), ensures a continuous supply of oxygen and nutrients vital for the brain's function and preservation of its structural integrity. Cerebral tissues receive about 20% of the body's oxygen [5]. Any interruption in CBF can compromise brain function and may ultimately result in brain death. Although CBF monitoring is not routinely performed in clinical settings due to the limitations of current technologies, its continuous assessment is essential in neuro imaging applications and neurovascular coupling studies [6]. On the other word, continuous monitoring of CBF is crucial for evaluating brain injuries associated with inadequate perfusion, ischemic events, and disrupted vascular autoregulation [7, 8].

Several techniques have been developed for continuous and non-invasive monitoring of tissue and CBF with practical advantages and limitations. Transcranial Doppler ultrasound, a commonly used clinical tool, measures blood flow in large vessels [9]. Laser Doppler

flowmetry estimates blood flow in superficial tissue layers [10]. Positron emission tomography (PET), considered as a gold standard technique, requires intravenous injection of a radioactive tracer [11]. Magnetic resonance imaging (MRI) based techniques offer high spatial resolution of perfusion imaging; however, suffer from relatively low temporal resolution and signal to noise ratio [12, 13]. Both PET and MRI systems are expensive, bulky, and require transporting the patient to a specialized facility.

Significant advancements in diagnostic instruments and therapeutic tools may greatly contribute to reduce mortality rates and enhance diagnostic precision and treatment effectiveness. The non-invasive techniques have potential to emerge the broader implementation in clinical practice. In the case of photonic and optical technologies, despite the long history of exploration, their full potential has yet to be fully realized. In recent years, however, rapid progress across these technological domains has significantly enhanced the feasibility and reliability of optical tools in clinical applications.

Diffuse optical spectroscopy (DOS) stands out as particularly promising. DOS techniques are implemented in a reflectance geometry, where near-infrared light is sent into tissue, and the scattered light is detected a few centimetres away from the light source. The detected signal predominantly arises from photons that traveled through a banana-shaped profile between the source and detector (figure 1.1). DOS comprises several modalities, most notably near-infrared spectroscopy (NIRS), and diffuse correlation spectroscopy (DCS). In DOS techniques, near infrared light in the optical window with the wavelength range of 650 to 950 nm [14] is used to illuminate the tissue. This range of wavelength is characterized by relatively low absorption and reduced scattering for biological tissues, which allows photons to penetrate several centimetres into deeper layers [15].

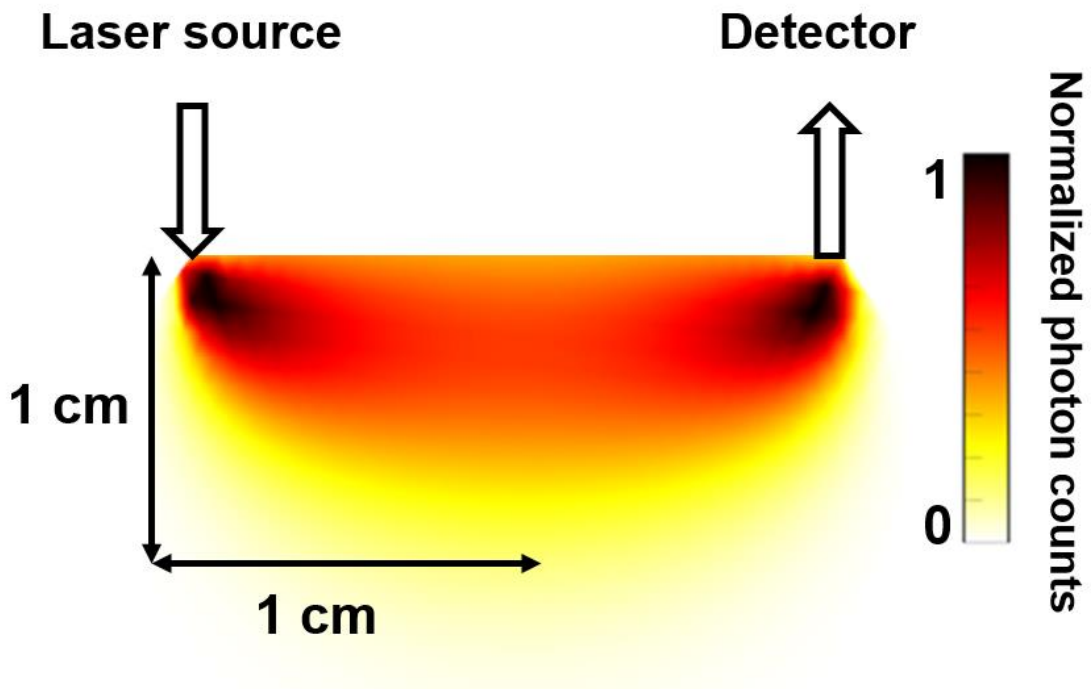


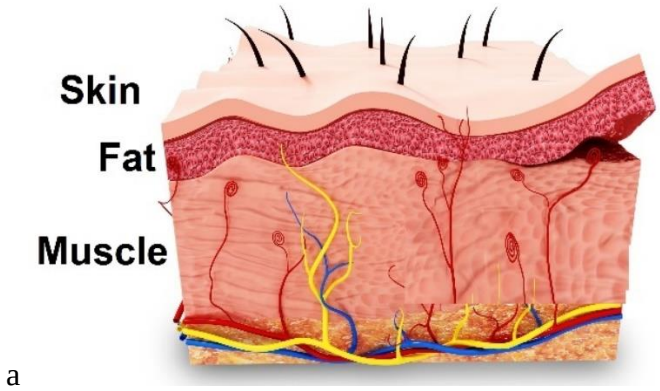
Figure 1.1 Schematics of diffuse light measurement in reflectance geometry, where a laser source is used to illuminate the tissue, and the scattered light is detected a few centimetres away from the fiber tip of the laser source. The colorbar present the photon counts. The figure was obtained using NIRfast package for a turbid medium, where the distance between the source and detector is 2 cm. The optical properties of tissue was considered to be $\mu_a = 0.01$ cm^{-1}and $\mu_s' = 1$ cm^{-1} [16].

The interaction of near infrared light with the medium alters the light properties in a way that it contains information about the tissue's composition and also helps to extract meaningful physiological parameters. Building on this discovery, DOS was developed to investigate tissue hemodynamic, such as cerebral oxygenation and cerebral blood volume [17]. Conventional NIRS primarily measures tissues optical properties including absorption coefficient (μ_a) and reduced scattering coefficient (μ_s') (detailed in 2.1 Basics of tissue optics), haemoglobin oxygen saturation and concentration. Although NIRS can estimate tissue's perfusion, doing so typically requires the use of exogenous contrast agents (e.g., indocyanine green) [18], which limits its utility for continuous monitoring.

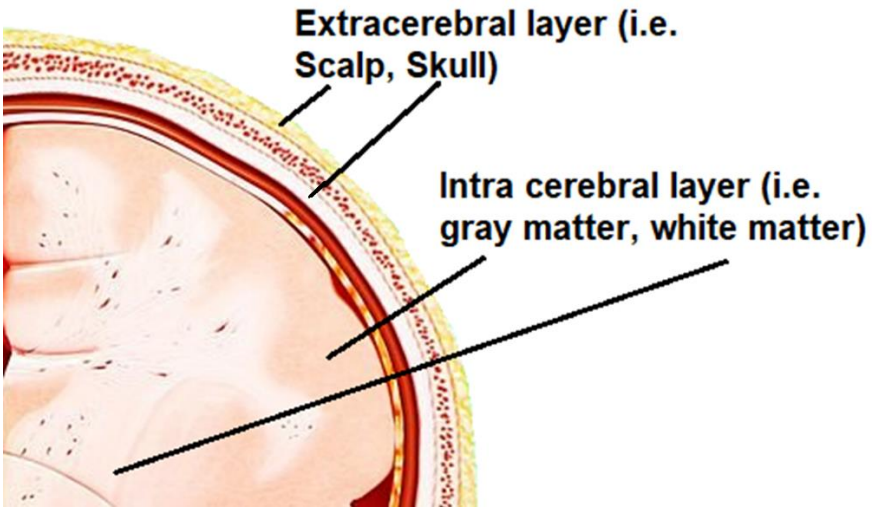
DCS is emerging as a promising optical technique in DOS for bedside tissue and CBF monitoring due to its advantages such as non-invasiveness, portability, and relatively low cost [19]. In this technique a long coherence laser is used to illuminate the tissue. As the light travels through the tissue, it interacts with moving red blood cells, causing fluctuations in the detected light intensity. These fluctuations are evaluated to estimate the tissue's blood flow index (BFI) [20]. In contrast to other blood perfusion imaging techniques [21, 22], the measured BFI does

not have absolute unit of perfusion (i.e. mL/100 g/min); this parameter is directly proportional to the tissues' blood flow changes [23].

A major limitation of DCS as a routine tool to monitor tissue and cerebral blood flow is the contamination of detected signals by compounds in the superficial layer which interferes with accurately measuring the deeper layer blood flow change. The muscle tissue BFI measured by DCS is affected by the blood flow in skin as well as the tissue fat fraction [24, 25] (figure 1.2 a). The detected signal from human head is also affected by extracerebral layers (e.g., scalp and skull). However, in neuroimaging and brain monitoring applications, the hemodynamic signals originating from intracerebral tissues (e.g., grey and white matter) are more clinically informative [26, 27] (figure 1.2 b).



a



b

Figure 1.2 Schematics of simplified model of different layers of a) tissue muscle and b) human head. The figures were modified from https://www.gettyimages.com/.

There are two main implementations of the DCS technique: continuous-wave DCS (cw-DCS) [28] and time-domain DCS (td-DCS) [29]. The cw-DCS technique, which uses a continuous-wave laser to illuminate the tissue, lacks the ability to discriminate photons based

on their pathlength through the tissue. With a single source-detector separation (SDS), cw-DCS integrates signals from all photon paths, making it difficult to distinguish between contributions of superficial and deeper tissue layers' blood flow changes [30]. Due to the diffusive nature of light propagation in biological tissues, increasing the SDS enhances the probability of detecting photons that have travelled deeper tissue layers [31]; although, this comes at the cost of a decreased number of detected photons. Some improvements in data analyses has been suggested to enhance the sensitivity to deeper tissues blood flow changes [32]. However, it increases the standard deviation in the estimated BFI [33]. In some studies, to improve the cw-DCS sensitivity to the flow changes in deeper tissue layer, multi-layered model is used to fit the experimental data acquired at multi-distance, which increases the system cost [34].

td-DCS, which utilizes a pulsed laser source, enables the depth discrimination of blood flow in superficial and deeper layers of tissue [29]. This technique allows to select the photons with specific path that penetrate different depths in the tissue. To improve the spatial resolution, increase photon collection, and reduce probe dimensions, td-DCS technique has been applied in the null-distance or short SDS. However, it needs a fast time-gated single-photon avalanche diode [19, 35]. While a narrower laser pulse width and a shorter instrument response function (IRF) in the td-DCS system are desirable for improving the depth discrimination of the measured BFI [36], they come with trade-offs. A shorter pulse width typically reduces the laser coherence length and increases the error in estimating the displacement of scatterers and blood flow changes [36, 37]. Although td-DCS enables the depth discrimination in tissue's BFI recovery, it comes with practical considerations. The recovered BFI measured by td-DCS depends on factors such as the IRF width, analyzed TOF gate start time, gate width and the SDS [38, 39].

Blood flow monitoring using cw-DCS has been validated against several established techniques, including color-weighted power Doppler ultrasound in mouse tumors [40], laser Doppler flowmetry in rats [41], and xenon-enhanced computed tomography in humans [42]. Additionally, cw-DCS has been validated with various MRI-based modalities for assessing blood flow changes. These include phase-encoded velocity mapping MRI during hypercapnia in children [32], blood oxygenation level dependent (BOLD) MRI in rat brains during electrical forepaw stimulation [43], arterial spin labelling (ASL) MRI during muscle occlusion in humans [44], and during hypercapnic challenges in both rodents [45] and adult humans [46]. cw-DCS has also shown utility in evaluating brain injuries and the effects of anaesthesia [47, 48].

MRI based techniques are considered as gold standard methods to evaluate the hemodynamic responses and can be used as reference method for validation of optical

techniques. BOLD-MRI is commonly used to evaluate the performance of the NIRS and DCS techniques in monitoring the cerebral hemodynamic responses [43]. BOLD-MRI technique is sensitive to changes in deoxyhemoglobin concentration (HbR) [49]. Although the BOLD signal reflects contributions from several factors, including CBF, cerebral blood volume, and the cerebral metabolic rate of oxygen ($CMRO_2$) [50], it has been reported the magnitude of the BOLD signal depends strongly on the exact balance of the CBF and $CMRO_2$ changes [51, 52]. Moreover, BOLD-MRI technique provides hemodynamic responses from both intracerebral and extracerebral regions with good temporal resolution.

On the other hand, optical coherence angiography has been used as a validation technique for IVIM-MRI to quantify the tissues' microvascular structure and microvascular blood perfusion [53]. Intra voxel incoherent motion (IVIM) magnetic resonance imaging (MRI) is a contrast-free diffusion weighted imaging (DWI) technique to visualize the microscopic motions of water molecules and blood perfusion in biological tissue. Diffuse optical spectroscopy has also been combined with diffusion-weighted imaging (DWI) [54] and dynamic contrast-enhanced MRI [55] as an additional tool for breast cancer characterization.

Despite substantial progress in DCS technique for assessing tissue microvascular blood flow, important limitations and questions remain. These challenges motivate further investigation into methodological advancements of DCS technique and its validation. Therefore, I recognized the existing knowledge gaps and defined the aims and hypotheses of this study as below.

1.2 Research gaps, aims and hypothesis

Following the existing research gaps in DCS technique studies has been listed.

Td-DCS at large SDS improves the sensitivity of the measurement to monitor blood flow changes in deeper tissue layers. However, its application is has practical limitations. In DCS systems, single-mode fibres with low numerical aperture and micron-scale core diameters are used. As a result, photon collection efficiency decreases significantly at larger SDSs, making it challenging to monitor blood flow.

Although, the performance of cw-DCS and td-DCS in monitoring CBF has been compared in series of simulations [56, 57], there is a lack of study to compare these techniques in monitoring the cerebral hemodynamic responses. Moreover, no study has been performed to

evaluate the performance of td-DCS in monitoring the cerebral hemodynamic response versus a gold standard technique.

The BFI measured by cw-DCS has been validated in many studies [32, 40]. However, there is lack of study to consider cw-DCS as a technique to assess the microvascular blood flow changes measured by other methods.

To overcome these challenges and research gaps, the aims of this study are listed as follows.

In the first part, I aimed to compare the performance of td-DCS at shorter and larger SDSs to evaluate the impact of SDS in monitoring the changes in displacement of scatterers and RBCs in superficial and deeper layer of phantom and human tissue.

The next part, I aimed to evaluate the correlation of hemodynamic response measured on human head by cw-DCS and td-DCS with BOLD-MRI technique in response to BH and HV respiratory challenges performed by healthy volunteers.

In last part, I aimed to evaluate the correlation between the intravascular perfusion-related motion measured by IVIM-MRI versus BFI measured by DCS.

In line with these aims, following two hypotheses were formulated for this dissertation.

1) Increasing the source detector separation improves the sensitivity of time domain DCS to blood flow changes appearing in deeper tissue layers.
2) Hemodynamic responses measured by DCS technique correlate well with those measured by MRI-based techniques, allowing DCS to serve as an optical tool for assessing microvascular blood flow changes.

1.3 Thesis outline

The structure of this dissertation is as follows:

Chapter 1: In first chapter, a short presentation of the diffuse optical spectroscopy field as well as the aim and hypotheses of this study has been provided.

Chapter 2: In second Chapter, first the theoretical background of the photon propagation in diffusive media and, the theoretical aspects of optical techniques used in the thesis including td-NIRS, cw-DCS and td-DCS has been presented. Then a detailed description of the

experimental setup was described, which followed by the presentation of optical and MRI data acquisition techniques. Next, experimental protocols for phantom and in vivo measurements carried out for system optimization and evaluation were presented. Finally, data analyses used for estimation of the displacement of scatterers, BFI and other hemodynamic parameters were explained.

Chapter 3: In chapter three, first, the results of experiments aimed at optimization of the td-DCS system during series of phantom and in vivo measurements at shorter and larger SDSs were presented. Next, results of cross-evaluation of the brain hemodynamic measured by DCS modalities and BOLD-MRI have been showed. Finally, the results of the cross-evaluation of the IVIM-MRI technique with cw-DCS for estimating the tissue perfusion-related motion and blood flow changes were presented.

Chapter 4: In chapter four, the research findings and results, strengths and limitations of the study have been discussed and the overall conclusions drawn from the results have been presented.

2 Methods

2.1 Basics of tissue optics

2.1.1 Photon Propagation in Tissue

The model of photon propagation in an optically turbid medium such as biological tissue based on solution of diffusion equations, has been proposed in multiple theoretical works [58, 59]. However, this model is simplification of the light propagation as electromagnetic wave, described by Maxwell's equations or the laws of geometrical optics. Because of the complexity of tissue structure, the inhomogeneity of component elements, and the large number of light rays to be considered it is difficult to obtain solutions to Maxwell's equations for such a medium. Therefore, several assumptions are considered to simplify this problem and describe the light propagation analytically in a scattering samples using photon diffusion theory [60].

The radiative transport equation can be simplified to the diffusion equation (Equation 2.1) under following assumptions. It can be assumed that the optical source illuminating the sample generates the isotropic power distribution of S (R, t), at position r and time t. Furthermore, the diffusion approximation can be applied only when the trajectories of the photons reaching the detector are completely random. This condition is met when the distance from the emission point to the detection point is greater than the transport mean free path of photons $l_{\mathrm{tr}} = \frac{1}{\mu_{\mathrm{s}}'}$ in the medium, where μ_{s}' is the reduced scattering coefficient of the medium and equals to product of scattering coefficient (μ_s) and $(1 - g)$, where g is the anisotropy factor of tissue (average cosine of the scattering angle). Additionally, the amplitude of temporal intensity fluctuation of the source must be much smaller than the magnitude of $v\mu_{\mathrm{s}}'$, where v is c/n , c is the speed of light in the vacuum and n is the refractive index of the medium. Moreover, the probability of the occurrence of the photon scattering phenomena in the medium must be significantly greater than the probability of the absorption phenomena i.e. $\mu_{\mathrm{s}}' \gg \mu_{\mathrm{a}}$, where μ_{a} is the absorption coefficient. When these conditions are met, light propagation in a turbid medium can be modeled by the diffusion equation [61, 62]:

$$(-D(R)\nabla^2 + v\mu_a(R) + \frac{\partial}{\partial t})\varphi(R,t) = vS(R,t) \quad (2.1)$$

where φ is the fluence rate at time t at the point defined by vector r, S corresponds to the fluence function of the radiation source, v is to the speed of light in the medium, $D = \frac{v}{3\mu_s'}$ is the diffusion coefficient. A detailed description of the derivation of the diffusion approximation from the radiative transport equation is presented in [58, 63].

2.1.2 Time domain near infrared spectroscopy

In time domain NIRS (td-NIRS) technique, tissue is illuminated with an ultra-short pulse laser in reflectance geometry. As photons propagate through the tissue, some are absorbed by absorbers like tissue chromophores. Some other photons undergo multiple scattering events and are scattered by scatterers such as red blood cells. The concentration of absorber and scatteres determin the optical propertiese of tissue μ_a and μ_s'. The detected signal predominantly arises from photons that traveled through a banana-shaped sensitivity profile between the source and detector [64] (figure 2.1).

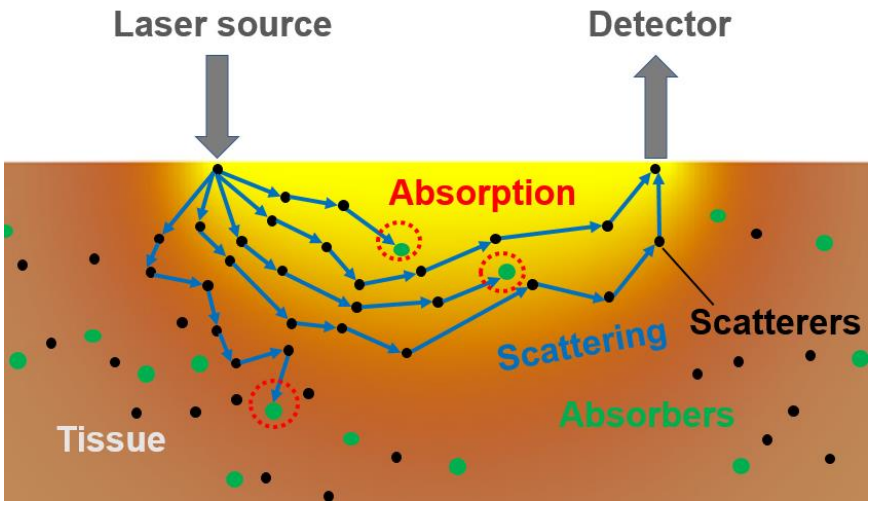


Figure 2.1 Photons trajectories between source and detector in a highly scattering medium forms a banana-shaped sensitivity profile. When photons propagate through the tissue, some are absorbed (see events in red circles) and some undergo multiple scattering events. Black circles mark scatterers and green circles mark absorbers.

In diffuse optics, infinite geometry refers to an ideal medium where there are no boundaries that affect photon propagation. Therefore, in an infinite homogeneous medium, the influence of boundaries on light propagation can be neglected under following conditions: (1) if the point-source and point-detector are sufficiently far from any boundaries, (2) if the point-source and point-detector are embedded within the medium. In these conditions the detected signal depends only on the distance between the point-source and point-detector and the optical properties of

the medium, without any influence of absorption and scattering from boundaries. For an ideal light emitter (generating Dirac pulse), the solution of diffusion equation is as follows [65, 66]:

$$\varphi(R,t) = \frac{v}{(4\pi Dt)^{3/2}} exp\left(-\frac{R^2}{4Dvt} - \mu_a vt\right) \qquad (2.2)$$

In the semi-infinite geometry, both the source and detector are located on the tissue's surface ($z = 0$). The source is perpendicularly located on the medium surface, with a source–detector separation (SDS) of ρ (figure 2.2). When a light source is introduced into a medium with multiple photon scattering, the beam of this radiation can be replaced by an isotropic emitter, which is located under the interface. This condition allows the introduction of a dipole radiation source, which consists of two points of source located in an infinite homogeneous scattering medium. The first point-source is a positive isotropic source located at a depth of $z_0 = l_{\mathrm{tr}}$. This source "pushes out" a stream of light from the medium. The second point-source is a negative imaging isotropic source located on top of the medium and simulates the extraction of radiation from the surrounding space, which hypothetically represents a scattering medium extended upwards to infinity. Therefore, between the sources, there must be an extrapolated boundary on which the values of radiation power of the sources are equal to zero. Because these two hypothetical sources with different polarity simultaneously affect the light fluxes. Since in the real case, part of the scattered radiation leaves the medium through its surface, i.e., at z=0., extrapolated boundary should be located above the interface between the media, i.e., at a distance of z_b. In order to satisfy the zero-boundary condition, a negative imaging isotropic source is assumed at $z = -(z_0 + 2z_b)$, where z_b [58]:

$$z_b = 2l_{tr}\left(\frac{1 + R_{eff}}{1 - R_{eff}}\right) \qquad (2.3)$$

and R_{eff} is the effective Fresnel reflection coefficient, *n* is reflective index of the medium [58]:

$$R_{eff} \approx -1.44n^{-2} + 0.7n^{-1} + 0.668 + 6.36 \times 10^{-3}n \qquad (2.4)$$

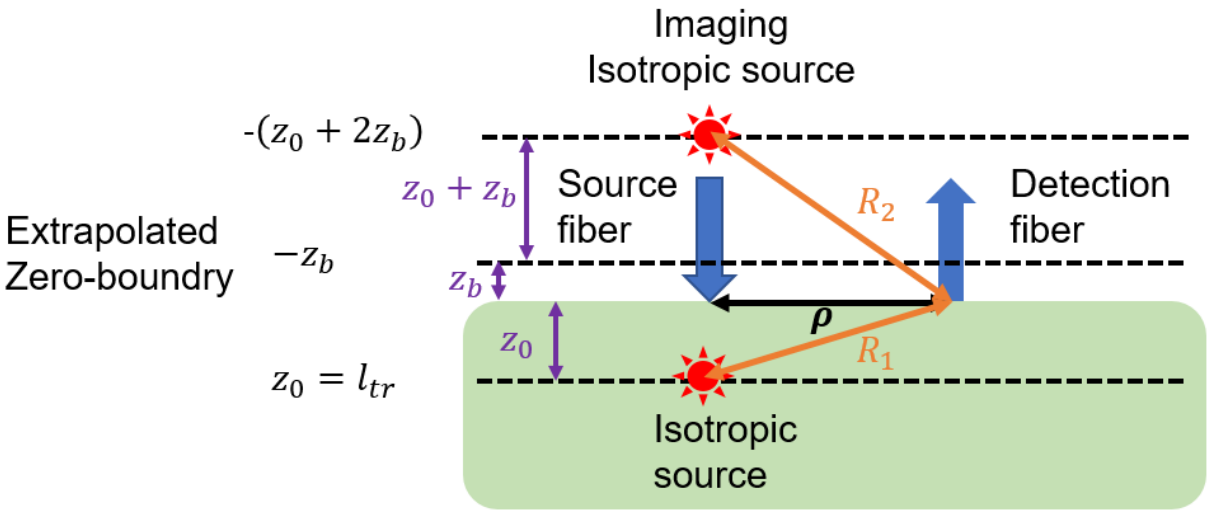


Figure 2.2 The schematic of extrapolated boundary model for photon diffusion in semi-infinite geometry [58].

For the semi-infinite homogeneous medium, the time-resolved reflectance $\varphi(R_{\mathrm{sd}}, t)$ presenting the number of photons per unit area per time emerging the sample surface at the detection point is defined as [65, 67]:

$$\varphi(R_{\mathrm{sd}}, t) = \frac{1}{(4\pi Dt)^{3/2}} \exp(-\mu_a v t) \left(exp\left(-\frac{{R_{sd}}^2 + (z - z_0)^2}{4Dt} \right) - exp\left(-\frac{{R_{sd}}^2 + (z + z_0)^2}{4Dt} \right) \right) \qquad (2.5)$$

Where v is to the speed of light in the medium, $D = \frac{v}{3\mu_s'}$ is the diffusion coefficient, μ_{s}' is the reduced scattering coefficient, μ_a is the absorption coefficient, ρ is the actual distance between the source and detection point (SDS – source-detector separation), $z_0 = 3D$ is the effective source depth, z_b is the extrapolated boundary position [67], $R_{\mathrm{sd}} = \sqrt{\rho^2 + {z_0}^2}$ is the distance between the detection point on the medium surface and the location of the isotropic source (r_1 in figure 2.2).

In td-NIRS, ideally is expected that light sources generate ultrashort Dirac pulse with full width half maximum (FWHM) of almost zero to illuminate the tissue. However, in practice, due to the limitations in the instrumentation, this is not feasible (detailed in 2.2 Instrument-Instrument response function measurement). Figure 2.3 (a) shows a narrow Gaussian laser pulse (FWHM ≈ 0.1 ns) generated in MATLAB 2022b [68]. In tissues, photons undergo

multiple absorption and scattering events, leading to attenuation and broadening of the laser pulse captured by detector. The distribution of time-of-flight (DTOF) describes how many photons arrive at the detection point as a function of their travel time through the tissue. Figure 2.3 (b-d) shows the calculated DTOFs using the NIRFAST 9.1 [16]. The DTOFs were obtained from Eq. (2.5) for a semi-infinite homogeneous medium at various SDSs and a range of optical properties of the medium.

At short SDSs, photons travel shorter paths and primarily sample the shallow tissue layers located close to the tissue surface. Measuring at larger SDS causes photons to undergo more scattering events and longer path lengths leading to increased probability of detecting photons that travel through deeper layers of the tissue. Moreover, an increase in SDS leads to shift the DTOF peak to later times as the photon pathlengths increase and also broadens the DTOF. At shorter SDSs higher number of photons can be detected, while increasing the SDSs leads to decrease the number of detected photons and consequently decrease the amplitude of DTOFs [69, 70] (figure 2.3 (b)).

Changes in μ_a directly influence the shape and amplitude of the DTOF curve. When the medium has low μ_a, photons travel longer distances before being absorbed, leading to a broader DTOF curve with a higher amplitude and higher number of detected photons with long-path. In case of high μ_a, the light absorption is higher, leading to reduce the DTOF amplitude and reduce the number of photons that travelled longer through the tissue, resulting in a narrower and steeper DTOF curve [71] (figure 2.3 (c)).

μ'_s quantifies how light is scattered within the tissue and influences the broadening of the DTOF curve. In medium with low μ'_s, photons travel with less scattering events, resulting in a narrower DTOF curve with higher amplitude. When the μ'_s is higher, photons undergo more scattering events, which increases the paths they travel and delays their arrival time to the detector. This leads to a broader DTOF curve with reduced amplitude, a delayed peak, and an increased mean time of flight [72] (figure 2.3 (d).

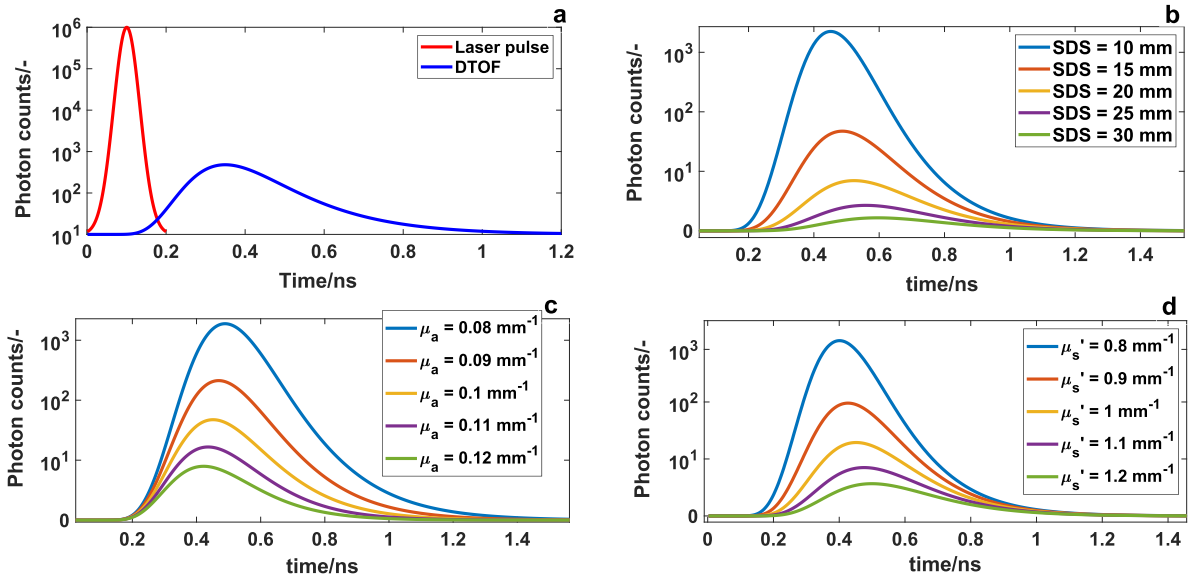


Figure 2.3 a) A narrow Gaussian profile laser pulse (FWHM of 0.1 ns) (red), and the DTOF curve in diffuse reflectance geometry (blue), describing the number of detected photons as a function of their travel time through the tissue (SDS=5 mm, μ_a = 0.08 mm^{-1},μ_s' = 0.8 mm^{-1}). b) DTOFs for varying SDS = 10–30 mm, in 5 mm increments with a fixed absorption coefficient (μ_a = 0.1 mm^{-1}) and reduced scattering coefficient (μ_s' = 1.0 mm^{-1}). c) DTOFs at a fixed SDS (15 mm) and fixed reduced scattering coefficient (μ_s' = 1.0 mm^{-1}) for varying absorption coefficients (μ_a = 0.08–0.12 mm^{-1}, in increments of 0.01 mm^{-1}). d) DTOFs at a fixed SDS (15 mm) and fixed absorption coefficient (μ_a = 0.01 mm^{-1}) for varying reduced scattering coefficients (μ_s' = 0.8–1.2 mm^{-1}, in increments of 0.1 mm^{-1}). The DTOF curves have been calculated using NIRFAST 9.1 [16].

2.1.3 Diffuse correlation spectroscopy

DCS is sensitive to the displacement of scatterers over time. In this technique a long coherence length laser is used to illuminate the tissue. The long coherence length is required to maintain the coherency of the scattered photons to enable interference at the detection point. Thus, the temporal coherency of the laser light is an important factor in developing the instruments [73]. The detected photons from a medium with moving scatterers are diffused with constructive and destructive interferences that cause spatial and temporal variations of the light intensity or the so-called speckle pattern, shown in figure 2.4. However, in DCS technique, the temporal variation of the light intensity is being detected.

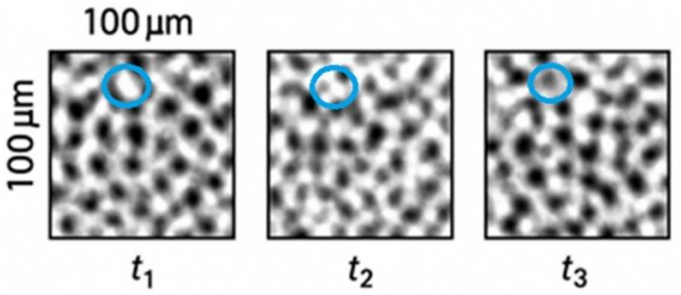


Figure 2.4 The displacement of scatterers causes fluctuations of the scattered light over time t or so-called speckle pattern. The blue circle is considered as the position of the single mode detection fiber's tip which collects the scattered photons.

2.1.4 Continuous wave diffiuse correlation spectroscopy (cw-DCS):

A conceptual sketch of the cw-DCS technique is presented in figure 2.5. The banana-shaped sensitivity profile between the source and detection points, defines where displacements of scatterer (e.g., RBC) affects the estimated BFI (figure 2.5 a). In cw-DCS, where a continuous wave laser is used to illuminate the tissue, the detected signal contains contributions of scattered photons from moving red blood cells in both superficial and deeper tissue layers (figure 2.2 b). Therefore the intensity autocorrelation function (g_2) is calculated from all photons that travelled with various paths in the medium [30]. The decay of the g_2 contains information on the displacements of the scatterers in time expressed with mm^2/s. Then g_2 calculated from photons travelled different path through the medium is fitted to g_2 calculated from theory to estimate the displacement of scatterers [74, 75] (figure 2.5 c).

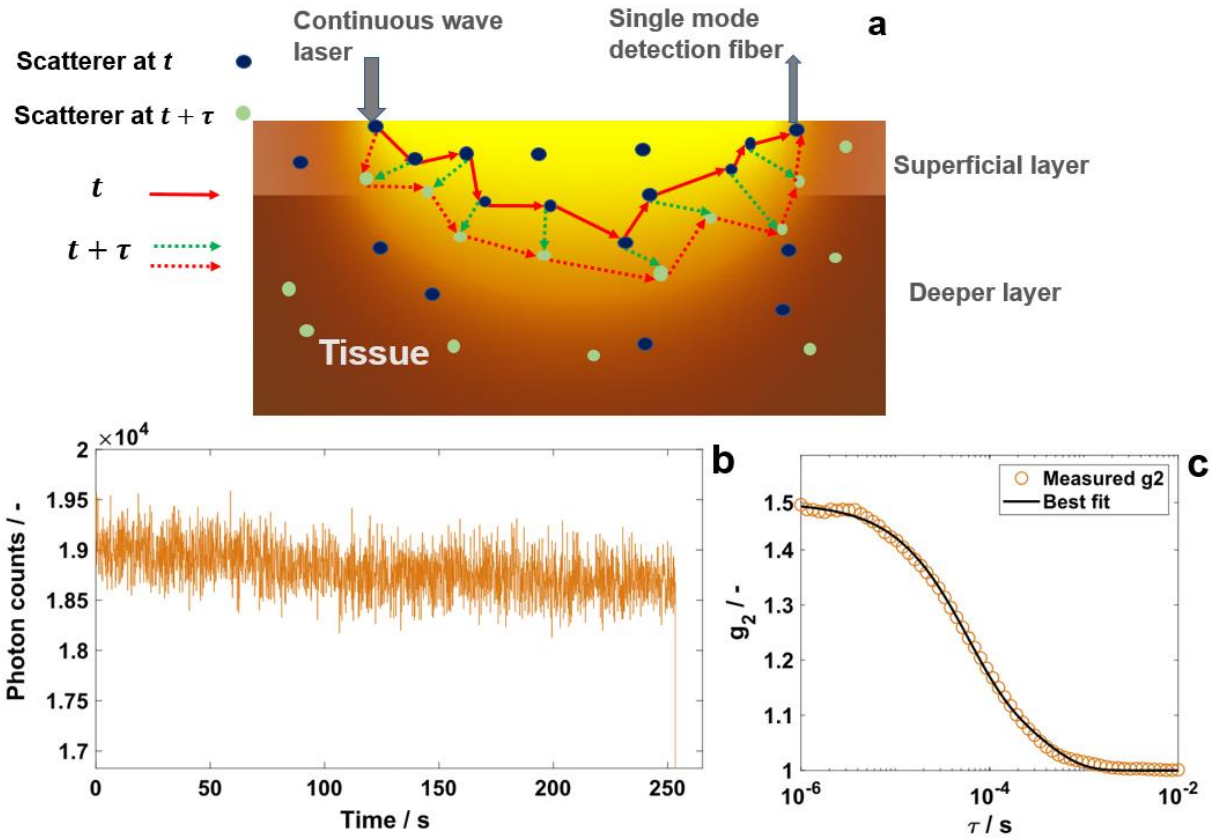


Figure 2.5 a) Photon trajectories between source and detection points in a two-layered highly scattering medium forms a banana-shaped sensitivity profile. The solid and dashed red arrows present the scattered photon's path at time t and $t+\tau$, respectively. The green arrows present the displacements of scatterers between time t and $t+\tau$. The blue and green dots present the scatterers at time t and $t+\tau$, respectively. b) The light intensity fluctuations detected from a continuous wave laser contained scattered photons from both superficial and deeper layers. c) The intensity autocorrelation function g_2 calculated from theory (black solid line) is fitted to g_2 calculated from the photons that travelled different path through the medium (orange circle marks) to estimate the mean squared displacement of scatterers in time.

The g_2 quantifies the intensity fluctuations of the speckle pattern over time, caused by displacement of scatterers [76]:

$$g_2(\tau) = \frac{\langle I(t)I(t+\tau)\rangle}{\langle I(t)\rangle^2} \qquad (2.6)$$

where t is the data collection time, $I(t)$ is the light intensity at time t, and τ is the lag time. Equation (2.6) can be linked to the electric field autocorrelation function ($g_1(\tau)$) by the Siegert relation [77]:

$$g_2(\tau) = 1 + \beta|g_1(\tau)|^2 \qquad (2.7)$$

where β is the coherence parameter depending on the laser coherence length and the number of modes in the detection fiber [29]. Parameter β also depends on the loss of temporal coherency of the detected light caused by moving scatterers [39, 78]. In cw-DCS technique in which a long coherence length laser is used, photon detection with a single mode fiber gives $\beta = 0.5$ for the unpolarized light [79]. In cw-DCS technique, the $g_1(\tau)$ can be expressed as [76]:

$$g_1(\tau) = \int_0^\infty P(s)\, g_1(\tau, s)\, \mathrm{d}s \qquad (2.8)$$

where $P(s)$ is the normalized path length distribution of photons propagating trough the medium and is calculated from the analytical solution of the diffusion equation in a semi-infinite medium. The electric field autocorrelation function (Equation 2.8) for a single pathlength, s, at a lag time, τ, in a scattering medium is given in [80]:

$$g_1(\tau) = \exp\left(\frac{1}{3} k^2 s \mu_s' \langle \Delta r^2(\tau) \rangle\right) \qquad (2.9)$$

where $k = \frac{2\pi}{\lambda}$ is the light wavenumber in the medium, s is the photon path length, and $\langle \Delta r^2(\tau) \rangle = 6 D_b \tau$ is the mean square displacement of the scatterers at lag time τ [81, 82], where D_b is the diffusion coefficient with the unit of cm^2/s or mm^2/s [83]. In DCS, the D_b represents the effective diffusion coefficient of moving scatterers (primarily red blood cells) rather than the true Brownian diffusion coefficient. In biological tissue, scatterer motion is dominated by flow and shear-induced dynamics, not purely Brownian motion, so D_b serves as a parameter proportional to blood flow rather than a direct measure of Brownian diffusion constant. In measurements on phantoms the product of αD_b is the measure of the mean squared discplacement of scatterers in time, where α refers to the fraction of moving scatterers to total number of scatterers (ranging from 0 to 1). In measurements on tissues the αD_b represents BFI of the tissue. The values of αD_b of tissues typically falls in the range of $\sim 10^{-6}\ \mathrm{mm}^2/\mathrm{s}$ [84, 85]. As phantoms should mimic the tissue propertiese, they have to be prepared to have αD_b within the range of $\sim 10^{-6}\ \mathrm{mm}^2/\mathrm{s}$.

2.1.5 Time domain Diffuse Correlation Spectroscopy (td-DCS):

cw-DCS lacks the ability to distinguish blood flow changes appearing in superficial and deeper tissue layers. It also cannot estimate the medium's optical properties unless multiple SDSs and advanced reconstruction algorithms are applied [86]. To improve the DCS technique sensitivity to distinguish the blood flow changes in superficial and deeper layers of tissues, td-DCS has been suggested. In this technique a pulsed laser is used to illuminate the tissue, enables to estimate the blood flow changes in superficial and deeper layers of tissues (figure 2.6 a). In td-DCS, using time gating strategy, the photons can be differentiated based on their TOF, associated with varying paths travelled in tissue [29] (figure 2.6 b). In this strategy, considering lower displacement of scatterers in superficial layer, the photons captured in early gate, enables the calculation of the autocorrelation function of the selected photons scattered from superficial layer of tissue. Considering higher displacement of scatterers in deeper layer, the photons captured in late gate, enables the calculation of the autocorrelation function of the selected photons scattered from deeper layer of tissue (figure 2.6 (c)). In td-DCS technique, the sensitivity to the displacement of scatterers in deep layer can be improved by analysing photons with a higher time of flights (longer pathlengths) which interrogate deeper layers. The measured DTOF, also provides insights into the sample's optical properties, such as absorption and reduced scattering coefficients.

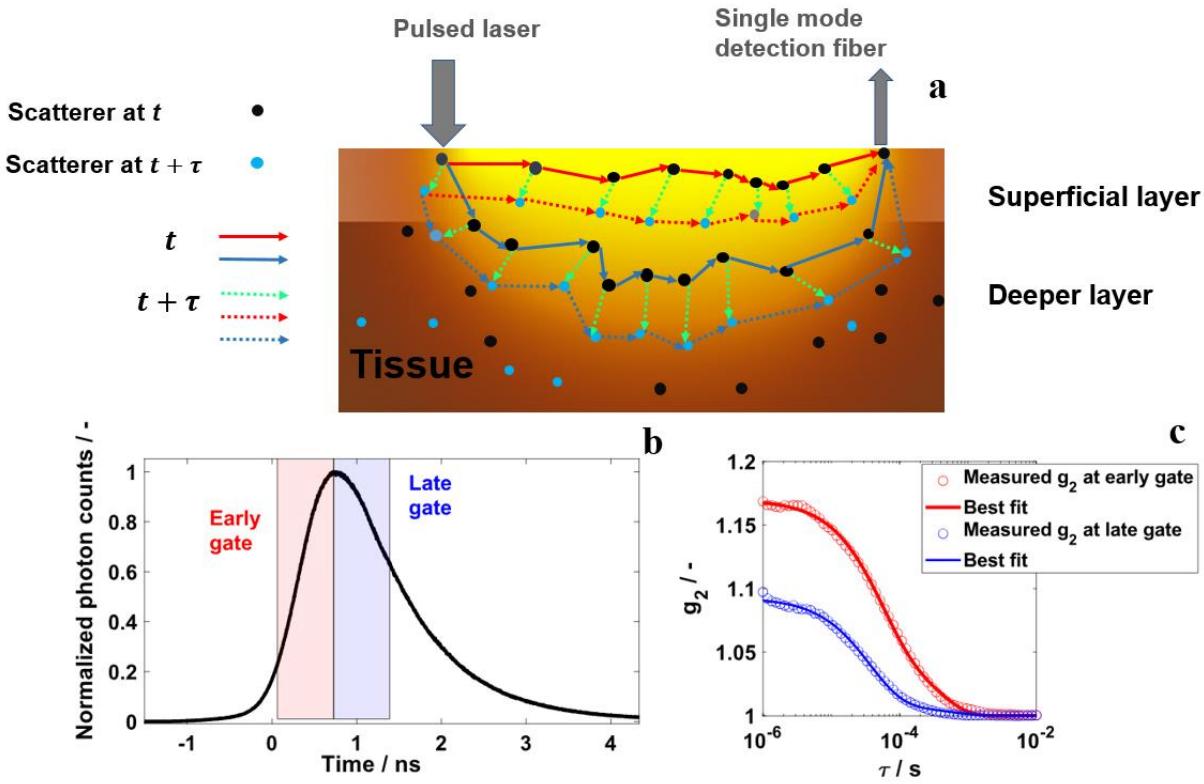


Figure 2.6 a) Photon trajectories in a two-layered highly scattering medium, where the mean squared displacement of scatterers in time in deeper layer is more than superficial layer. The illustration shows photon paths (red and blue), photon traveling through more superficial layers (solid arrows with red paths) has a shorter TOF than photons penetrating deeper into the tissue (solid arrows with blue paths). The dashed arrows present the scattered photon's path at time t and $t+\tau$ respectively. The green dashed arrows present the displacements of scatterers between time t and $t+\tau$. The dark blue and light blue dots present the scatterers at time t and $t+\tau$, respectively. b) Time-gating strategy, enables to distinguish photons based on their time of flight, which facilitates c) calculating the autocorrelation function of photons travelled shorter (early time gate, red) and longer (late time gate, blue) paths through the tissue.

In the td-DCS technique, two times are measured for each detected photon including time of flight (t_s) and absolute arrival time (t). The time t_s is time that photons travel from the source to the detector and is used to build the DTOF. Dividing the DTOF into different time gates allows differentiation of the photons traveling through the tissue with various paths [29]. The time t corresponds to the absolute arrival time since the start of the measurement. So the normalized intensity autocorrelation function $g_2(t_s,\tau)$, is defined as [87]:

$$g_2(t_s,\tau) = \frac{\langle I(t_s,t)I(t_s,t+\tau)\rangle}{\langle I(t_s,t)\rangle^2} \qquad (2.10)$$

where τ is the lag time, $I(t_s, t)$ is the intensity fluctuation of the detected light composed of photon travelling t_s pico seconds between the source and detector and arrived *t* seconds since the start of data collection. $\langle \ldots \rangle$ operator stands for the temporal averaging. The $g_2(t_s, \tau)$ can be linked to the $g_1(t_s, \tau)$ through the Siegert relation (equation 2.10) [77, 88]. The pulsed laser with short pulse required for td-DCS has lower coherence length compared to the continuous wave laser utilized in cw-DCS technique. Low coherence length of the pulsed laser leads to various β across TOF. Consequently, in the case of td-DCS, β depends on the width and the position of the time gate as well [29, 39]. Considering a semi-infinite tissue model, the $g_1(\tau)$ at a given time gate between the t_{s1} and t_{s2} is modelled by the following equation [89, 90]:

$$g_1(t_{s2} - t_{s1}, \tau) = \int_{t_{s1}}^{t_{s2}} P(t_s) \exp\left(\frac{1}{3} k^2 s \mu_s' \langle \Delta r^2(\tau) \rangle\right) \mathrm{d}t_s \qquad (2.11)$$

where $P(t_s)$ is the normalized path length distribution of photons propagating trough the medium and is calculated from the analytical solution of the diffusion equation in a semi-infinite medium (equation 2.5) [90, 91].

In both cw-DCS and td-DCS, the decay rate of g_1 is linked to the particles' mean squared displacement [92]. Slow decay and fast decay refer to lower and higher αD_b, respectively (figure 2.7 (a)). Same as in td-NIRS, in DCS techniques, SDS determines the length of detected photons' paths travelled through the medium, which in turn affects the autocorrelation curve. At shorter SDS (e.g., 5−15 mm), the photons that typically probes more superficial layers of tissue are detected. Photons traveling shorter paths through the medium lead to slower decay of the autocorrelation curve. At larger SDS (e.g., 20 – 30 mm), the probability of detecting photons that penetrate deeper into the tissue is increased. At larger SDS, photons travel longer distances, and experience more scattering events, leading to faster decay of autocorrelation curve [93, 94] (figure 2.7 (b)).

An increase in μ_a reduces the photon travel time, as photons are more likely to be absorbed before they can contribute to the detected signal. This leads to the slower decay of the autocorrelation curve. When μ_a is lower, more photons can survive the path between source and detector, and increases the number of photons that can be detected from deeper layer leading to faster decay of autocorrelation curve [76, 83] figure 2.7 (c).

As μ_s' increases, photons experience more scattering events, which leads to more rapid decorrelation of the scattered light and causes the autocorrelation curve to decay faster. When μ_s' is lower, photons scatter less frequently, leading to a slower decay in the autocorrelation curve [76, 83] figure 2.7 (d).

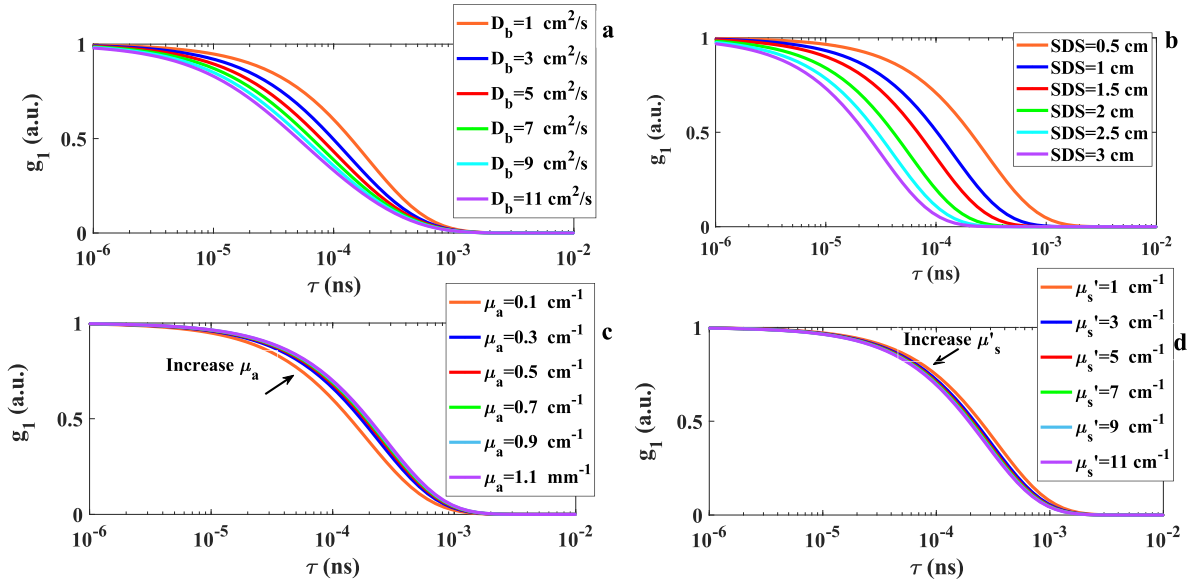


Figure 2.7 Effect of a) changes in mean squared displacements of scatterers in time, b) source-detector separation (SDS), c) absorption coefficient (μ_a), and d) reduced scattering coefficient (μ_s') on the decay of electric field autocorrelation curve (g_1). The g_1 has been calculated using NIRFAST 9.1 [16].

2.2 Instrumentation

The optical hybrid DCS system was equipped with a picosecond pulsed laser, a continuous-wave laser, single photon avalanche diodes, time-correlated single photon counting electronics, optical emission and detection fibres and PC.

Pulsed laser: In this study, a VisIR-765-HP "STED" laser (PicoQuant, Germany) was used, operating at the wavelength of 765nm with an 80MHz repetition rate and a coherence length of ~ 3.5cm. The information on the laser coherence length was provided by the laser manufacturer and was also reported for this laser in reference [95].

Continuous wave laser: The optical hybrid DCS system is equipped with a continuous-wave (DL785-100-SO) (Crystalaser, USA) with the wavelength of 785nm and a coherence length of > 10 meters [96].

***Detectors*:** At the detection side of the optical DCS system, the single photon avalanche diode (SPAD) (PDM, Micro Photon Devices, Picoquant, Germany) is used. SPAD detectors are a silicon-based device known for its high quantum efficiency. This detector can detect photons with timing resolution <50ps and 77 ns dead-time. The quantum efficiency of the detector at

the wavelength of 550nm is 49 % [97].

Emission optical fiber: The light from both pulsed laser and continuous wave laser was coupled to the graded index multi-mode (MM) fibers using a collimator. The used MM fibers have 600µm core diameter and 0.39.

Detection optical fiber: In DCS, the single mode (SM) fibers are used as a detection fiber because the diffused reflected light should be collected from a single speckle. In this study SM fibers (780HP, Thorlabs, USA) with 4.4µm core diameter were used to connect to the SPADs.

Photon time tagging: The time-correlated single photon counting (TCSPC) boards (SPC-150, Becker & Hickl, Germany) were used to time-tag each detected photon. These boards were synchronized to the pulsed laser for a timing reference. TCSPC module records the absolute arrival time of each photon from the beginning of the measurement, called macro time (t). The TCSPC module also records TOF from a specific laser pulse, called micro time (t_s). The TCSPC used in this study, provides 3.05ps (12.5 ns/4096 time bins) temporal resolution for micro time to assess the DTOF and approximately 12.5ns time resolution for macro time [98] to assess the autocorrelation. The TCSPC boards were connected to the PC with a PCIe port.

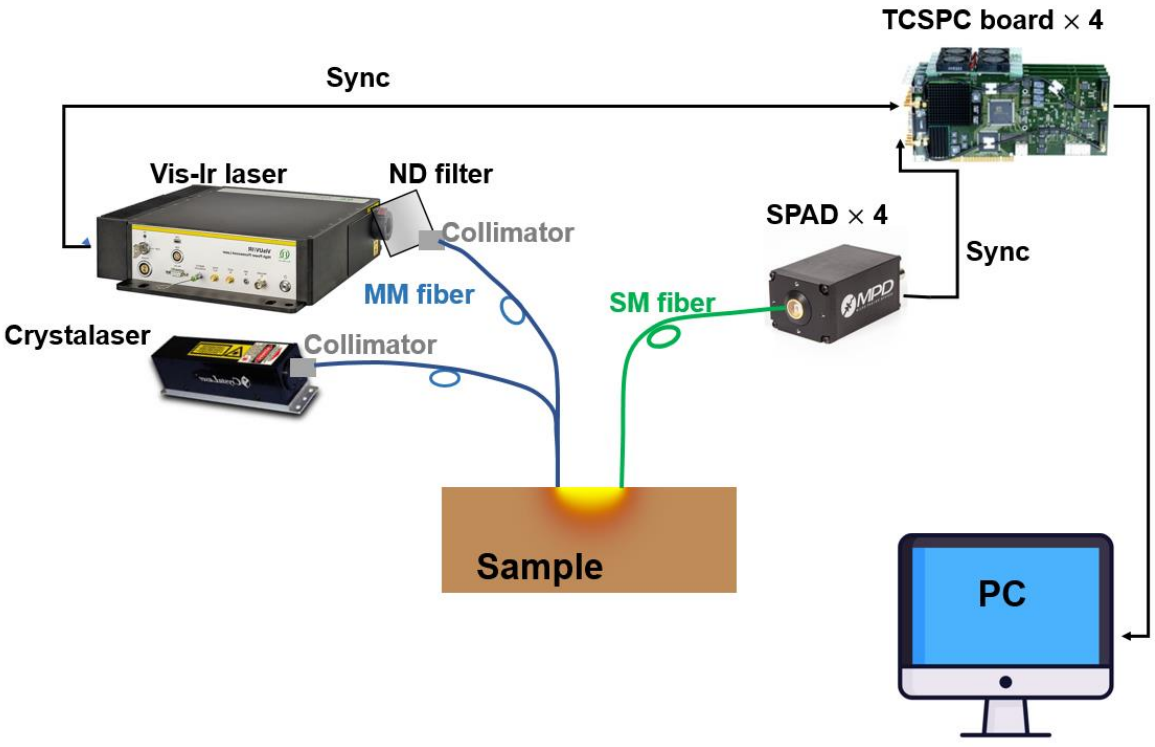


Figure 2.8 Schematics of the DCS system. SPAD: single-photon avalanche photodiodes, TCSPC: time-correlated single-photon counting. SM fiber: single-mode fiber, MM: multi-mode fiber. ND filter: Natural density filter.

Instrument response function measurement: Instrument response function (IRF), refers to the temporal broadening of the detected pulse introduced by the experimental setup components

including light source, detector and electronic components. As laser pulse shape depends on the laser power, the IRF was measured at the same laser power, which was used for both phantom and in vivo measurements. The full width at half maximum (FWHM) of the IRF of td-DCS part was 560ps, measured by positioning the tips of the source with collimator and detection fibers facing each other. A sheet of white paper covered the detection fiber tip to fill up the whole numerical aperture of the fibers [99]. To reduce the laser power and prevent TCSPC photon count overflow while measuring the IRF, neutral density (ND) filters were placed between the detection fiber tip and the collimator coupled to the laser source fiber tip. The count rate to prevent the TCSPC photon count overflow (detail in 2.3.1 optical data acquisition - Data acquisition) was 170k photons per second. The distance between the source and detection fibers' tip, introduced by the thickness of ND filter and a paper sheet was negligible ($\approx 3\text{mm}$) and therefore, was not considered in the data analysis.

Fibers for simultaneous DCS and MRI scanning: The 8-m optical fibers connected to the optical hybrid DCS system were routed from a port in the control room through a tunnel in the scanner room (figure 2.9). The equipment used in the scanner room including the objective, prism, optical fiber, probe, and elastic bandage didn't have detectable magnetic susceptibility that could contaminate the MRI signal. This was verified in real time during the measurements using a monitor connected to the scanner. This real time monitoring allowed continuous observation while the subjects' head, muscle, and tissue-mimicking phantom were positioned in the MR coil.

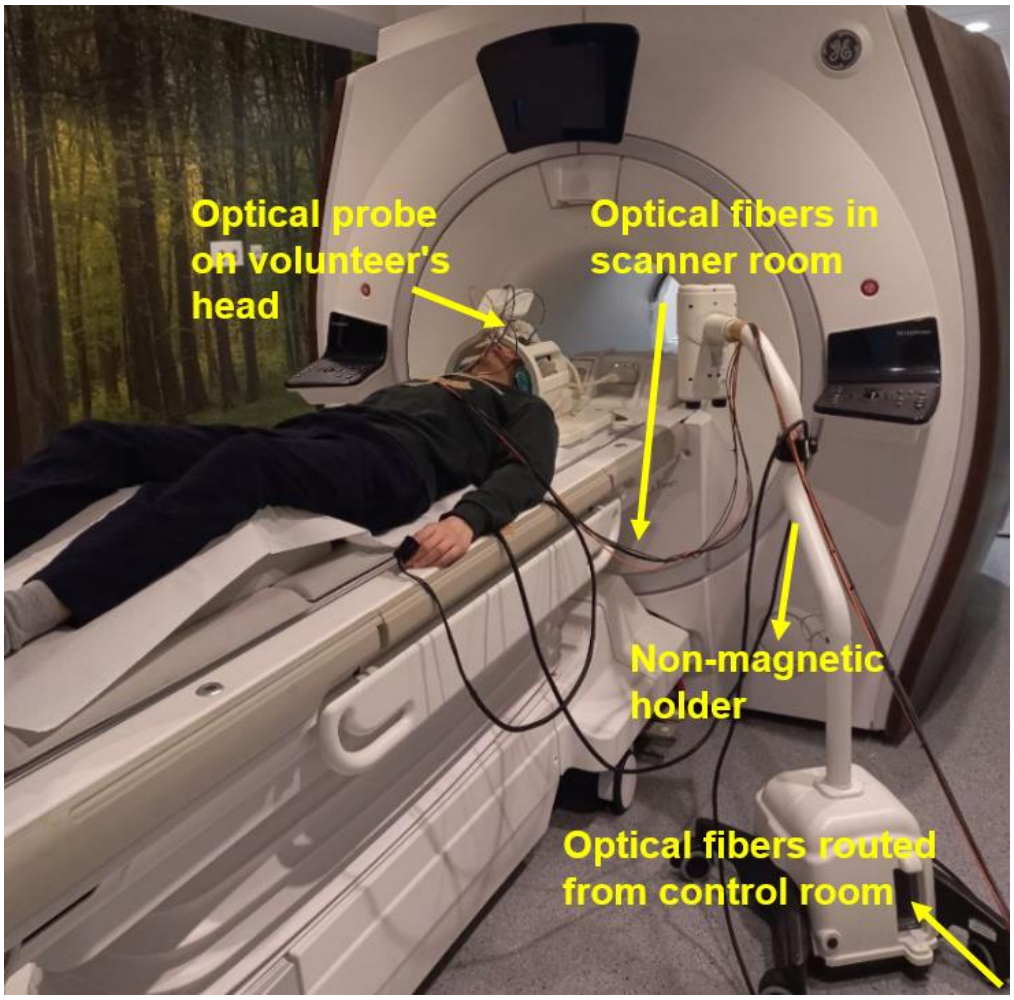


Figure 2.9 The 8-meter optical fibers were routed from control room to scanner room, mounted on a non-magnetic holder and were placed on the subjects' head. The pulse oximeter sensor was attached to the index finger of volunteers.

2.3 Data acquisition

2.3.1 Optical data acquisition

Data acquisition: The SPCM Data Acquisition Software (Multifunctional 64-bit Data Acquisition Software, Becker & Hickl) was used to record the signals. In SPCM, the FIFO (First-In, First-Out) mode, was used to time tag photons and record each individual photon's macro and micro time. An experiment can be run over a time of seconds, minutes, or hours. At the output, the FIFO memory is continuously read by the software. Because the number of bits to save the macro time is limited, the macro time may overflow during the recording. For photon numbers larger than the FIFO size the maximum average count rate is determined by the rate

at which the computer is able to read the FIFO. If the computer does not record the events on memory card faster than the photon detection events by SPAD, FIFO overflow can occur. FIFO overflow causes loss in counting photons and other information written into the FIFO during the measurement procedure [98]. The SPCM software can show the overflow warning during the data acquisition. Based on my experience during both phantom and in vivo measurements, if the photon counts excessed 170·000 counts per second, the overflow happened. In this study, to prevent overflow, the photon count rate was adjusted to be around 170·000 counts per second (detailed in next paragraph).

Experimental setup of evaluation the td-DCS performance at shorter and longer SDSs: The first series of the experiments were performed with the aim of optimization of the td-DCS part of the optical system, and to evaluate its performance at shorter (1.5 cm) and larger (2 and 2.5 cm) SDSs. As laser pulse shape and pulse width changes in various laser power, all measurements were conducted at the same laser power of 256mW. Therefore, the natural density filter (ND) filters were used at the laser output in order to attenuate the light. The measurements at each SDS required a different ND filter. To prevent FIFO overflow, ND filters were placed in front of the laser beam. However, for in-vivo measurements at larger SDSs, due to lower number of the detected photons, the FIFO overflow wasn't observed. To apply high laser power, a beam expander (F810SMA-780, Thorlabs) (figure 2.10 a) was used to enlarge the illumination area to 13mm in diameter which allowed to be in line with the safety regulations for the safe skin exposure as the averaged power density per unit time should not exceed 2.7 mW/mm^2 (at the wavelength of 760nm) [100]. The use of beam expander allowed delivery of light with averaged power density per time of 1.9mW/mm^2 to the sample surface. Manufacturer of the utilized beam expander reports Gaussian profile of light delivered by the beam expander. The power density was calculated from the ratio of the laser power (256mW) to the area illuminated by the beam expander. To improve the signal to noise ratio (explained in details in 2.5 Data analysis approaches - DCS techniques), four SPADs were used at each SDS. As shown in figure 2.10 b, the SDSs were measured from the centre of the illumination area to the centre of the SM fiber tip. All four SM fibers were located at the same SDS.

a



b

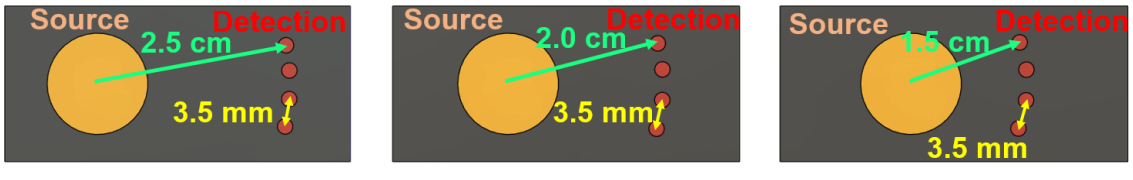


Figure 2.10 a) The position of the collimator (F810SMA-780) used as beam expander in the fiber holder. Here the SDS is 1.5cm. b) The top view of the fiber holder showing the fibers' position. The distances from source to detector are 1.5, 2 and 2.5 cm. The distance between the SM fibres' tips is 3.5mm which is the shortest possible distance due to the diameter of outside jacket of the fiber's.

Experimental setup of the cross evaluation of DCS and BOLD-MRI: Same as in the first series of experiments, the pulsed laser was applied with the averaged laser power per unit time of 256mW. A beam expander compatible for MRI environment was designed using Aspheric Lens (AL1512 - Ø15 mm S-LAH64, THORLAB, Germany) for td-DCS experiments. The shield to hold the lens was designed with the fusion Autodesk software and printed using Zortrax m200 3D printer (Zortrax, Poland). This custom designed beam expander was used again to increase the illumination area of pulsed laser to ~13mm diameter, to ensure the averaged laser power per unit time (1.9mW/mm²) remained below the safe threshold (i.e., < 2.7mW/mm²). To satisfy the tradeoff between sufficiently large SDS to detect photons penetrating deeper layers of the tissue and sufficiently enough number of detected photons, both cw-DCS and td-DCS [39] were applied at SDS of 2cm. The SDSs were estimated as a distance from the center of the expanded beam to the tip of the detection fibers (figure 2.11). To improve the signal to noise ratio in td-DCS technique (explained in details in 2.5 Data analysis approaches - DCS techniques), three SPADs were used to detect the signals. All three SM fibers were located at the same SDS. The signal from cw-DCS was detected using one SPAD.



Figure 2.11 a) The side view of designed cw-DCS and td-DCS beam expander. b) The schematics of cw-DCS and td-DCS optical probe with the fibers' position in the optical fiber holder. (c) The SDS was 2 cm and calculated from the center of the expanded beam to the tip of the detection fibers. In td-DCS probe, three SM fibers were located at the same SDS. The distance between the SM fibers was 3.5 mm which is the shortest possible distance due to the diameter of outside jacket of the fiber's. The length and width of the optical probes are $6 \times 3.5\ cm$ and the thickness is 2 mm.

Experimental setup of the cross evaluation of IVIM-MRI and cw-DCS: The third series of experiments were performed to cross evaluate the IVIM-MRI and cw-DCS in measuring tissue blood perfusion/flow. The picosecond pulsed laser and continuous-wave laser were used as the sources to measure optical properties and displacement of scatterers, respectively. Same as in the second series of experiment, a small prism was used to enlarge the illumination beam of the continuous wave laser. This solution enabled to use higher incident power of 60 mW while the applied power density of 0.6mW/mm² remained within safety limits for skin exposure [100]. To satisfy the tradeoff between sufficiently large SDS to detect photons which penetrated in the deep layers of the medium and sufficiently enough number of detected photons, the measurements were carried out at SDS 2 cm (detailed in 2.5.4 Intra voxel incoherent motion MRI - Region of interest of DWI image). To improve the signal to noise ratio (explained in details in 2.5 Data analysis approaches - DCS techniques), two SPADs were used. Two SM fibers were located at the same SDS (figure 2.12).

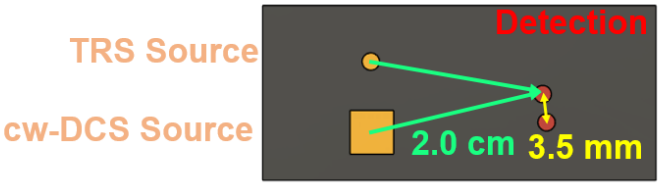


Figure 2.12 Schematics of the optical probe for simultaneous measurements of IVIM-MRI and cw-DCS. The SDSs were 2 cm and calculated from the center of the expanded beam to the tip of the detection fibers. Two SM fibers were located at the same SDS. The distance between the SM fibers was 3.5 mm which is the shortest possible distance due to the diameter of outside jacket of the fiber's. TRS: time resolved spectroscopy. DCS: diffusion correlation spectroscopy.

2.3.2 MRI data acquisition

***BOLD-MRI*:** The BOLD-MRI imaging was performed using the GE MRI Discovery MR750w magnetic resonance scanner with a magnetic field induction of 3T. An 8-channel head coil was used to acquire the signal. The T1-weighted sequence was an accelerated sagittal IR-FSPGR (Inversion Recovery – Fast Spoiled Gradient Echo), with the inversion recovery component applied to suppress the signal from fat tissue. In the T1 weighted image, the sequence parameters include a slice thickness of 1.2 mm, no spacing between slices, echo time (TE) of 2.92 ms, repetition time (TR) of 6.928 ms, and an inversion time of 400 ms in plane resolution. The flip angle was set to 11 degrees to optimize the signal-to-noise ratio and tissue contrast. The T2 weighted sequence images were acquired with a slice thickness of 1.2 mm, 0.6 mm spacing between slices, TE of 87ms, and a TR of 2.5 seconds. The protocol employed a 90-degree flip angle and echo train length of 100. T2-weighted images were acquired as supplementary data to support comprehensive radiological assessment. The CUBE T2 sequence reconstruction matrix was interpolated using zero filling method from 320×320 to 512×512 which resulted in 0.5×0.5 plane resolution. The voxel bandwidth in both structural images was set to 244 Hz. The MRI sessions were acquired using an echo planar imaging sequence with a TR of 2.5 s, TE of 25 ms, slice thickness of 3 mm, and no gap between slices. The field of view (FOV) was 19.2 × 19.2 cm, with both acquisition and reconstruction matrices set to 64 × 64 pixels, resulting in an in-plane resolution of 3 × 3 mm² and isotropic voxels of 3 × 3 × 3 mm³. A total of 47 slices and 144 volumes were acquired.

***IVIM-MRI*:** IVIM-MRI measurements were performed using a 3T GE Discovery MR750w scanner (GE Healthcare, USA) equipped with an 8-channel knee coil. The MRI data acquisition included 17 non-zero b-values (10, 20, 30, 60, 90, 120, 150, 180, 210, 240, 300, 500, 700, 1000, 1200, 1350, 1500 s/mm²), measured in three orthogonal directions and one b_0 image [102]. *b*-value refers to the weighting of the diffusion of the MR pulse sequence and is determined by the magnitude and timing (duration and separation) of the diffusion gradients [103, 104]. It was tried to select b-values that were accessible on the scanner and were close to an optimized set [105]. A single-shot 2D echo-planar imaging DWI sequence was used to acquire the data. Each acquisition took approximately 2 minutes for both phantom and muscle occlusion experiments.

The imaging parameters of the tissue mimicking phantom imaging were as follows: TR = 4000 ms, TE = 69.4 ms, FOV = 64 × 128 mm², slice thickness = 10 mm, in-plane resolution = 2 × 2 mm², matrix size = 32 × 64, number of excitations = 4 (This parameters represent the

number of times each line of k-space data is acquired and are primarily used to improve the signal-to-noise (SNR) ratio), and Pixel Bandwidth= 7812.5 Hz/px. The MRI scanner room temperature was maintained at 22°C during the entire of phantom imaging.

The imaging parameters of muscle occlusion test were as follows: TR = 6000 ms, TE = 97.1 ms, FOV = 128 × 128 mm², slice thickness = 10 mm, in-plane resolution = 2 × 2 mm², matrix size = 64 × 64, number of excitations = 1, and Pixel Bandwidth = 7812.5 Hz/px.

2.4 Experimental protocols

2.4.1 Physical phantom

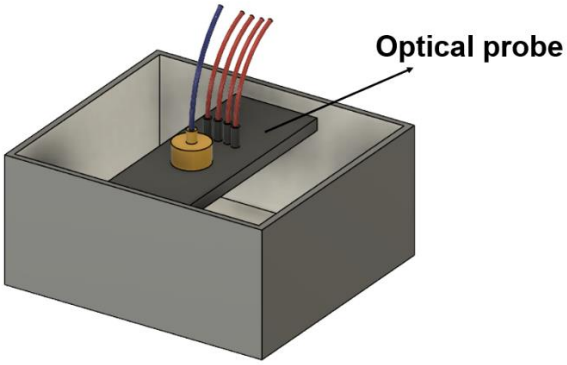
Homogenous and Two-Layered Phantoms: A one-layered (homogenous) (Figure 2.13 a) and two-layered (Figure 2.13 b) 3D containers were designed using fusion Autodesk software and printed using Zortrax m200, from black ABS material. The two-layered container was designed with various superficial layer thicknesses. The layers were separated using a transparent thin film (Mylar sheet with the thickness of 23 μm). The thickness of superficial layer was set to be 0.5 cm, 1 cm and 1.5 cm according to the typical scalp and skull thickness of adults' head following [106, 107].

The mixtures to fill the containers, were made using a lipid-based liquid SMOFlipid (Fresenius Kabi, Poland), distilled water, as well as glycerol (Vegetable Glycerin 99.5% pharmaceutical grade, Bioswena, Poland) to slow down the displacements of scatterers in the phantoms. SMOFlipid is a highly scattering fatty emulsion that consists of spherical oil droplets within a lipid membrane with $\sim 0.5\ \mu m$ diameter [108]. The mixtures representing the $\alpha D_{\mathrm{b}}^{\mathrm{fast}}$ and $\alpha D_{\mathrm{b}}^{\mathrm{slow}}$ were prepared without glycerol and using the 40% glycerol concentration, respectively. As the absorption properties of the medium has minor influence on the recovered αD_{b} [84], no absorber was added to the mixtures. To adjust the desired reduced scattering coefficient, different concentrations of SMOFlipid were added to each mixture according to the recipe described in [109, 110]. The optical properties of all phantoms, measured by time domain part of the optical hybrid system, were μ_{a} = 0.003 mm^{-1} and μ'_{s} = 1 mm^{-1}.

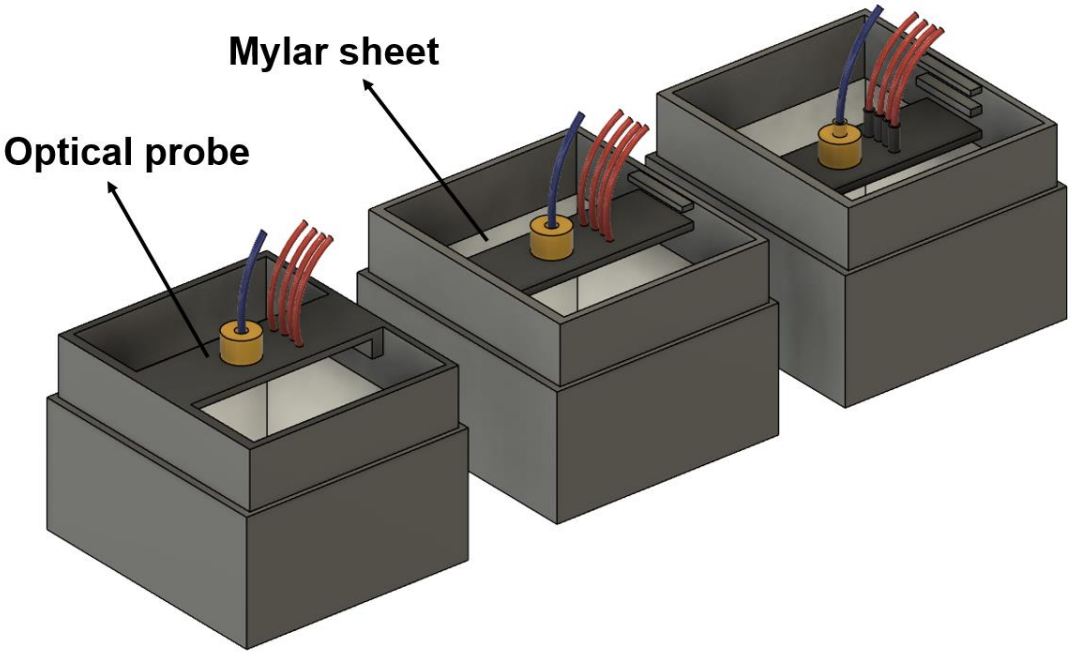
For td-DCS characterization at shorter (1.5 cm) and larger (2 and 2.5 cm) SDSs, three series of phantom measurements were conducted. First, the αD_b of the two homogenous phantoms with 40 and 0 % glycerol concentration were measured separately. Then measurements were performed on the two-layered phantom, with 40% glycerol concentration in the superficial layer

and no glycerol in the deep layer. In the final step, the top layer was filled with a mixture containing no glycerol, and the 40% glycerol mixture was used to fill the deep layer. The measurements on two-layered phantom were performed at three different top layer thicknesses at each three SDSs.

The cw-DCS and td-DCS ability to recover the αD_b changes in superficial and deeper layer of two-layered phantoms were also evaluated and compared. To do that the same series of measurements were conducted at three different top layer thicknesses, however at the fixed SDS of 2 cm.



a



b

Figure 2.13 Schematic of containers used for a) homogenous phantom and b) two-layered phantom with possibility to put the optical probe in various distance from the Mylar sheet, to mimic upper layers with different thicknesses. The container was filled with mixture to match the level of fluid with the upper surface of the optical probe.

Tissue Mimicking Phantom: To cross evaluate the parameters measured by IVIM-MRI and flow index measured by cw-DCS in monitoring the water molecules and scatterer displacements within a controlled medium, a series of measurements were performed on a tissue-mimicking phantom. A 3D container was designed using fusion Autodesk software and printed using Zortrax m200 from black ABS material. The container was designed with parallel holes to pass the transparent silicon tubes with the inner diameter of 1 mm representing a simplified model of tissue with vessels. The phantom was designed with three rows of tubes located at different depths in respect to the probe. The first, second, and third rows of tubes were placed at depths of 0.5, 1, and 1.5 cm from the surface of the mixture, respectively. The tubes were threaded multiple times through the phantom, bending around the structure to ensure identical and controlled flow rates in all segments (figure 2.14 a). The distances between the centers of tubes was 1 cm.

Within a liquid only the Brownian motion of scatterers is expected to occur. In order to mimic the blood flowing through the vessels, silicon tubes were connected to a programmable syringe pump (NE-1000 Programmable Single Syringe Pump), which permits generating the desired pump flow rates (F_{pump}). In this study, six F_{pump} of 1 to 6 mm^3/s with the step of 1 were applied within the tube. The F_{pump} were calculated from the multiplication of $A_{\text{cs}} \times V_{\text{pump}}$ [111] where $A_{cs}(\text{mm}^2)$ and $V_{\text{pump}}(\text{mm/s})$, refer to the cross-sectional area of the tube and the pump velocity respectively. Each series of measurement including baseline and six F_{pump} was repeated five times to ensure the repeatability. The outflow was connected to a reservoir and allowed to drain freely.

The container was filled with an agar-gel mixture, doped with $NiCl_3$ (figure 2.14 c). To prepare the mixture, it was heated while being stirred to completely dissolve the agarose. Then the SMOFlipid 20 (Fresenius Kabi) was added to the mixture to obtain a turbid material with reduced scattering coefficient of μ'_s = 1 mm^{-1} and absorption coefficient of μ_a = 0.003 mm^{-1}. The mixture was poured into the container to cool down and solidify. The liquid mixture to pump through the tubes was also prepared using SMOFlipid as the scatterers (i.e., mimicking the RBCs) and distilled water. Since the absorption property of the sample doesn't significantly affect the scatterers displacements and consequently recovered αD_{b} [84], no absorber was added to the mixtures. The measured optical properties of these mixtures were μ_a = 0.003 mm^{-1} and μ'_s = 1 mm^{-1}. The optical properties were measured by time domain part of the optical hybrid system.

Before each measurement, the entire phantom was visually inspected for air bubbles and vented if necessary. The source and detector fibers of cw-DCS technique, were confined in a black 3D printed holder and were placed on the surface of the container. The distance between the first raw of tubes and the optical fiber's tip was 5 mm. As reported in [112], the position of the source and detector, parallel or perpendicular to the tubes' direction doesn't significantly influence the FI_{DCS}.

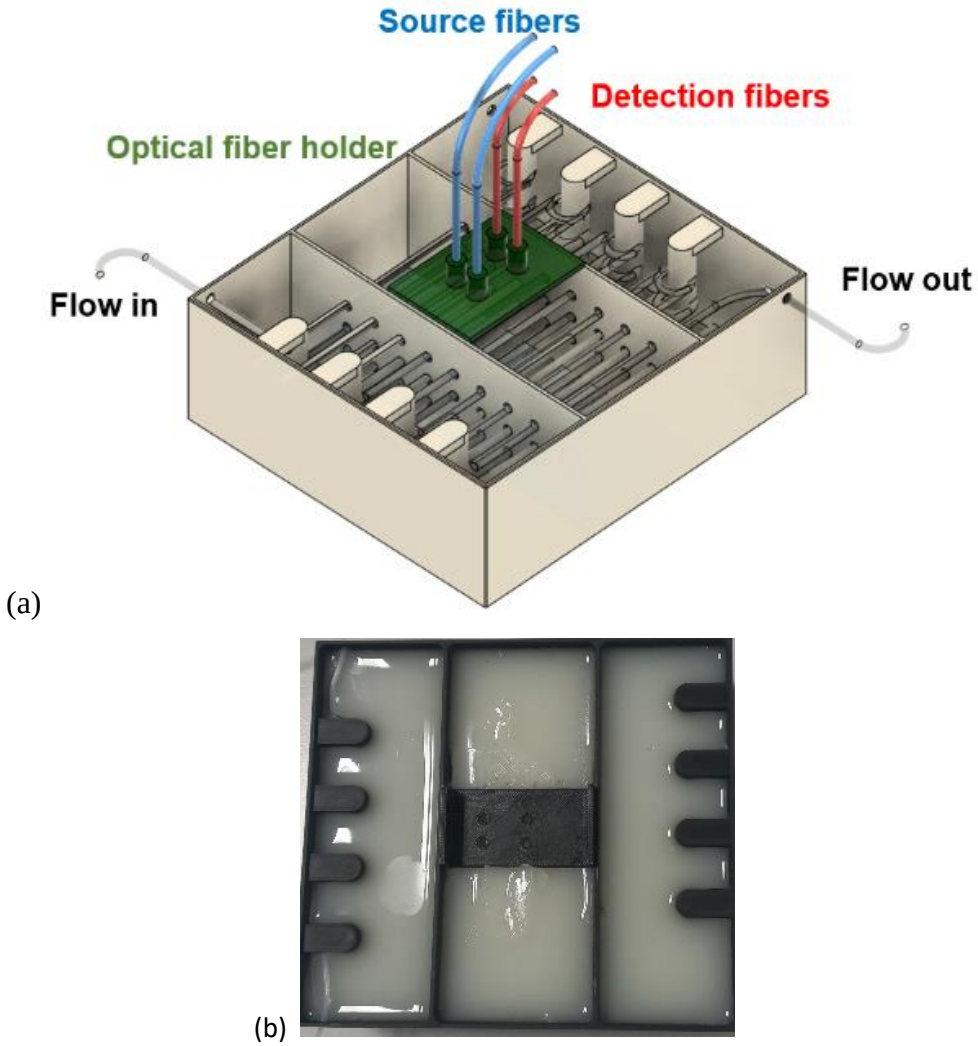


Figure 2.14 a) The tissue mimicking phantom has the dimension of dimension of $16 \times 14 \times 5.5$ cm in length, width, and depth respectively. b) The top view of the container filled with the agar-gel mixture doped with $NiCl_3$. The mixture filled the container to match the level of fluid with the lower surface of the optical probe.

In diffusion theory, the zero-boundary (or extrapolated zero) condition assumes that when photons reach to the boundary of medium, they are absorbed. However, in the homogenous, two-layered and tissue mimicking phantom utilized in this study, the upper part of phantoms, where the optical probe is located, is open. Therefore, some photons may scatter out or inside

the phantom from the surface of mixture which doesn't satisfy the zero-boundary condition. However, not fulfilling this condition has minimal effects on the results of measurements.

2.4.2 In vivo experiments protocol

Muscle occlusion test: The occlusion trial involves placing a cuff pressure (tourniquet) around the upper arm (or forearm), inflating it to occlude arterial and/or venous blood flow for a certain duration, then releasing it. This causes a transient period of ischemia (reduced flow), followed by a reactive hyperaemia (flow increase) once the cuff is released [113, 114]. The occlusions were obtained using a standard leg and arm occlusion cuff with air pump allowing to pump the cuff to a defined pressure manually. The widths of occlusion cuff for leg and arm were 12 and 17 cm, respectively.

Respiratory challenges: Hypercapnia or Breath hold (BH) is a state of elevated carbon dioxide levels in the blood and is usually caused by breathing slower than normal or stop breathing. BH results in vasodilation and increasing the CBF. Conversely, hypocapnia or Hyperventilation (HV) is a state of decreased carbon dioxide in the blood, generally resulting from deep and rapid breathing than normal. HV is usually achieved by inducing mild to severe hypocapnia, which involves reduction in partial pressure of arterial carbon dioxide (PaCO2) in the brain [115, 116]. HV induces significant vasoconstriction in cerebral arterioles and decreasing CBF and cerebral blood volume [117]. BH and HV are systemic rather than regional or local stimulations that induce cerebrovascular responses. They are commonly used to evaluate the ability of DCS systems to monitor CBF changes [118, 119], as well as in BOLD-MRI studies of cerebral hemodynamics [120, 121]. Previous studies involving healthy volunteers have shown that such BH and HV protocols do not cause significant discomfort under the protocols performed in this study [122, 123]. The Valsalva maneuver is a forced expiratory effort against a closed airway, usually done by trying to exhale forcefully while keeping the mouth and nose closed [124].

Bioethical approval: The study protocol received approval from the Bioethics Committee of the Military Medical Chamber in Warsaw, Poland (Approval No. 17/23). All participants gave written informed consent and signed the study agreement prior to enrolment.

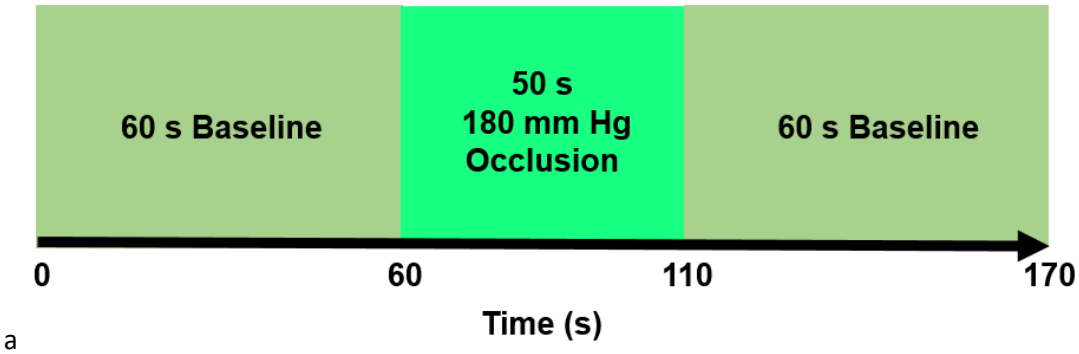
In vivo measurements protocol for comparison of td-DCS performance at shorter and larger SDSs: To evaluate the measured BFI by td-DCS at three different shorter (1.5 cm) and longer (2 and 2.5 cm) SDSs, the occlusion test was performed on the forearm of healthy adult

volunteers, separately in both left and right arms. Data in each occlusion test was acquired using the following time acquisition: 60 s baseline followed by 40 s arterial occlusion (180 mmHg cuff pressure) and 60 s release (Figure 2.15 a). This protocol was repeated twice at each SDS separately. Four healthy adult volunteers (three females, one male, mean age 32 years) participated in this study.

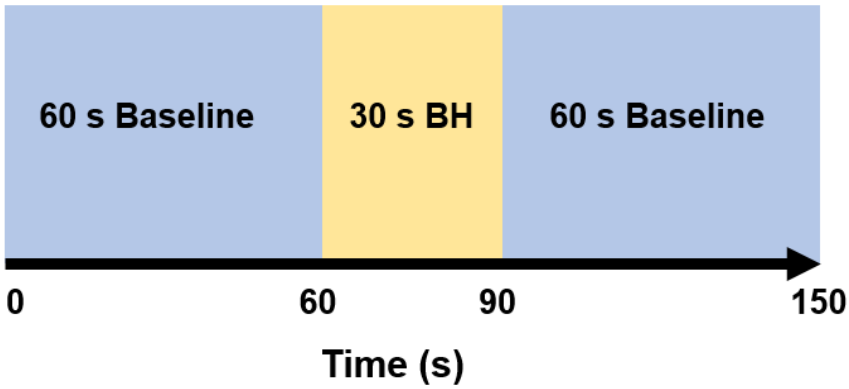
To evaluate td-DCS performance at shorter (1.5 cm) and larger (2 and 2.5 cm) SDSs in monitoring the CBF changes, the BH and HV respiratory challenges were performed by volunteers, which respectively elevate and decrease intravascular deoxyhemoglobin (HbR) concentrations [125, 126]. Following, the volunteers were asked to do Valsalva maneuver.

The BH task consisted of a 60-second baseline, 30-second breath-hold without initial inspiration or expiration, and 60-second recovery (figure 3.15 b). The HV task began with a 60-second long baseline, followed by a 40-second effort to exhale and inhale fully to maximize respiratory exchange ratio and recovery in the 60s (figure 3.15 c). The Valsalva task began with a 60-second baseline period, followed by a 20-second forced exhalation while keeping the mouth and nose closed, and ended with a 60-second recovery period (figure 3.15 d). Each task was repeated twice in each trial for each SDS.

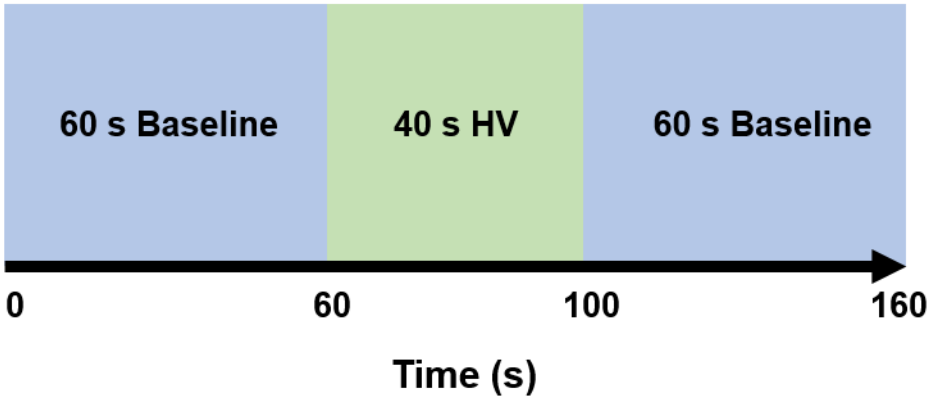
Six healthy adult volunteers (four females and two males, mean age $36 \pm SD$ years) participated in BH and HV respiratory challenges and four of them were able to perform Valsalva manoeuvre successfully. In both occlusion and respiratory challenges volunteers were sitting on an armchair with body angle of almost 130^{o}.



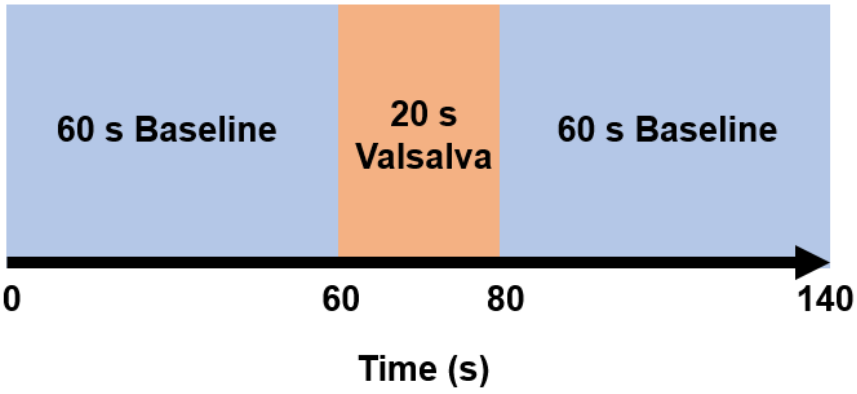
a



b



c

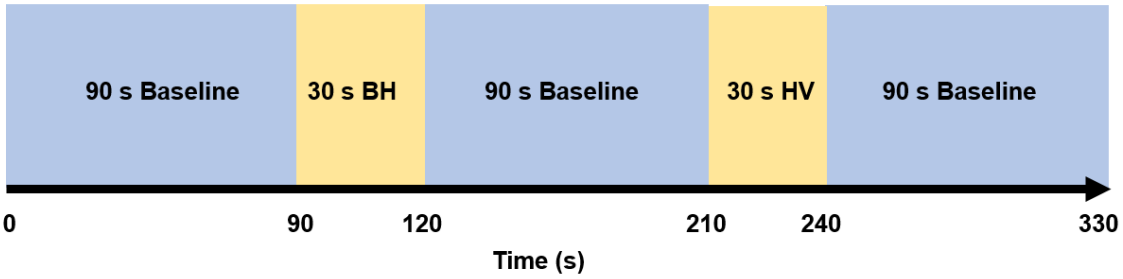


d

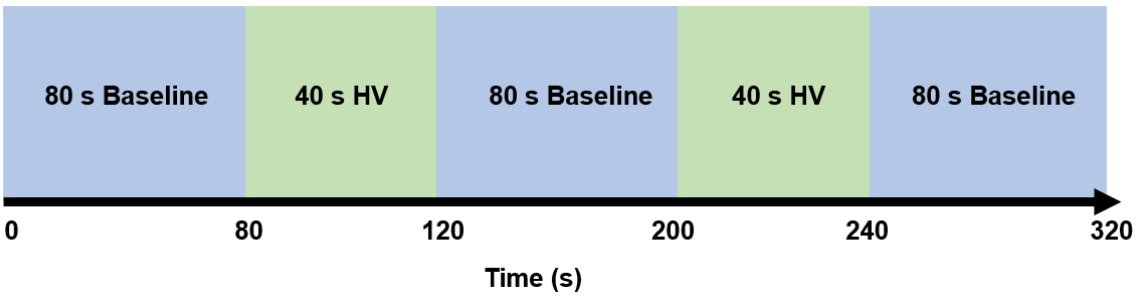
Figure 2.15 The schematics of measurement protocols for a) forearm occlusion test, b) BH test, c) HV test, and d) Valsalva used for evaluation of the td-DCS performance in monitoring the tissue blood flow changes at different SDSs.

In vivo measurements protocol to evaluate the correlation of Hemodynamic Responses Measured by DCS and BOLD-MRI: In order to evaluate the cross correlation between the hemodynamic response measured by cw-DCS and td-DCS with BOLD-MRI, the respiratory challenges of BH and HV were performed by volunteers. BH protocol involved two cycles, each consisting of 90 seconds of normal breathing followed by 30 seconds of breath-holding (figure 2.16 a), during which participants were instructed to not take a deep breath beforehand. The HV task included two repetitions of 80 seconds of self-paced breathing followed by 40 seconds of hyperventilation (figure 2.16 b). During self-paced breathing, participants breathed normally, while during HV, they were instructed to breathe more deeply.

During data acquisition, participants viewed visual cues, projected from the control room onto a screen positioned at the end of the scanner bore. These visuals were made visible via a mirror mounted on the RF coil above the subject's eyes. The experimental protocol and visual guidance were managed using Presentation® software (Version 23.0, Neurobehavioral Systems, Inc., Berkeley, CA).



a



b

Figure 2.16 measurements protocols performed by volunteers a) BH and b) HV to evaluate the correlation of the hemodynamics responses measured by cw-DCS and td-DCS with BOLD-MRI.

To evaluate the correlation between cw-DCS and td-DCS with BOLD-MRI technique, sixteen healthy adult participants (8 males and 8 females, average age of 37 years) with no known vascular conditions, were enrolled in the study. All measurements were conducted while subjects were lying in a supine position inside the MRI scanner (figure 2.17). To minimize the motion artefacts, subjects were instructed to not move throughout the procedure of respiratory

challenges, and their heads were securely stabilized within the RF coil using pillows. Simultaneous with applying the DCS modalities and BOLD-MRI technique, the peripheral oxygen saturation (SpO_2) level and the heart rate (HR) were monitored using a pulse oximeter (Nonin 7500FO, USA). The sensor clamp of pulse oximeter which includes both light emission diode and detector, was gently attached to the tip of the left-hand index finger of volunteers.



Figure 2.17 A volunteer in supine position on the MRI bed. Both cw-DCS and td-DCS parts were housed in one instrument rack and placed out of the scanner room.

In vivo measurements protocol for cross evaluation of the IVIM-MRI and DCS in measuring tissue blood perfusion/flow: To cross-evaluate the IVIM-derived perfusion/flow parameters with BFI measured by cw-DCS, the venous occlusion (60 mmHg) and arterial occlusion (180 mm Hg) were performed on the volunteers' muscle, to have a period of ischemia response [41, 127]. This paradigm included 5-minute baseline (required time for IVIM-MRI pre-scanning), a 3 min of venous occlusion, followed by 2 min of baseline, and 3 min of arterial occlusion (figure 2.18). These occlusion times were set based on the required time to capture the full IVIM imaging sequence.

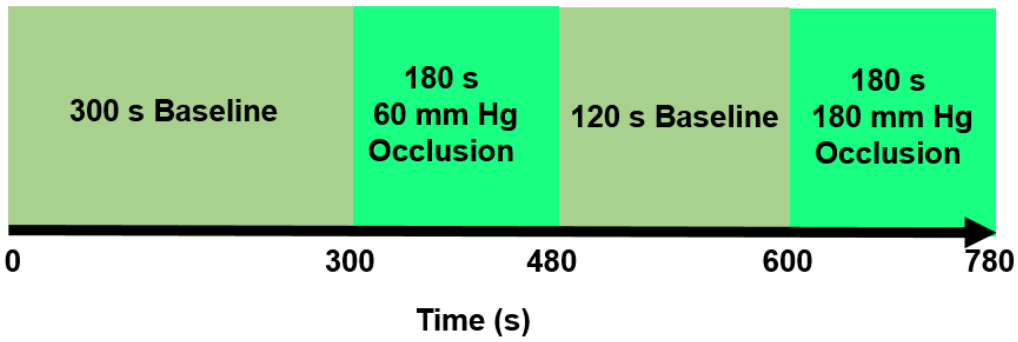


Figure 2.18 The schematics of protocol for leg and forearm occlusion used for cross-evaluation of the IVIM-derived parameters with BFI measured by cw-DCS.

Five healthy adult volunteers (three males, two females) with an average age of $35 \pm SD$ years participated in the muscle occlusion tests to evaluate IVIM-MRI and cw-DCS techniques in monitoring the tissue blood perfusion/flow. The occlusion tests were performed on the volunteers' leg and forearm while they were investigated in prone position in the tunnel of the MRI scanner. To reduce the motion artifacts, volunteers were instructed to not move during data acquisition. Moreover, the subject's muscles were tightly fixed to Knee coil using a pillow.

Optical Probe Placement on the Volunteer's Forearm, Head and Leg: The probes to hold the optical fibers were made from flexible silicone material and secured to the subject's head and muscles using an elastic bandage.

For cuff occlusion test to evaluate td-DCS performance in measuring BFI at shorter (1.5 cm) and larger (2 and 2.5 cm) SDSs, the optical probe was fixed on the volunteers' forearm (Figure 2.19 a). To evaluate td-DCS at shorter and larger SDSs in monitoring CBF changes, the optical probe was located at the left side of the frontal lobe of the healthy volunteers [79, 119], approximately 1 cm above the eyebrow (Figure 2.19 b). The midline region was intentionally avoided due to the presence of major vascular structures, such as the sagittal sinus, which have high optical absorption and could cause excessive signal attenuation [128].

To cross-evaluate cw-DCS and td-DCS techniques with BOLD-MRI technique in monitoring the cerebral hemodynamic responses, the optical probes should be placed in the same tissue regions [119, 129]. Given that BH and HV tasks are expected to induce comparable hemodynamic responses across left and right hemispheres in healthy individuals. Therfore, optical fiber probes were symmetrically positioned 1 cm above the eyebrows on the left and right sides of the forehead (Figure 2.19 c). The MRI head coil had openings that allowed probe placement on the volunteers forehead. A fiducial marker (Vitamin E capsule) was placed over each optical probe of cw-DCS and td-DCS, between the source and detection fibres' tip, to

enable precise localization of the probe positions and optical fiber the on anatomical MRI scans (Figure 2.19 d).

For simultanous monitoring of blood perfusion/flow changes using IVIM-MRI and cw-DCS techniques, the probe was positioned over the gastrocnemius muscle of the leg (figure 2.19 e) and the extensor muscle of the forearm (figure 2.19 f). Since the MRI knee coil did not have openings to couple the optical fibres to the subject's muscles, the probe was placed just at the edge of the coil.

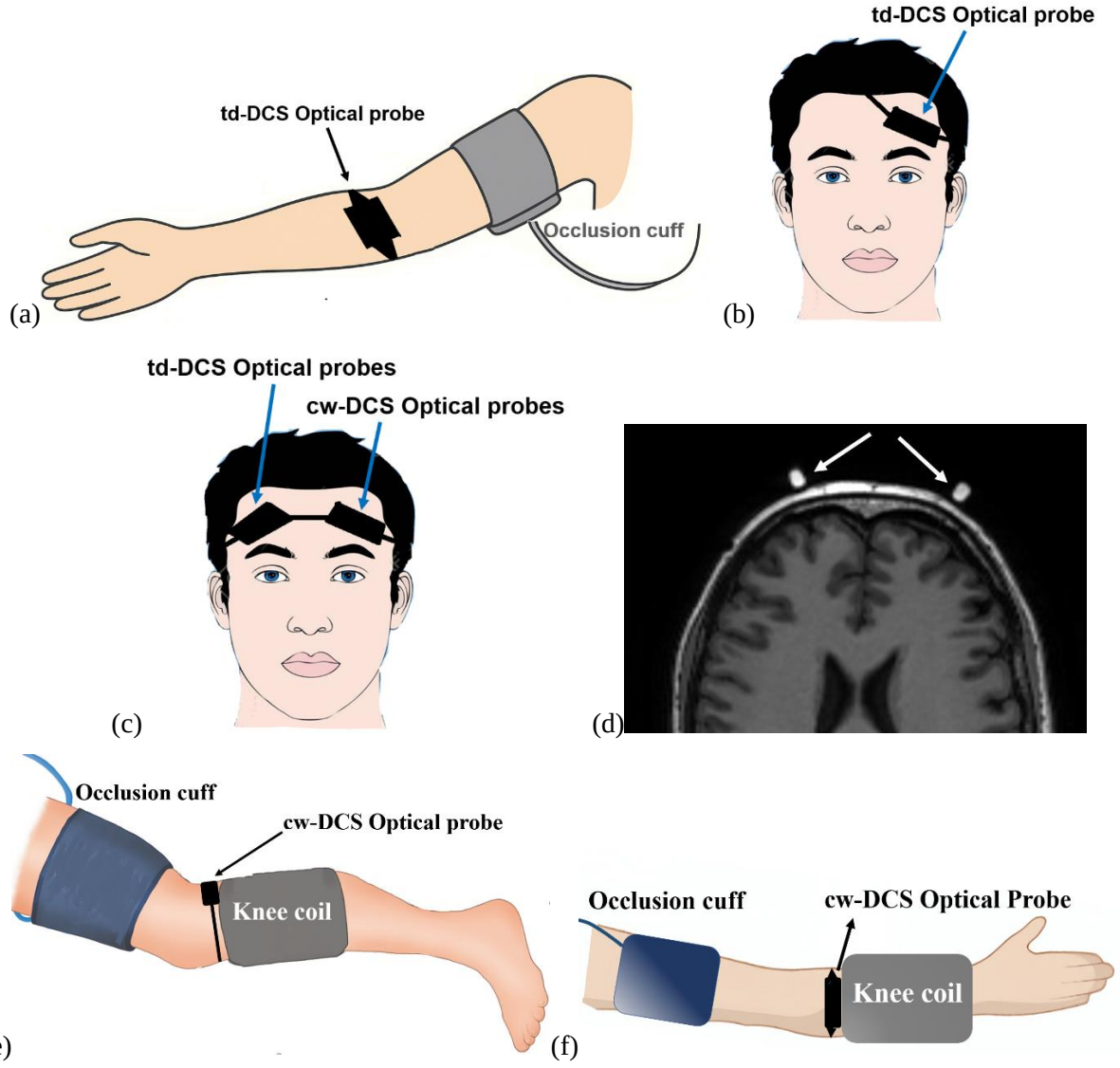


Figure 2.19 The position of td-DCS optical probes a) on the flexor compartment of volunteer's forearm and b) forehead. c) Position of optical probes on the volunteer's forehead while simultaneous measurements of cw-DCS and td-DCS with BOLD-MRI technique. d) The white circles in the MRI image refers to the vitamin E as a marker to determine the place of optical fibres. The vitamin E were located between the source and detection fibres on each optical probe of cw-DCS and td-DCS. Position of optical probes on the e) gastrocnemius compartment of the leg and f) extensor compartment of forearm while simultaneous measurements of cw-DCS and IVIM-MRI.

2.5 Data analysis approaches

2.5.1 Derivation of optical properties

The method used in this study for the retrieval of the optical properties of the phantoms and tissue was based on the moments, i.e. mean time of flight, and variance of the DTOF [70]. In the moment approach, the zeroth order of statistical moment refers to the total number of detected photons. The first and second order of statistical moments correspond to the mean time of flight of photons m_1 $(< t_s >)$ and variance $(V =< {t_s}^2 > - < t_s >^2)$ of the DTOF. The advantage of this approach lies in its ability to correct the influence of the IRF. To deconvolve the influence of the IRF, the moments of the IRF were subtracted from the moments of the measured DTOF. The subtraction of moments was applied for both mean time of flight and variance [70, 130].

The statistical moments of the DTOFs obtained from each data acquisition of phantom and in-vivo measurements, were utilized to estimate the absorption coefficient (μ_a) (equation 2.12) and reduced scattering coefficient (μ'_s) (equation 2.13) , detailed in [70]. The DTOFs range for calculating the optical properties was defined from 5% of the DTOF peak on the rising edge to 1% on the falling edge [131].

$$\mu_a = \frac{m_1^3}{2cV(m_1^2 + V)} \qquad (2.12)$$

$$\mu_s' = \frac{2m_1 c(m_1^2 + V)}{3\rho^2 V} \qquad (2.13)$$

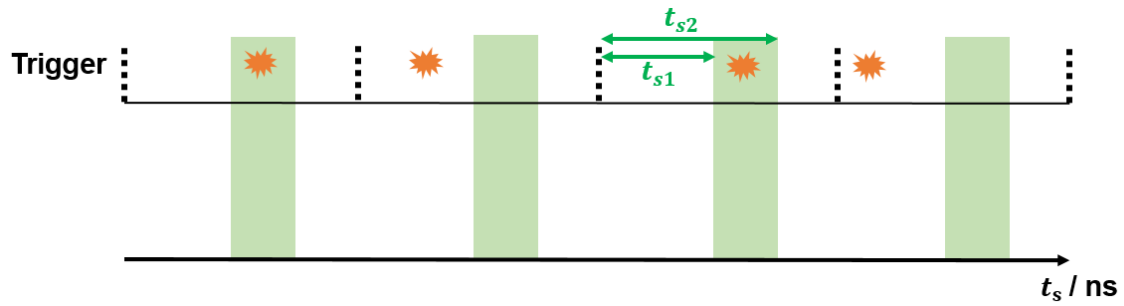
Where ρ is the distance between the source and detector (figure 2.1) and c is the speed of light in the medium.

Although tissue optical properties can vary slightly during respiratory challenges and occlusion tests, previous studies have shown that low-magnitude changes have minimal impact on the recovered αD_b [84], and consequently on the BFI. Therefore, constant μ_a and μ_s' were assumed throughout the entire in-vivo experiment, including both baseline and challenge periods to calculate the BFI.

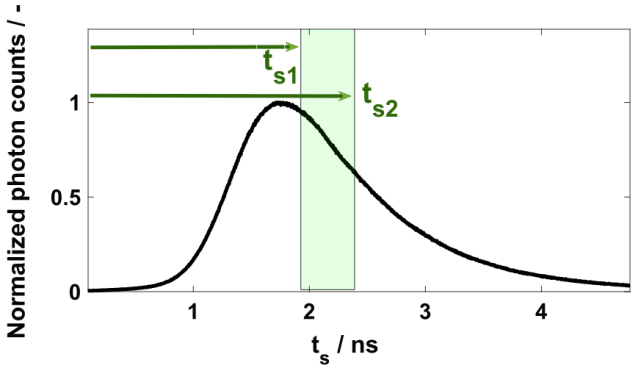
2.5.2 DCS techniques

In this section, the data analysis procedures applied to cw-DCS and td-DCS measurements has been described. These analyses were performed to calculate the αD_{b} in the homogenous, two-layered and tissue-mimicking phantom, as well as the BFI changes of muscle tissue and cerebral layer.

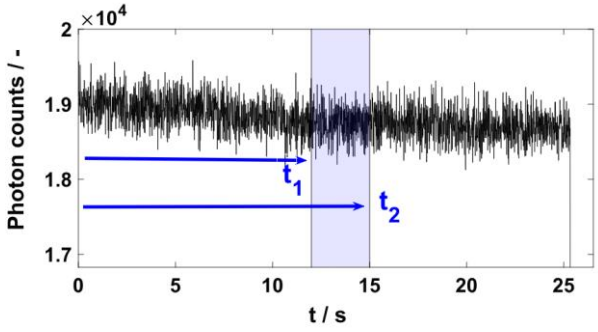
DCS data pre-possessing: Figure 2.20 illustrates the pre-data processing approach used to analyze the td-DCS acquired data. The TCSPC records two photon detection events: 1) The time of flight of photons (t_s) which refers to the time between the pulse of laser light and the photon detection event (micro time). The rigger signals denote to the time when the pulse of laser light is emitted (figure 2.20 a). Then DTOF can be calculated from the histogram of the number of photons across the time-of-flight (figure 2.20 b). 2) The precise absolute arrival time (t) of photons since the start of the measurement (macro time). The time range between t_1 and t_2 (blue rectangular area in figure 2.20 c) determines the integration time (detailed in 2.2.2 DCS techniques, integration time). The photons detected within the specific time of flight between t_{s1} and t_{s2} (green rectangular area in figure 3.20 b), specific absolute arrival time range between t_1 and t_2 (blue rectangular area in figure 2.20 c) are used to calculate the autocorrelation function (figure 2.20 d).



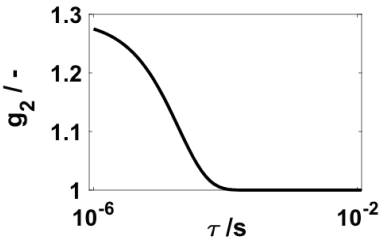
a



b



c



d

Figure 2.20 Sketch of the td-DCS data pre-processing approach. a) The temporal positions of the detected photons (orange asterisks) shown together with the trigger pulses generated by the laser driver, the rectangular green area shows the position of the gate, limited by specific times of flight photons between t_{s1} and t_{s2}. b) The DTOF is obtained by building a histogram of photon counts as a function of t_s, same as in (a) the rectangular green area shows the position of the gate limited by specific times of flight photons between t_{s1} and t_{s2}. c) The number of photons counted during the measurement. The rectangular blue area shows a 3 s integration time (between absolute arrival times of t_1 and t_2). d) The intensity autocorrelation function is obtained from the photons detected within the specific time of flight (between t_{s1} and t_{s2}), and specific absolute arrival time (t_1 and t_2), where τ is the lag time.

cw-DCS fitting scenarios: For data analyses related to cw-DCS, two fitting scenarios were applied to estimate the αD_{b} and BFI: (1) fitting the electric field autocorrelation function derived from theory $g_1(\tau)$ to the whole autocorrelation function $(0 < g_1(\tau) < 1)$ of the measured data (figure 2.21 a), and (2) fitting the theoretical $g_1(\tau)$ only to the early portion of the measured $g_1(\tau)$, in order to improve the sensitivity of the measurement of αD_b to flow changes appearing in deeper layer of the medium (figure 2.21 b). Restricting the fit to the early lag times is known to give more weight to photons with longer paths and higher αD_{b} [32]. Therefore, it may increase the contribution from the photons penetrating in the deeper layers of the tissue to the detected signal. To do that, first, the threshold decay was computed for $g_1(\tau) > 0.7$ of the measured data. Then the $g_1(\tau)$ curve from theory was fitted to the $g_1(\tau) > 0.7$ of the measured data in the range of threshold decay [32].

The flow index of the tissue mimicking phantom (FI_{DCS}) and the BFI of the muscle tissues (BFI_{DCS}) in cw-DCS and IVIM-MRI cross evaluation experiments, were calculated from fitting the electric field autocorrelation function $g_1(\tau)$ derived from theory, to the whole autocorrelation function $(0 < g_1(\tau) < 1)$ of the measured data. To improve the signal to noise ratio of cw-DCS technique, in simultaneous cw-DCS and IVIM-MRI experiments, the g_1 used to calculate the αD_{b} and BFI was averaged from the g_1 obtained from signals measured by the two SPADs.

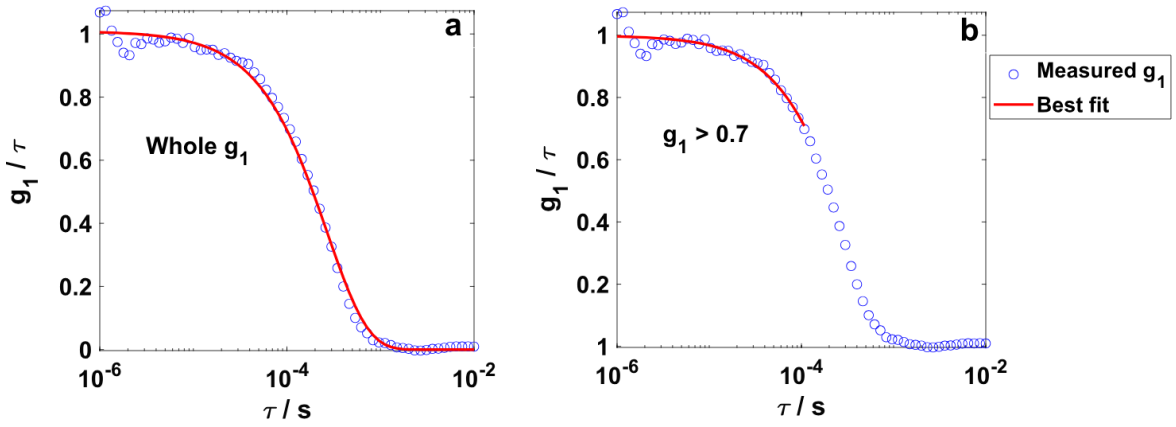


Figure 2.21 Two fitting scenarios were used to estimate the αD_b and BFI. a) Fitting the theoretical $g_1(\tau)$ the whole measured $g_1(\tau)$, b) Fitting the theoretical $g_1(\tau)$ only to the early portion of the measured $g_1(\tau)$ (i.e. for $g_1(\tau) > 0.7$).

Time gating strategy in td-DCS: In data analyses related to td-DCS technique, photon selection based on time of flight, named time gating strategy [29] was applied. This strategy distinguishes

between the short and long photon paths and classifies the αD_b of superficial and deeper layers of the medium. In time gating strategy, gate start time is critical parameter that directly influence the recovered αD_b of the superficial and deeper layer. This parameter defines the start of the gate which photons are collected and analysed based on TOF. Setting an appropriate gate start time helps to exclude photons that have only travelled through superficial layers, and improving the focus on changes in αD_b appearing in the deeper layer. Temporal gate refers to the time range in which photons are collected and defines the range of DTOF to be analysed. Increasing the gate width can increase the number of photons and improve the signal to noise ratio, however it may lead to mixing the signals related to photons that penetrate at different depths. Narrow gate width increases the probability of selecting photons with specific TOF and path length. But it significantly reduces the number of detected photons, thereby decreasing the signal-to-noise ratio. So, the balance in gate width to have enough number of photons to improve signal to noise ratio and narrow enough to isolate photons with specific path length is necessary.

In this study a medium-specific time gating strategy was applied. In this approach two time gates were defined to isolate the signals of scattered photons from superficial and deeper layers. The early gate starts with the width of FWHM/2 before the DTOF peak on its rising edge and ends at the DTOF peak. The late gate starts at the DTOF peak and ends with the width of FWHM/2 on the falling edge [39] (figure 2.22 a). Consequently, the calculated g_1 from detected photons in early and late gate (figure 2.22 b) are corresponding to αD_b changes in superficial and deeper layer. These gates are based on the FWHM of DTOF, and depend on the optical properties of the medium and SDS. In "4.1 Comparison of td-DCS performance at shorter and larger SDSs – Physical phantom, these gates performance in recovering the αD_b have been discussed. In this study, due to subject-specific variations in DTOF broadening, the gate widths derived with the approach described above, ranged from 450 to 550 ps.

To improve the signal to noise ratio of the td-DCS technique in measurements at shorter and larger SDSs, the g_1 used to calculate the αD_b and BFI was averaged from the g_1 measured using four SPADs. Similarly, during simultaneous measurement of td-DCS and BOLD-MRI techniques, the g_1 used to calculate the αD_b and BFI was averaged from the calculated g_1 of three SPADs.

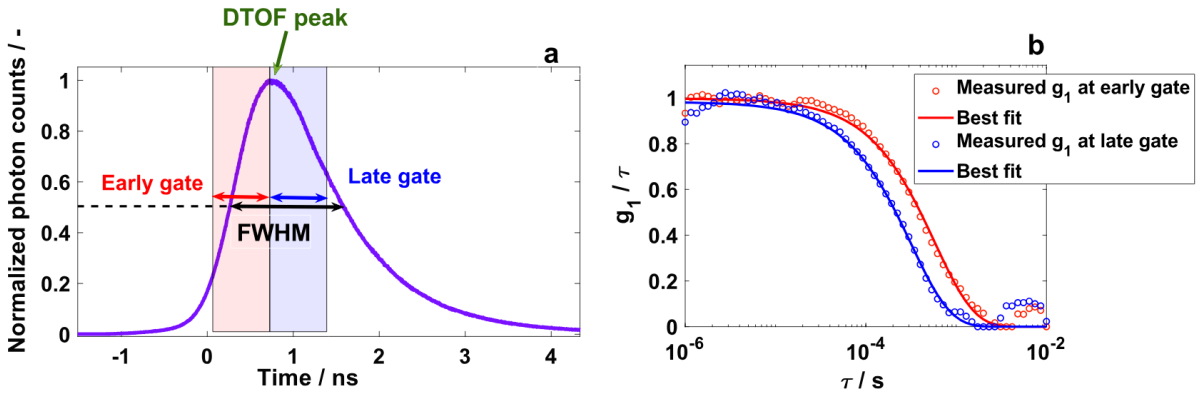


Figure 2.22 a) The defined early and late gates. Early gate starts with the width of FWHM/2 before the DTOF peak on its rising edge and ends at the DTOF peak. The late gate starts at the DTOF peak and ends with the width of FWHM/2 on the falling edge. b) Considering higher αD_b in deeper layer comparing to superficial layer, the signals obtained from photons detected in early gate are expected to be more sensitive to changes in αD_b of scatterers appearing in the superficial layer and the corresponding autocorrelation function decays slower; the signals obtained from photons detected at late gate are expected to be more sensitive to changes in αD_b of scatterers appearing in the deeper layer and the corresponding autocorrelation function decays faster.

Lag Time $(\boldsymbol{\tau})$***:*** For both cw-DCS and td-DCS, the intensity autocorrelation function $g_2(\tau)$ was calculated over a lag time tau range from 10^{-6} to 10^{-2} seconds.

Integration Time: In both cw-DCS and td-DCS, integration time plays a significant role in processing of acquired signals and consequently the estimated αD_b and BFI. The integration time refers to the time ranges of absolute arrival time (t_1 and t_2 in figure 2.20 a) over which the intensity autocorrelation function is computed. The signal to noise ratio can be improved by increasing the integration time which yields losing the temporal resolution required to detect rapid changes in blood flow [19].

To evaluate the td-DCS performance at shorter (1.5 cm) and larger (2 and 2.5 cm) SDSs, the αD_b of phantom and and BFIs of in-vivo measurements were calculated with 2 s integration time. This integration time represents a trade-off between the sufficiently long time to increase the signal to noise ratio and a sufficient temporal resolution to estimate the dynamics of blood flow changes.

The αD_b of the phantom measurements and BFI of simultaneous monitoring of hemodynamic response measured by cw-DCS, td-DCS and BOLD-MRI were calculated with a 2.5 s integration time. This temporal resolution is comparable to the temporal resolution of the BOLD-MRI technique.

In the simultaneous measurements using cw-DCS and IVIM-MRI study, the integration time to estimate the αD_b and BFI measured by cw-DCS was 1 s. Due to the very low temporal

resolution of the IVIM-MRI technique, which provided one dataset almost every two minutes, the cw-DCS flow index with a 1 s integration time was averaged for two minutes of measurements.

Assessment of the DTOFs for time gating: To get the best td-DCS performance at each SDS, the optimal time ranges of DTOF to recover the αD_b of the scatterers contained in superficial and deeper layers of the two-layered phantoms should be founded. To do that, metrics based on the measurands of β and αD_b were determined. The coefficient of variation of β ($CV_{\beta(t)}$) was defined as the ratio of the standard deviation and the mean value of the β, calculated at a given time of flight *t*. The other metrics based on β was the contrast to noise ratio $CNR_{\beta(t)}$ defined as the ratio of the measured $g_2(t,\tau)$ and its standard deviation at short ($\tau \to 0$) and long ($\tau \to \infty$) lag times (e.g. $\tau = 10^{-6}$ s and $\tau = 10^{-2}$ s) [89, 132]:

$$CNR_{\beta}(t,t_s) = \frac{g_2(t,t_s,\tau\to 0) - g_2(t,t_s,\tau\to\infty)}{\sqrt{\sigma^2_{\tau\to 0}+\sigma^2_{\tau\to\infty}}} = \frac{\beta(t,t_s)}{\sqrt{\sigma^2_{\tau\to 0}+\sigma^2_{\tau\to\infty}}}, \qquad (2.14)$$

where $\sigma^2_{\tau\to 0}$ and $\sigma^2_{\tau\to\infty}$ are standard deviation of the $g_2(t,\tau)$ at the short and long lag times (τ) respectively.

Further, the coefficient of variation of the αD_b ($CV_{\alpha D_b}(t)$) at the given time of flight *t* was calculated as the ratio of the standard deviation and the mean value of the αD_b. The equation to evaluate the contrast to noise ratio of the αD_b ($CNR_{\alpha D_b}(t)$) [133] has also been defined as:

$$CNR_{\alpha D_b}(t,t_s) = \frac{\alpha D_b(t,t_s) - \alpha D_b^{slow}(t,t_s)}{\sigma_{\alpha D_b}(t,t_s)}, \qquad (2.15)$$

where $\alpha D_b(t,t_s)$ was measured on two-layered phantom, $\alpha D_b^{slow}(t,t_s)$ is the reference value of the medium with slow $\alpha D_b(t,t_s)$ (phantom mixture with 40% Glycerol) and the $\sigma_{\alpha D_b}(t,t_s)$ is the standard deviation of the $\alpha D_b(t,t_s)$ measured on two-layered phantom at a given time of flight *t*.

Sensitivity metrics (S): To evaluate the performance of td-DCS at shorter (1.5 cm) and larger (2 and 2.5 cm) SDSs in recovering the $\alpha D_b(t,t_s)$ of scatterers contained in superficial and deeper layers, sensitivity metrics were defined similar to [39, 133]. These sensitivities were calculated independently for early and late time gates of the DTOF. Considering two-layered

phantoms with different αD_{b} in superficial and deeper layer, the sensitivity of the td-DCS to recover the changes in displacement of scatterers contained within each layer can be defined as follows:

$$S = \frac{(\alpha D_{\mathrm{b}}(t,t_s)/\alpha D_{\mathrm{b}}^{\mathrm{slow}}(t,t_s))-1}{(\alpha D_{\mathrm{b}}^{\mathrm{fast}}(t,t_s)/\alpha D_{\mathrm{b}}^{\mathrm{slow}}(t,t_s))-1} \cdot 100\% = \frac{\alpha D_{\mathrm{b}}(t,t_s)-\alpha D_{\mathrm{b}}^{\mathrm{slow}}(t,t_s)}{\alpha D_{\mathrm{b}}^{\mathrm{fast}}(t,t_s)-\alpha D_{\mathrm{b}}^{\mathrm{slow}}(t,t_s)} \cdot 100\% \quad (2.16)$$

where t_s is the time of flight, $\alpha D_{\mathrm{b}}(t,t_s)$ was measured on the two-layered phantom, $\alpha D_{\mathrm{b}}^{\mathrm{slow}}(t,t_s)$ and $\alpha D_{\mathrm{b}}^{\mathrm{fast}}(t,t_s)$ are the reference values for the mixtures in which the scatterers move slow (40% Glycerol) and fast (no Glycerol). Therefore, equation 2.16 applied on the data measured on two-layered phantom with higher αD_{b} of scatterers contained in the deep layer was marked as S_{DL} (sensitivity to changes appearing in deeper layer) and for the higher αD_{b} of scatterers within the superficial layer was expressed as S_{SL} (sensitivity to changes appear in in the superficial layer).

Normalized αD_b: To compare the cw-DCS and td-DCS technique ability to assess the αD_{b} of scatterers contained in superficial and deeper layer of the two-layered phantom, the normalized αD_b ($n\alpha D_{\mathrm{b}}$) was calculated from the data measured on two-layered phantom.

$$n\alpha D_b = \frac{\alpha D_{\mathrm{b}} - \alpha D_{\mathrm{b}}^{\mathrm{slow}}}{\alpha D_{\mathrm{b}}^{\mathrm{fast}} - \alpha D_{\mathrm{b}}^{\mathrm{slow}}} \cdot 100\% \quad (2.17)$$

Equation 2.17 is same as equation 2.16, however is suitable to present the analysis of both cw-DCS and td-DCS.

***The beam expander effect*:** A beam expander was used to increase the illumination area to 13 mm in diameter. Therefore, variation of the actual SDSs ranges are 1.5 ± 0.65 cm, 2.0 ± 0.65 cm and 2.5 ± 0.65 cm for three considered SDSs. Using a beam expander in td-DCS may affect measurement of αD_{b}. Parameters including limited laser coherence length, IRF width, gate start time and gate width has influence on $\alpha D_{\mathrm{b}}(t,t_s)$. Thus, the results of measurements of αD_{b} are typically presented in relative scale ($r\alpha D_{\mathrm{b}}$) [35, 118]. In this study, to evaluate the impact of beam expander in td-DCS, the $r\alpha D_{\mathrm{b}}$ as the ratio of the $\alpha D_{\mathrm{b}}^{\mathrm{fast}}(t,t_s)$ to the $\alpha D_{\mathrm{b}}^{\mathrm{slow}}(t,t_s)$ was defined and this value was calculated from the data measured on homogenous phantoms with and without the beam expander on the source fiber's tip.

2.5.3 Blood Oxygenation Level-Dependent MRI

Blood oxygenation level-dependent (BOLD) magnetic resonance imaging (MRI) is a non-invasive imaging technique to monitor the brain hemodynamics response. The BOLD signal can be mathematically modeled by considering the relationship between blood volume and oxygenation changes. A common framework is the balloon model, which describes how changes in blood volume and oxygen metabolism interact to produce the BOLD signal. This model simplifies the complicated network of venous capillaries, venules, and veins into a single compartment that expands and contracts like a balloon based on blood inflow and outflow. The BOLD signal $S_{\mathrm{BOLD}}(T)$ is calculated as a function of venous volume fraction v(T) and deoxygenated hemoglobin content q (T) [134, 135]:

$$S_{\mathrm{BOLD}}\ (T) = V_0.\left(k_1\big(1-q(T)\big) + k_2\left(1-\frac{q(T)}{v(T)}\right) + k_3\big(1-v(T)\big)\right) \qquad (2.18)$$

where $S_{BOLD}(T)$ is the BOLD signal at time T, V_0 is the baseline venous blood volume fraction, $q(T)$ is the relative concentration of deoxygenated hemoglobin, k_1, k_2, k_3 are constants that depend on the magnetic field strength and the properties of the tissue (such as baseline deoxygenation concentration).

The $S_{\mathrm{BOLD}}(T)$ change is based on the magnetic properties of oxyhemoglobin (HBO_2) and deoxyhemoglobin (HB). HBO_2 is diamagnetic, meaning it does not significantly distort the local magnetic field. HB is paramagnetic, meaning it distorts the local magnetic field, leading to changes in the MR signal. $S_{\mathrm{BOLD}}(T)$ changes can be imaged with a spatial resolution on the order of millimeters [50, 136].

In this study, the BOLD-MRI data was preprocessed using MATLAB 2022b and the Statistical Parametric Mapping toolbox (SPM12) [137]. Standard preprocessing steps included slice-timing correction, realignment, and normalization to the Montreal Neurological Institute (MNI) space [138].

Cerebral Metabolic Rate of Oxygen ($CMRO_2$): The $CMRO_2$ refers to the rate of oxygen consumption by the brain and is considered a direct indicator of energy homeostasis and brain health [139]. Estimating $CMRO_2$ has been of great interest in the fields of neuroimaging and neurovascular coupling. Many studies have estimated this parameter using simultaneous monitoring of hemodynamics response measured by BOLD-MRI and near-infrared

spectroscopy techniques [140, 141]. $CMRO_2$ can be defined as the product of the CBF and BOLD signal changes. In this study the relative $CMRO_2$ ($rCMRO_2$) change has been derived from the model proposed by Davis and Hoge [142, 143]:

$$rCMRO_2 = \left(\frac{CBF}{CBF_0}\right)^{1-\alpha/\beta} \left(1 - \frac{\frac{\Delta BOLD}{BOLD_0} - 1}{M}\right)^{1/\beta} \tag{2.19}$$

where CBF_0 and CBF are the values observed during baseline and during the respiratory challenges. $\Delta BOLD$ is the S_{BOLD} change, $BOLD_0$ is the S_{BOLD} observed during baseline, M is the BOLD calibration constant and $\alpha \approx 0.38$ and $\beta \approx 1.5$ are the constant parameters [144, 145]. To estimate the M, equation 2.19 can be rewritten as follows [143]:

$$\frac{\Delta BOLD}{BOLD_0} = M \left(1 - (rCMRO_2)^{\beta} \left(\frac{CBF}{CBF_0}\right)^{\alpha-\beta}\right) \tag{2.20}$$

During breath hold respiratory challenge, it is assumed that $CBF > CBF_0$. Considering the $\alpha - \beta$ gives a negative value, the $\left(\frac{CBF}{CBF_0}\right)^{\alpha-\beta}$ would dominate any changes in $CMRO_2$, thus reduces the entire term in parentheses in equation 2.20 to unity. Consequently, M can be estimated as the maximum BOLD signal change during the breath hold for each individual subject [146, 147].

Region of interest of BOLD-MRI image: Parametric Bayesian segmentation was applied to anatomical images to generate individual tissue masks for each subject. Three masks of scalp, skull, and gray matter were used to extract the BOLD signals changes. The scalp and skull were classified as the extracerebral layer of tissues, while the gray matter represented the intracerebral tissue layer.

In this study, from the data obtained across 14 volunteers, the average thickness of the extracerebral layer (from scalp surface to gray matter) estimated from MRI images, was 12 mm; while the average gray matter thickness was approximately 3 mm. Although there is cerebrospinal fluid between the skull and gray matter, it was not considered in the two-layer head model due to its negligible optical scattering and absorption properties, which minimally impacts the detected optical signal and hence the estimated BFI [47, 148].

To improve the signal-to-noise ratio, BOLD signals were extracted from tissue regions with segmentation probability greater than 70%. Segmentation probability refers to the probability (0–100%) that a given voxel belongs to a specific tissue [149].

2.5.4 Intravoxel Incoherent Motion MRI

IVIM-MRI is a contrast-agent-free diffusion-weighted imaging technique that enables the visualization and quantification of microscopic motion of water molecules within biological tissues. IVIM-MRI distinguishes between two types of motions: water molecules diffusion and microvascular perfusion related to blood flowing in the capillary network [150, 151].

In DWI technique, the magnetic gradients are used for sensitizing the motion of water molecules which results in MR signal attenuation. If the MR signal *S* is measured in a liquid solution with only the Brownian motion of water molecules [152], the signal attenuation can be expressed by a single exponential equation [103]:

$$\frac{S}{S_0} = e^{-bD_B} \qquad (2.21)$$

where S represents the attenuated MR signal, S_0 is the MR signal at baseline with no diffusion gradients $(b = 0)$ and D_B is Brownian diffusion coefficient. *b*-value refers to the weighting of the diffusion of the MR pulse sequence and is determined by the magnitude and timing (duration and separation) of the diffusion gradients. The b-value is the factor that defines the degree of diffusion weighting in an MR sequence. It quantifies how sensitive the sequence is to the microscopic random motion (Brownian motion) of water molecules [103].

In biological tissues the water molecules diffusion in the extravascular tissue and the blood microcirculation within the intravascular tissue, lead to MR signal attenuation. Therefore, the signal attenuation can be described by a two-exponential IVIM-MRI model that incorporates the contributions from both blood perfusion (fast component) and water molecules diffusion (slow component) [103, 104].

$$S = S_0\,(fe^{-bD_{\text{fast}}} + (1-f)e^{-bD_{\text{slow}}}) \qquad (2.22)$$

where S_0 represents the MR signal at baseline. f is the IVIM-derived perfusion fraction, which quantifies the fractional contribution of MR signal attenuation due to intravascular blood perfusion to the overall MR signal attenuation. f distinguishes the intravascular perfusion and water molecules diffusion motion within the extravascular tissue [150, 153]. D_{fast} is the IVIM-derived Pseudo-diffusion coefficient which quantifies the perfusion-related motion of blood

within the microvascular network referring to blood perfusion. This parameter is called pseudo-diffusion coefficient as it represents the motion of water molecules caused by microcirculation of blood (perfusion) in the capillaries, rather than water Brownian diffusion motion. D_{fast}, in muscle tissue is approximately on the order of $\approx 10^{-2}\ \text{mm}^2/\text{s}$. D_{slow} is the IVIM-derived diffusion coefficient, which reflects the Brownian-related motion of water molecules in extravascular tissue with the order of magnitude $\approx 10^{-3}\ \text{mm}^2/\text{s}$ [103, 150]. Due to the origin of the latest two parameters, the D_{fast} is generally at least an order of magnitude greater than D_{slow} [104, 150]. Considering the classical tissue perfusion parameters, the f is proportional to blood volume contained in the tissue. D_{fast} is proportional to the blood velocity in tissue. $f \cdot D_{\text{fast}}$ is proportional to blood flow in the tissue [104, 154]. In this study $f \cdot D_{\text{fast}}$ reflects the IVIM-derived flow (F_{IVIM}) in the tube of the tissue mimicking phantom and IVIM-derived blood flow (BF_{IVIM}) of the volunteer's muscle during occlusion test.

The IVIM-derived parameters were calculated using software developed by Kamil Lipinski [102, 155], implemented in MATLAB 2022b (MathWorks, Natick, MA, USA). The diffusion data underwent a preprocessing procedure involving the following four steps: denoising, removal of Gibbs ringing artifacts, eddy current correction, and DWI bias field correction. Denoising was performed using the Marchenko–Pastur Principal Component Analysis [156, 157]. The Gibbs ringing artifacts were mitigated through the method of local subvoxel-shifts [158] and were performed using MRTrix version 3.0.4 [159]. The eddy current correction was corrected using FSL software version 6.0.6.4 [160]. The B1 Inhomogeneity correction was applied using the N4 algorithm [161] implemented in the ANTs software version 2.3.1 [162].

To enhance the robustness and stability of the estimations, a segmented fitting approach was employed [102]. In first step, to estimate D_{slow}, the attenuated MR signal at the high b-value in the range of $b > 250\ \text{s/mm}^2$ was fitted using single-exponential model (Equation 2.21). Because in $b > 250\ \text{s/mm}^2$ range, the contribution of perfusion-related motion in microcapillary network is negligible and the decay of signal is dominated by Brownian motion of water molecules in tissue. In the second step, the attenuated MR signal at $b = 0$ was subtracted from the attenuated MR signal attenuation at $b > 250\ \text{s/mm}^2$. Then, this subtraction was divided to the attenuated MR signal at $b = 0$ to estimate the *f*. In the third step, considering the values of D_{slow} and f calculated in last two steps, the pseudo-diffusion coefficient D_{fast} was obtained. To do that the attenuated MR signal acquired at b-values in the range of $0 < b < 1500\ \text{s/mm}^2$, was fitted using the two-exponential IVIM model (Equation 2.22). This is because, the signal obtained in this range of low b-value ($0 < b < 1500\ \text{s/mm}^2$)

is sensitive to diffusion-related motion of water molecules in extravascular structure of tissue ($b > 250\ \mathrm{s/mm^2}$) and perfusion-related motion in microcapillary network ($b < 250\ \mathrm{s/mm^2}$) [163, 164].

Region of interest of DWI image: For the phantom experiment, the IVIM-derived parameters were calculated from the regions restricted to voxels in which the tubes were positioned. To exclude voxels that partially covered tubing from the primary analysis, after performing IVIM parameters reconstruction, the region of interest (ROI) was subjected to the voxels with $f > 0.1$.

For the leg and forearm muscle occlusion tests, data from a rectangular cuboid region of interest with $6 \times 4 \times 2$ cm (length×width×depth) was analyzed. The cuboid was positioned with the largest dimension along the muscle. This ROI was chosen to target the specific muscles (gastrocnemius muscle in the leg and the extensor muscle in the forearm), while considering the expected photon path distribution in tissue for SDS of 2 cm and sufficiently large ROI to improve the IVIM signal to noise ratio. To ensure reliable IVIM-derived parameter estimation, a signal intensity threshold in the MR data processing was applied to restrict the analysis to voxels within the range of $S \leq 0.95\ S_{\max}$, where S is the MR signal attenuation calculated using Equation 2.22. This was done to focus the analysis on microvascular perfusion rather than large-vessel arterial and venous flow. This limit ensures that the resulting maps represent microvascular perfusion (capillary network perfusion) rather than components related changes of blood flow in large-vessels [165].

Each of the IVIM-derived parameters measured on tissue mimicking phantom and muscle occlusion test was calculated from the entire ROI. This calculation aligns well with the estimated αD_{b} and BFI. Because of multiple sequential photon scattering events on the path between source and detector the spatial resolution of the DCS technique is low. Similarly, the measured signal is influenced by αD_{b} changes of scatterers occurring on the path of photons between the source and detection points [166].

2.5.5 Cross-analysis of the signals obtained by DCS, BOLD-MRI and IVIM-MRI

Statistical analysis: The Wilcoxon signed-rank test was performed using two-sided p-values. This test was used to evaluate the statistically significant changes in amplitude of αD_{b}, BFI, BOLD, and IVIM signals. The Wilcoxon signed rank test is a nonparametric test for

independent paired data [167]. This test is appropriate for data analyses within-sample or within-subject changes. The homogenous and two-layered phantom measurements were performed using the mixtures prepared with the same ingredients; however, prepared in such a way that different αD_b were obtained. The tissue mimicking phantom carried out with the same phantom, while the αD_b in the tubes changed using syringe pump. The in vivo tests were performed by volunteers, while the BFI changed using occlusion test or respiratory challenges. These conditions fulfil the requirement for intrinsically paired data to use Wilcoxon signed rank test. A p-value lower than 0.05 ($p < 0.05$) was considered statistically significant.

***Comparison of temporal hemodynamic responses measured by DCS and BOLD-MRI by analysis of hysteresis loop*:** To assess the temporal hemodynamic response captured independently by DCS and BOLD-MRI, the BFI signal changes and BOLD signal changes derived for both intracerebral and extracerebral layers of tissues were normalized to unity. Subsequently, a hysteresis loop was plotted, illustrating the relationship between the normalized BFI and BOLD signal over time. The loop not only reflects how the two signals evolve together but also reveals their temporal alignment of the signals [168].

Histograms of the hemodynamic response delays measured by DCS and BOLD-MRI: In order to find the delay between the BFIs and BOLD signals, in response to the performed BH and HV respiratory challenges, the signals were smoothed using a moving average filter with a window size of 5 samples (smoothdata (data,"movmedian",5) in MATLAB) to reduce the noise. Then the signals were synchronized at the positions of the maximum and minimum of the signal amplitude. The delays of responses observed in the BFIs and BOLD signals were determined as the time shift of signals before the synchronization.

Correlation of Hemodynamic Responses measured by DCS and BOLD-MRI: To assess the relationship between BFI and BOLD signal changes, a linear regression analysis was performed to compute the Pearson correlation coefficient (r) between the synchronized signals. The Pearson correlation coefficient was chosen since it was expected that there is a linear relationship between the BFI and BOLD signals changes [43]. Moreover, calculating the correlation from the synchronized signals enhances the comparison accuracy and leads to a stronger observed correlation between BFI and BOLD dynamics. This strategy has also been applied in other studies [169-171].

***Correlation between the IVIM-derived parameters and flow index measured by cw-DCS*:** To evaluate the correlation between the IVIM-derived parameters and DCS-derived flow index

measured on tissue mimicking phantom, Pearson's correlation (r) approach was considered. The Pearson correlation coefficient was chosen since a direct linear relationship was expected between the IVIM-derived parameter and BFI [53]. The r varies from -1 to 1 and measures the extent to which a linear model explains variability in the data.

3 Results

3.1 Comparison of td-DCS performance at shorter and larger SDSs

In this part, the td-DCS performance at shorter (1.5 cm) and larger (2 and 2.5 cm) SDSs for recovering the αD_b and BFI were presented. Using quality metrics such as coefficient of variation and contrast-to-noise ratios, the optimal time gate(s) of the DTOF to extract the αD_b of scatterers were identified. The sensitivity metrics of the td-DCS at shorter (1.5 cm) and larger (2 and 2.5 cm) SDSs were evaluated on two-layer phantoms with different αD_b and superficial layers thicknesses. These sensitivity metrics helps to evaluate the sensitivity of each SDSs in related early and late time gates to recover the αD_b of superficial and deeper layer of two-layered phantom. Finally, in vivo experiments were carried out on the forearm and forehead of healthy volunteers to compare each SDS's ability to recover the BFI changes of muscles in response to the occlusion test and cerebral layer during respiratory challenges.

Physical phantom: In order to find the optimal DTOF range to estimate the αD_b and BFI, a series of measurements were performed on homogenous and two-layered phantoms (detailed in 2.4.1 Physical phantom – homogeneous and two-layered phantoms). The β and αD_b parameters have been calculated for the time ranges around DTOF peak, measured on homogeneous phantoms at shorter (1.5 cm) and larger (2 and 2.5 cm) SDSs. Here 5% of IRF was considered as zero time to compare the time shift of the measured DTOFs by increasing the SDSs.

As shown in Figure 3.1, increasing the SDS shifts the DTOFs to a longer time of flight and broadens the DTOF profile. Therefore, based on the proposed time-gating strategy in this study (Detailed in 2.5.2 DCS techniques - Time gating strategy in td-DCS), shift and broadening of the DTOF by increasing the SDS, affects the position of the early and late gates. According to Figure 3.2, the standard deviation of the calculated β and αD_b of longer time of flight at larger SDSs of 2 and 2.5 cm is lower compared to shorter SDS of 1.5 cm. Moreover td-DCS at larger SDSs allows to use high laser power without FIFO overflow (detailed in 2.3.1 Optical data acquisition - Experimental setup of the td-DCS at different source detector separation).

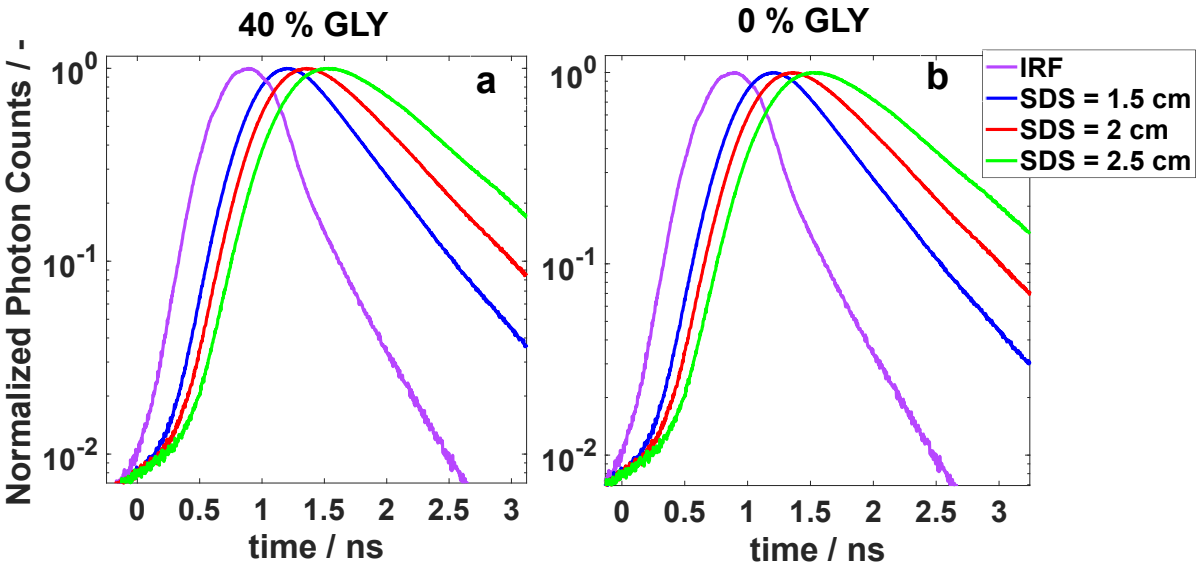


Figure 3.1 The IRF as well as the DTOFs measured on homogenous phantoms with a) 40% Glycerol concentration and b) no Glycerol. Time zero refers to 5% of the IRF on rising edge. The figure was adapted from N. Mogharari et al. [39].

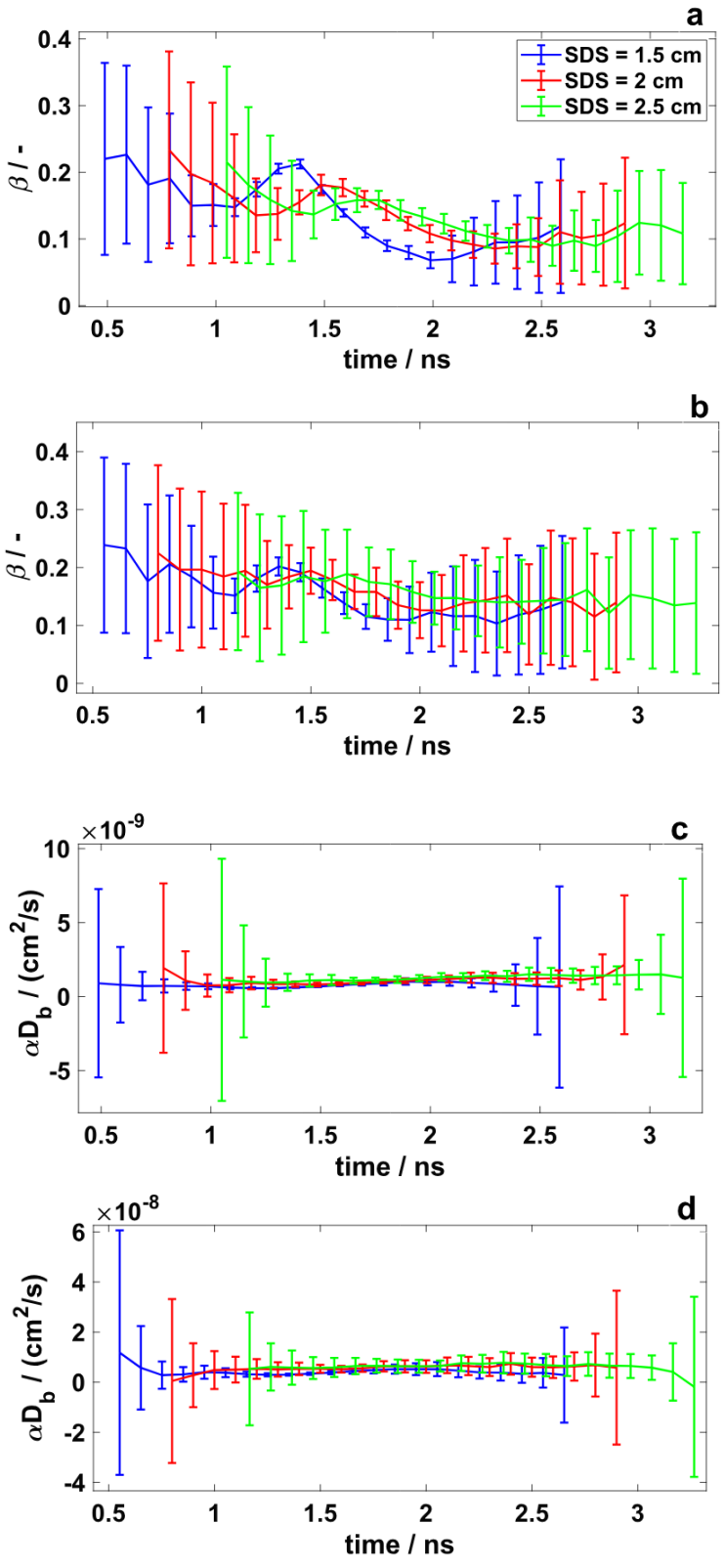


Figure 3.2 a) Estimated $\beta(t, t_s)$ and c) $\alpha D_b(t, t_s)$ as a function of time of flight for homogeneous phantoms containing 40% glycerol, b) Estimated $\beta(t, t_s)$ and d) $\alpha D_b(t, t_s)$ as a function of time of flight for homogeneous phantoms containing 0% glycerol, measured at source-detector separations of 1.5, 2.0, and 2.5 cm. Error bars represent the standard deviation. Time zero was defined as the time point corresponding to 5% of the IRF maximum on the rising edge of the DTOF.

To define the optimal DTOF range to recover the $\alpha D_b(t, t_s)$ and BFI, the measurand $\beta(t, t_s)$ and related metrics including coefficient of variation $(CV_\beta((t, t_s)))$ and contrast to noise ratio $(CNR_\beta((t, t_s)))$ (figure 3.3, 3.4, and 3.5) were calculated (based on analyses detailed in 2.5.2 DCS techniques - Assessment of the DTOFs for time gating). These parameters have been calculated for the time range of 2.2 ns around DTOFs peak, measured on homogenous and two-layered phantoms (detail explained in 2.4.1 physical phantom-homogenous and two-layered phantom). The ~2 ns time range around DTOF peak was proposed based on figures 3.2 as it has the lowest standard deviation in the estimation of the $\beta(t, t_s)$ and $\alpha D_\mathrm{b}(t, t_s)$. The $\beta(t, t_s)$ and related metrics have been calculated for every 100 ps of DTOF and indicates different trends over various times of flight. The highlighted red and blue area refers to early and late gates calculated by the proposed gating strategy (calculation based on data analyses detailed in section 2.5.2 DCS techniques-Time gating strategy in td-DCS). In this gating approach, zero time refers to DTOF peak.

As shown in figure 3.3, the $\beta(t, t_s)$ decreases at longer time of flight. The high $CV_\beta((t, t_s))$ in early and late time ranges follows the high standard deviation in $\beta(t, t_s)$. The $CNR_\beta(t, t_s)$ depends on the ratio of $\beta(t, t_s)$ and noise of the measured $g_2(t, \tau)$ and follows other metrics' trends. According to these results, the time ranges with the highest $\beta(t, t_s)$ and $CNR_\beta(t, t_s)$ and the lowest $CV_\beta(t, t_s)$ are the optimal DTOF range to extract $\alpha D_\mathrm{b}(t, t_s)$ and BFI which refers to DTOF peak. So, the red and blue highlighted area referring to early and late gates calculated by the proposed gating strategy (calculation based on data analyses detailed in section 2.5.2 DCS techniques-Time gating strategy in td-DCS) matches well with the optimal time ranges based on these measurand and metrics.

Comparing the results from different SDSs indicate an increase in SDS leads to decrease in $\beta(t, t_s)$, consequently increases the $CV_\beta(t, t_s)$ and decreases the $CNR_\beta(t, t_s)$.

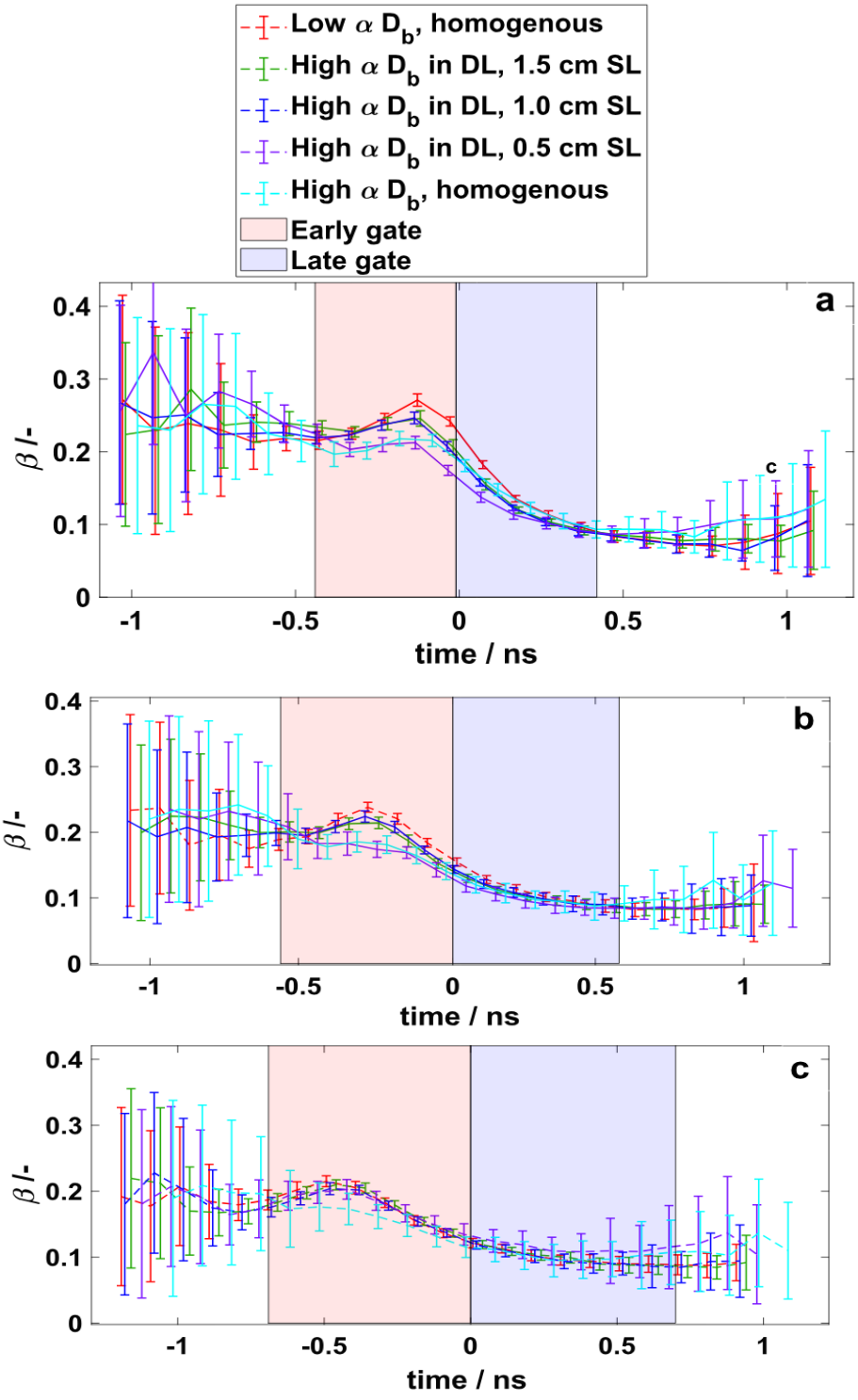


Figure 3.3, $\beta(t, t_s)$ at different time of flight of photons (t_s) and SDSs of a) 1.5cm, b) 2cm and c) 2.5cm. Time 0 is set at the maximum value of the DTOF. Each data points have been calculated within windows of 100 ps from 120 $g_2(t, \tau)$ collected with 2 s integration time. The rectangular red and blue areas refer to the early and late gates, respectively. DL – deep layer, SL – superficial layer. The figure was adapted from N. Mogharari et al. [39].

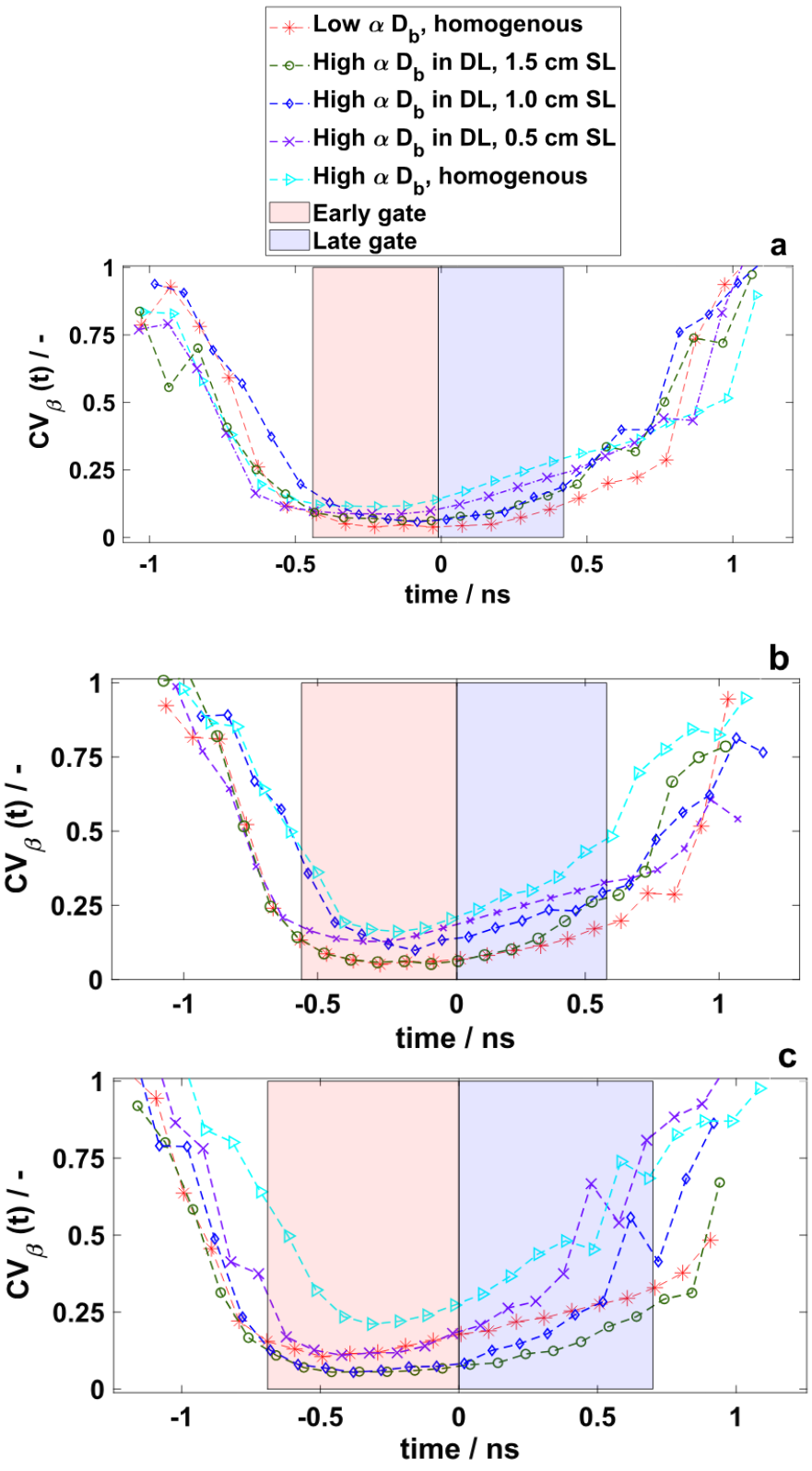


Figure 3.4 The calculated coefficient of variation $CV_\beta(t, t_s)$ metrics at different time of flight of photons (t, t_s) and SDSs of a) 1.5 cm, b) 2cm and c) 2.5cm. Each data points have been calculated within windows of 100 ps from 120 g_2 (t,τ) collected with 2 s integration time. The rectangular red and blue areas refer to the early and late gates. The time 0 refers to the DTOF peak. DL – deep layer, SL – superficial layer. The figure was adapted from N. Mogharari et al. [39].

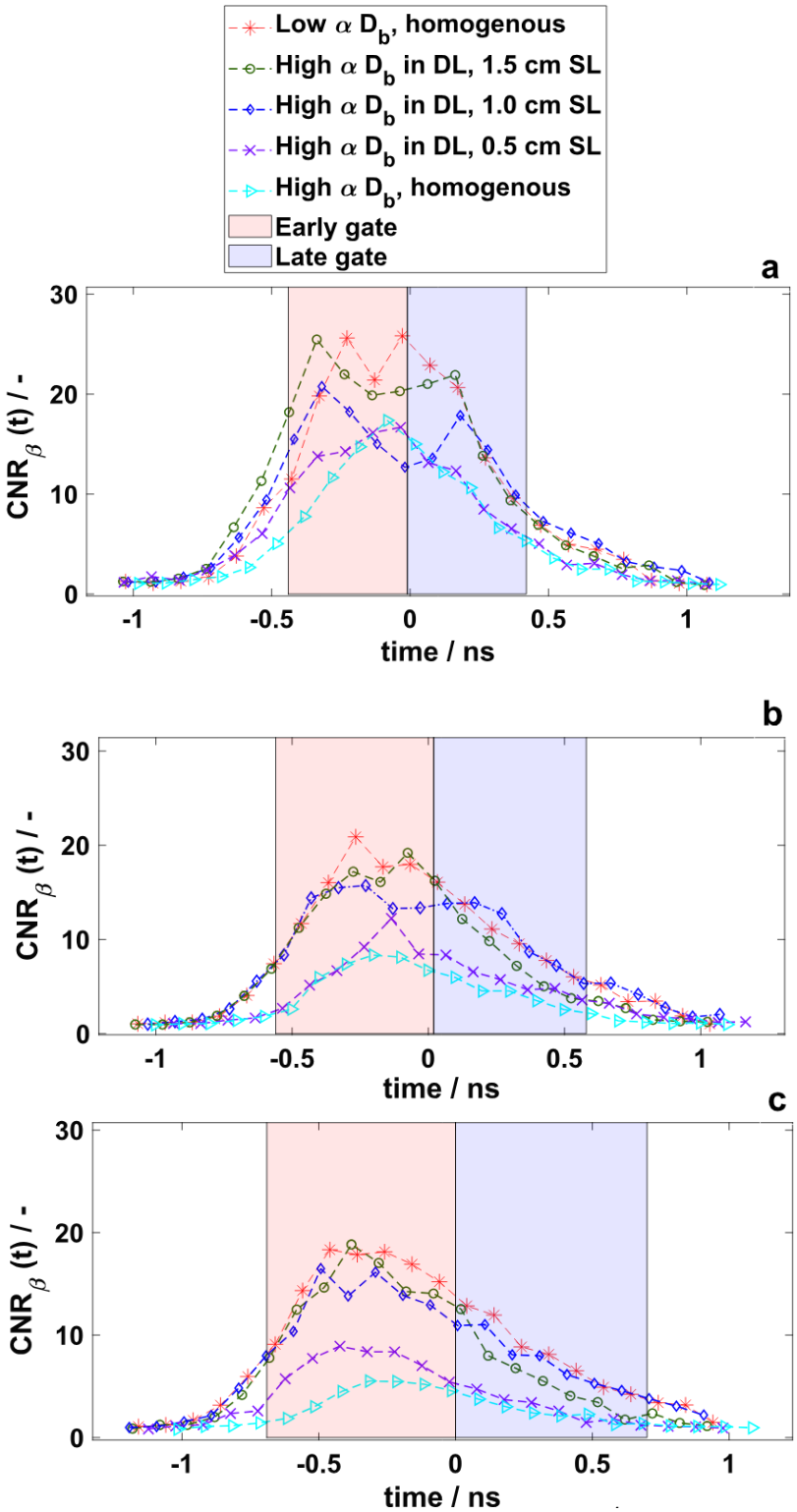


Figure 3.5 The calculated contrast to noise ratio $\mathrm{CNR}_\beta(t, t_s)$ metrics at different time of flight of photons (t, t_s) and SDSs of a) 1.5, b) 2 and c) 2.5 cm. Each data points have been calculated within windows of 100 ps from 120 $g_2(t, \tau)$ collected with 2 s integration time. The rectangular red and blue areas refer to the early and late gates. The time 0 refers to the DTOF peak. DL – deep layer, SL – superficial layer. The figure was adapted from N. Mogharari et al. [39].

Figure 3.6, 3.7 and 3.8 show the calculated $\alpha D_{\mathrm{b}}(t, t_s)$ and related metrics including coefficient of variation ($CV_{\alpha \mathrm{D_b}}(t, t_s)$) and contrast to noise ratio ($CNR_{\alpha \mathrm{D_b}}(t, t_s)$) (calculation based on data analyses detailed in 2.5.2 DCS techniques - Assessment of the DTOFs for time gating). The measurand of $\alpha D_{\mathrm{b}}(t, t_s)$ shown in figure 3.6 (a) has been extracted for the corresponding β shown in figure 3.3 (a). The retrieved $\alpha D_{\mathrm{b}}(t, t_s)$ of two-layered phantoms, changes in the range of the αD_{b} of the homogeneous phantoms mixtures which were used to fill the superficial and deep layer (phantoms feature detailed in 2.4.1 physical phantom-homogenous and two-layered phantom). As the $\alpha D_{\mathrm{b}}(t, t_s)$ refers to the mean squared displacements of scatterers per time, it is expected to be constant in the homogenous medium. However, the limited coherence of the pulsed laser leads to slightly differences in the mean value of aD_{b} along the DTOF.

Based on these results, lower standard deviation in the $aD_{\mathrm{b}}\,(t, t_s)$ calculated from the photons detected at time ranges around DTOF peak indicate lower $CV_{\alpha \mathrm{D_b}}(t, t_s)$ and significantly higher $CNR_{\alpha \mathrm{D_b}}(t, t_s)$. The $CNR_{\alpha \mathrm{D_b}}(t, t_s)$ for the detected photons with very short and very long time of flights is close to zero.

According to the measurand of $\alpha D_{\mathrm{b}}(t, t_s)$ and related metrics, the optimal range of DTOF with lowest standard deviation and best recovered metrics is around DTOF peak. The estimated early and late time gates with the proposed gating approach (calculation based on data analyses detailed in section 2.5.2 DCS techniques-Time gating strategy in td-DCS) follows well the optimal DTOF ranges based on the measurands of $\alpha D_{\mathrm{b}}(t, t_s)$ and related metrics.

As mentioned before, increasing the SDS leads to shift the DTOF peak to later time of flight and increases the possibility of detecting photons with longer pathlength which come from deeper layer. So, although lower $\beta(t, t_s)$ at larger SDS increases the standard deviation in the calculated $\alpha D_{\mathrm{b}}(t, t_s)$; higher number of photons with longer TOF detected from deeper layer increase the $CNR_{\alpha \mathrm{D_b}}(t, t_s)$. This is due to the higher differences between the recovered $\alpha D_{\mathrm{b}}(t, t_s)$ measured on two-layered phantom and $\alpha D_{\mathrm{b}}^{\mathrm{slow}}(t, t_s)$ in superficial layer, which leads to comparable $CNR_{\alpha \mathrm{D_b}}(t, t_s)$ between shorter (1.5 cm) and larger (2 and 2.5 cm) SDSs (see figure 3.8).

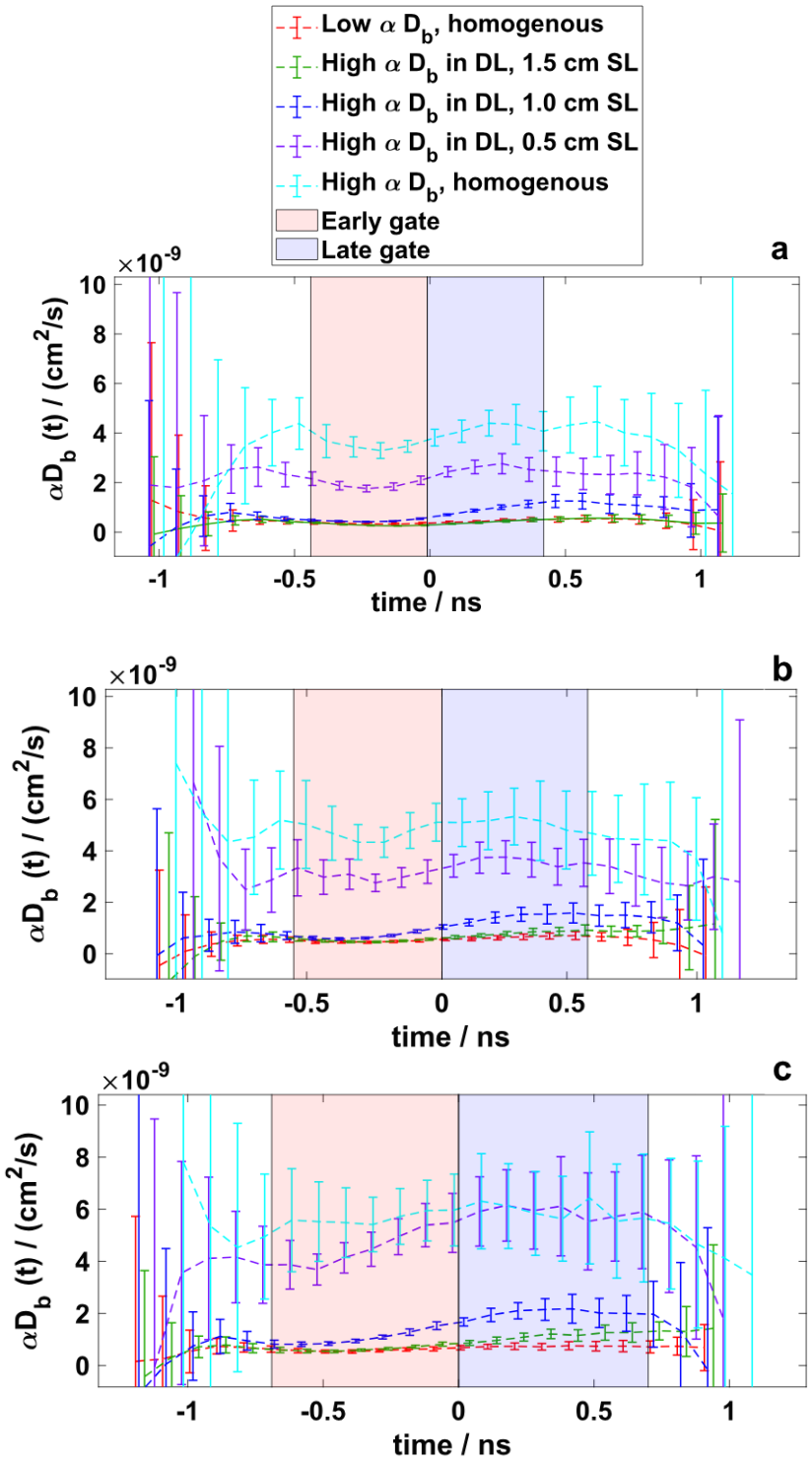


Figure 3.6 The recovered $\alpha D_b(t, t_s)$ parameter as a function of time of flight of photons for different SDSs of a) 1.5, b) 2 and c) 2.5 cm. Time 0 is set at the maximum of the DTOF. Each data points have been calculated within windows of 100 ps from 120 autocorrelation functions $g_2(t, t_s, \tau)$, collected with 2 s integration time each. The red and blue shaded areas refer to the early and late gates, respectively. DL – deep layer, SL – superficial layer. The figure was adapted from N. Mogharari et al. *[39]*.

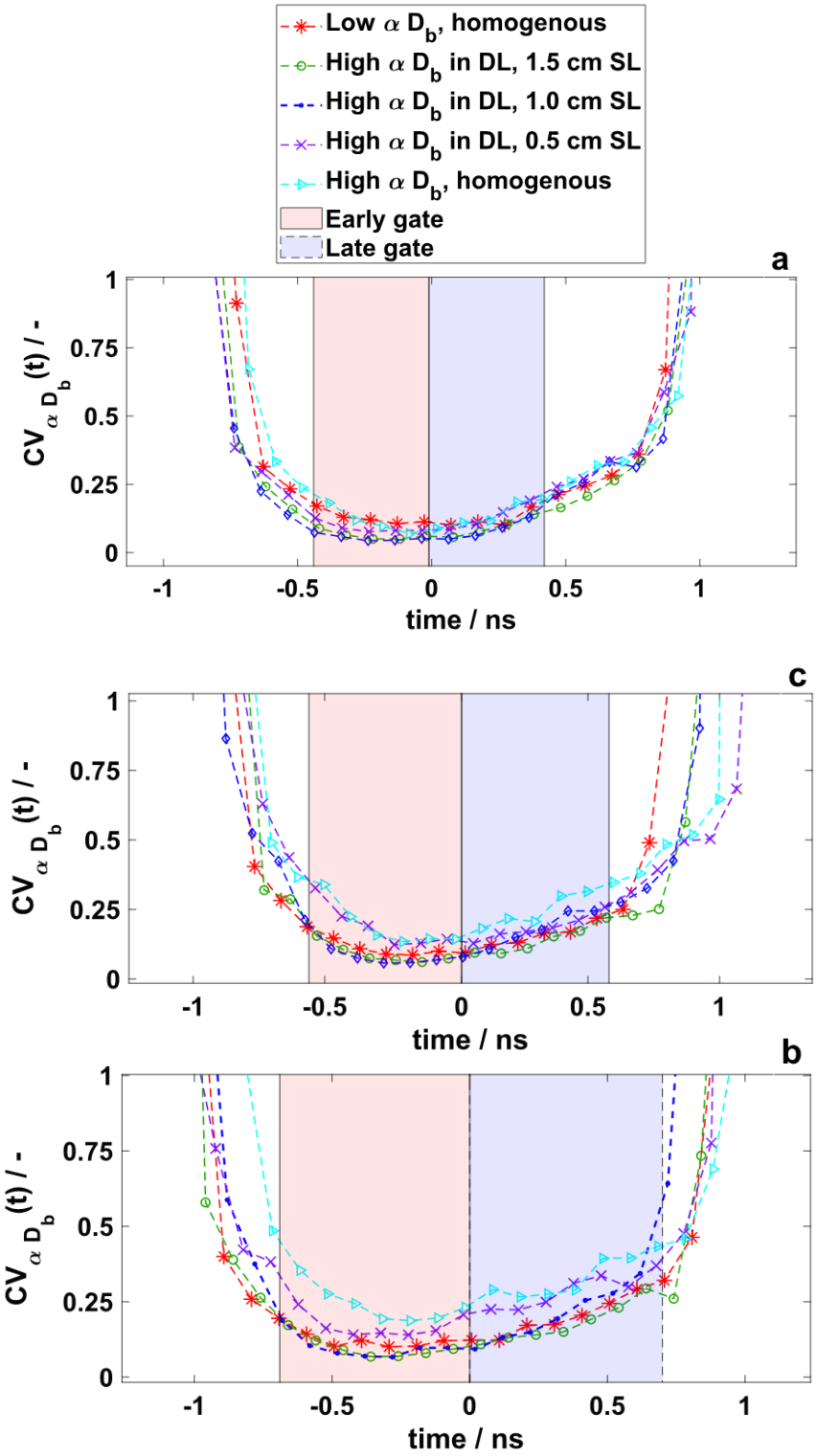


Figure 3.7 The recovered coefficient of variation $CV_{\alpha D_b}(t, t_s)$quality metric at varying time of flight of photons and SDS of a) 1.5, b) 2 and c) 2.5 cm. Time zero is set at the maximum of the DTOF. Data point calculated within windows of 100 ps from 120 autocorrelation functions $g_2(t, t_s, \tau)$, collected with 2 s integration time each. The red and blue shaded areas refer to the early and late gates, respectively. The time zero refers to the DTOF peak. DL – deep layer, SL – superficial layer. The figure was adapted from N. Mogharari et al. [39].

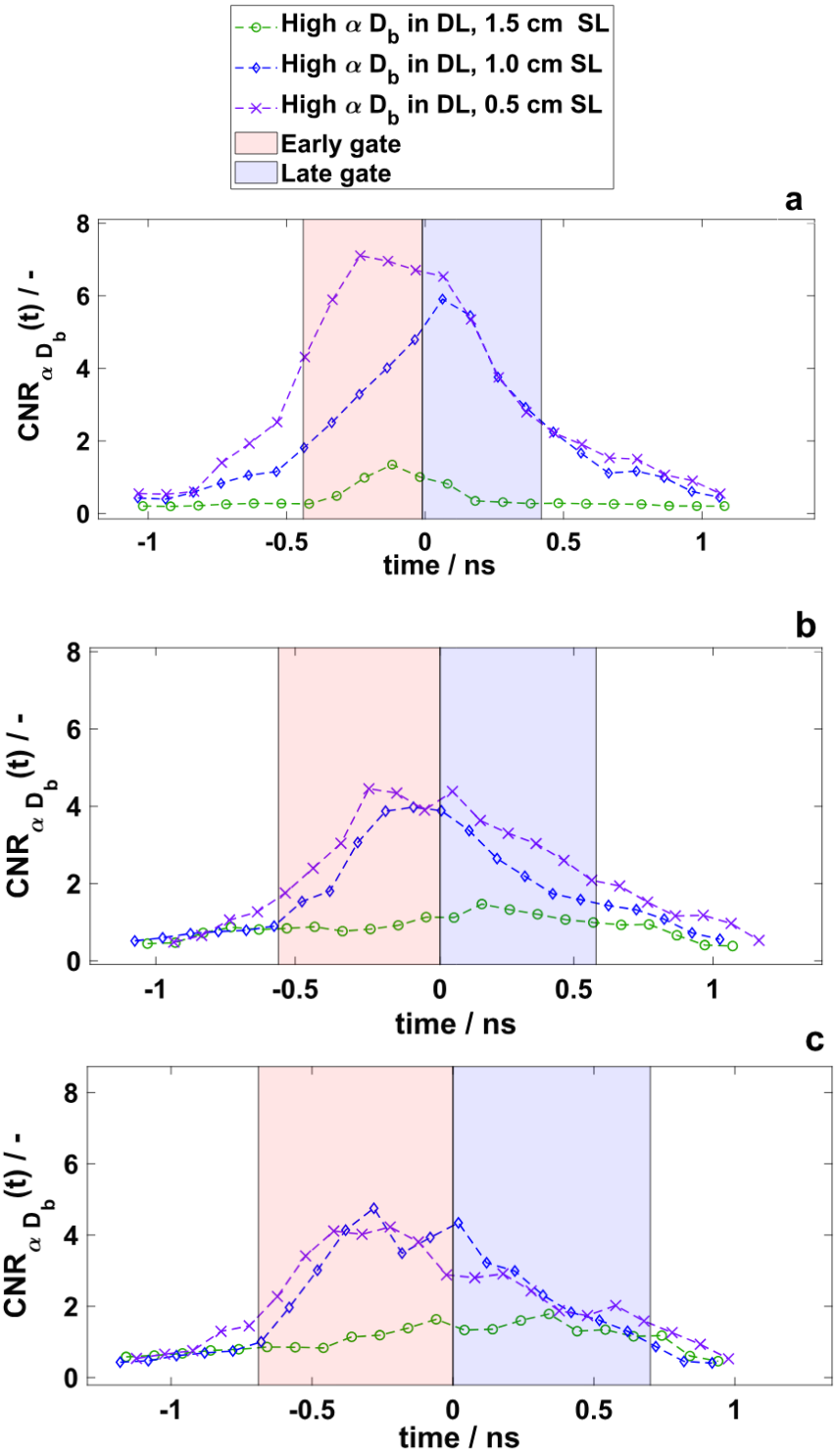


Figure 3.8 The recovered contrast to noise ratio $CNR_{\alpha D_b}(t, t_s)$ quality metric at varying time of flight of photons and SDS of 1.5 (a), 2 (b) and 2.5 (c) cm. Time 0 is set at the maximum of the DTOF. Data point calculated within windows of 100 ps from 120 autocorrelation functions $g_2(t, t_s, \tau)$ collected with 2 s integration time each. The rectangular red and blue areas refer to the early and late gates. The zero time refers to the DTOF peak. DL – deep layer, SL – superficial layer. The figure was adapted from N. Mogharari et al. [39].

To evaluate the impact of beam expander on monitoring the $\alpha D_{\mathrm{b}}(t, t_s)$ of scatterers, the experiments were repeated without the beam expander at tip of laser's fiber, measured on homogenous phantoms with 40% glycerol concentration ($\mathrm{D_b^{slow}}(t, t_s)$) and 0% glycerol concentration ($\mathrm{D_b^{fast}}(t, t_s)$). Then, these results were compared with the data measured using beam expander. Figure 3.9 shows the relative $\alpha D_{\mathrm{b}}\ (t, t_s)$ ($r\alpha D_{\mathrm{b}}\ (t, t_s)$) as the ratio of $\mathrm{D_b^{fast}}(t, t_s)$ to the $\mathrm{D_b^{slow}}(t, t_s)$ (calculation based on data analyses detailed in section 2.5.2 DCS techniques - The beam expander effect), calculated for detected photons from the early and late time gates measured at different SDSs. Based on these results, there is no statistically significant difference ($p > 0.05$) between the $r\alpha D_{\mathrm{b}}\ (t, t_s)$ calculated from the early and late gates measured with and without beam expander.

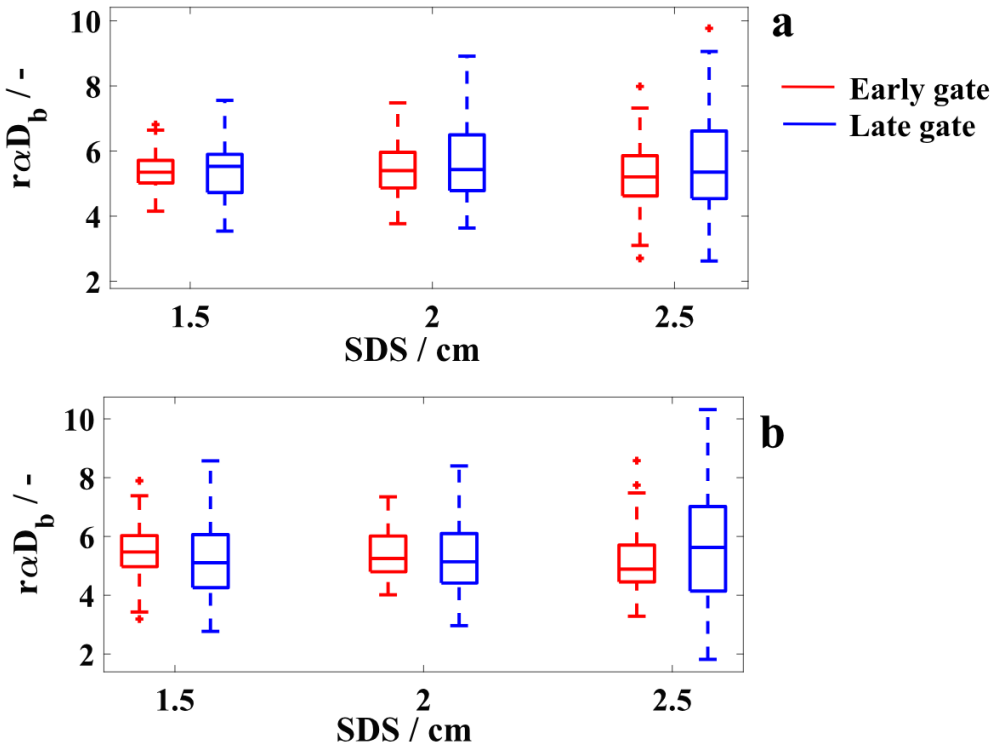


Figure 3.9 The $r\alpha D_b = \alpha D_b^{\mathrm{fast}}((t, t_s))/\alpha D_b^{\mathrm{slow}}((t, t_s))$ measured a) without the beam expander and b) with the beam expander at tip of detection fiber. The boxplots were calculated from the data acquired within early and late gates from 120 autocorrelation functions $g_2(t, t_s, \tau)$ collected with 2 s integration time each. In each boxplot, the central line represents the median, the lower and upper edges indicate the 25th and 75th percentiles, respectively. Whiskers extend to the most extreme data points, not considering outliers. Outliers are indicated by plus signs. The figure was adapted from N. Mogharari et al. [39].

As in td-DCS, early and late gates are expected to carry information of the displacements of scatterers in the superficial and deeper layers, the sensitivities of each SDS at defined time gates to recover the αD_b in deep layer ($S_{DL}(t, t_s)$) have been evaluated (calculation based on data analyses detailed in 2.5.2 DCS technique - sensitivity metrics). Figure 3.10 shows the $S_{DL}(t, t_s)$ calculated for two-layered phantom with different top layer thickness, where the $\alpha D_b(t, t_s)$ of scatterers in the deeper layer is more than in the superficial layer. For all phantoms with different superficial layer thicknesses, SDSs of 2 and 2.5 cm improve the sensitivity to recover the αD_b in deeper layer when using the late gate. However, increased SDS also affects the position of the early gate and consequently increases its sensitivity to displacements of satterers in deeper layer, which is especially observed for the phantom with a low superficial layer thickness (0.5 cm).

For phantoms with high superficial layer thicknesses of 1 and 1.5 cm, the difference between the $S_{DL}(t, t_s)$ of the early and late gates is clearly visible (figure 3.10 a, b). As shown in figure 3.10 (a), which is the closest approximation to an adults' human head model [106, 107], the $S_{DL}(t, t_s)$ of late gate to $\alpha D_b(t, t_s)$ of scatterers in a deep layer (brain) located 1.5 cm from the surface can be increased by an average of 2.4 times while changing the SDS from 1.5 cm to 2.5 cm.

Sensitivity of td-DCS to displacements of scatterers in superficial layer ($S_{SL}(t, t_s)$) (calculation based on data analyses detailed in 2.5.2 DCS technique - sensitivity metrics) is another important parameter calculated from the two-layered phantom with higher $D_b(t, t_s)$ in the superficial layer. As shown in figure 3.11 (a), in the case of very thick top layer thickness (1.5 cm) both early and late gates at all SDSs show high $S_{SL}(t, t_s)$ and strongly affected by $\alpha D_b(t, t_s)$ of scatterers in superficial layer. However, $S_{SL}(t, t_s)$ decreases for phantoms with lower top layer thickness, specially at larger SDSs (figure 3.11 b, c).

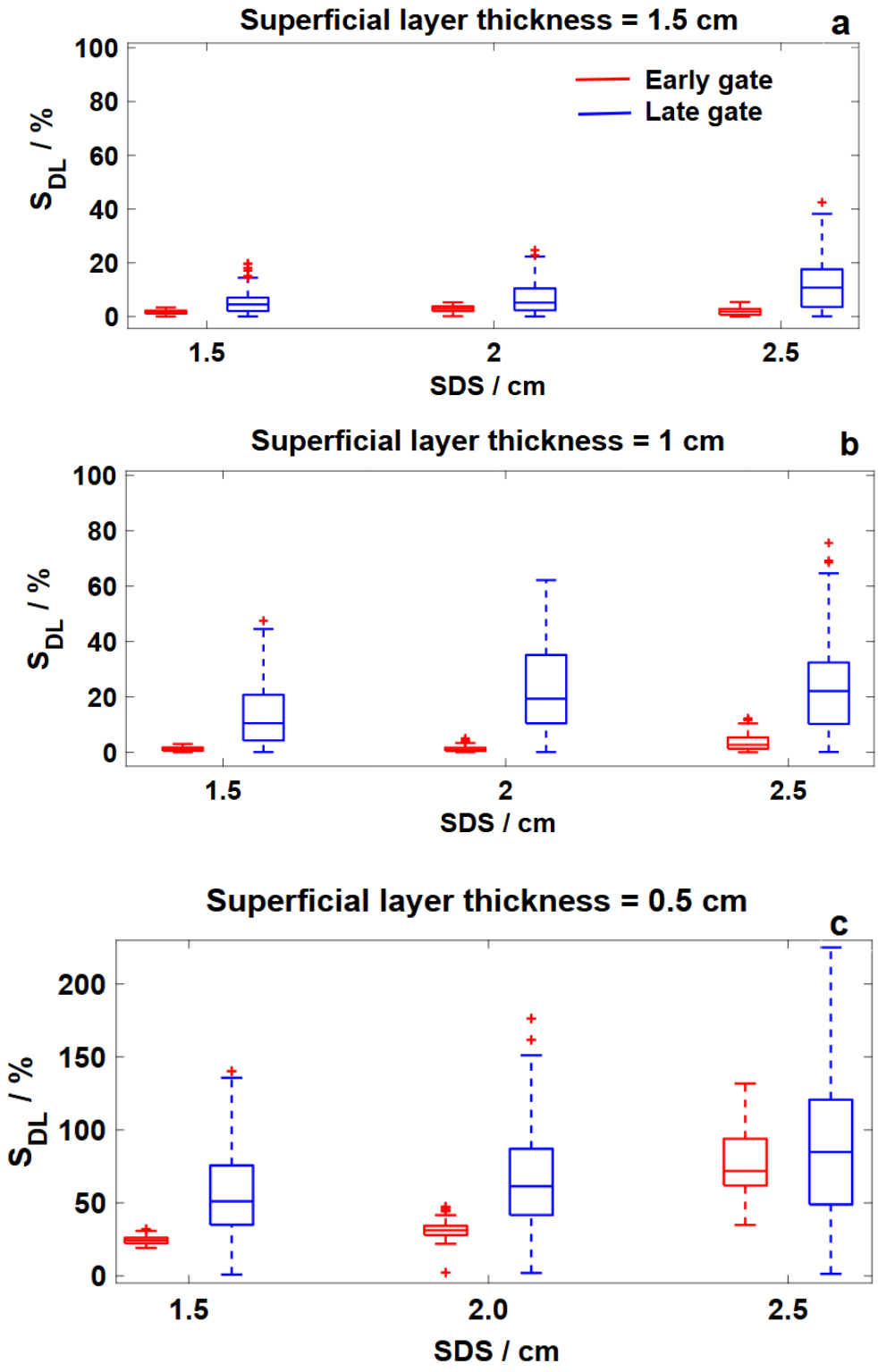


Figure 3.10 Sensitivity of the td-DCS to monitor the $\alpha D_b(t, t_s)$ of scatterers in deep layer (S_{DL} (t, t_s)) at SDS of a) 1.5, b) 2 and c) 2.5 cm for various top layer thickness. The data were calculated within early and late gates from 120 $g_2(t, t_s, \tau)$ collected with 2 s integration time each. In each boxplot, the central line represents the median, and the lower and upper edges indicate the 25th and 75th percentiles. The whiskers extend to the most extreme data points, not considering outliers. Outliers are indicated by plus signs. The figure was adapted from N. Mogharari et al. [39].

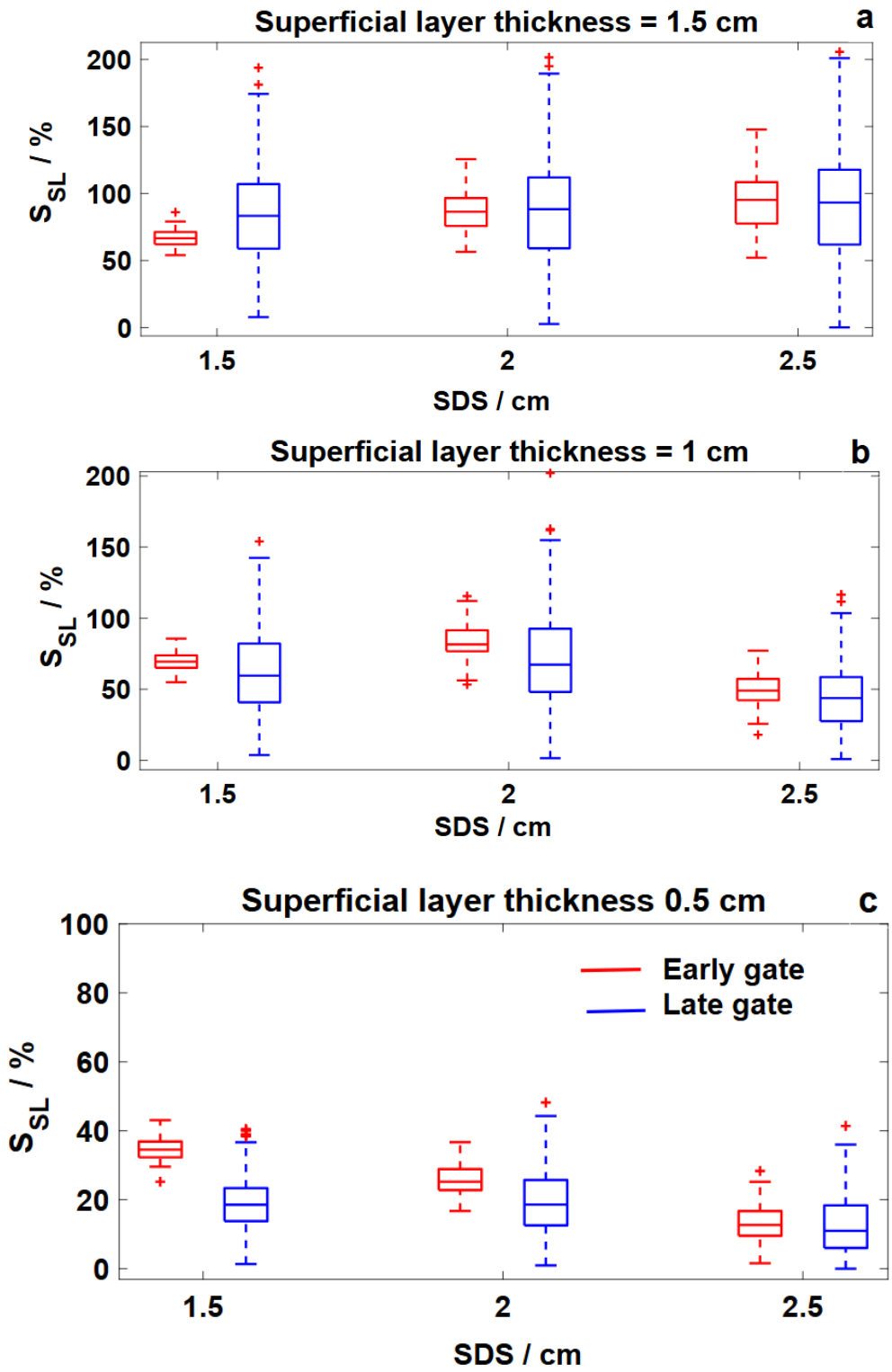


Figure 3.11 Sensitivity of the td-DCS to monitor the $\alpha D_b(t, t_s)$ of scatterers in superficial layer ($S_{SL}(t, t_s)$) at SDS of a) 1.5, b) 2 and c) 2.5 cm for various top layer thickness. The data were calculated within early and late gates from 120 $g_2(t, t_s, \tau)$ collected with 2 s integration time each. In each boxplot, the central line represents the median, and the lower and upper edges indicate the 25th and 75th percentiles. The whiskers extend to the most extreme data points, not considering outliers. Outliers are indicated by plus signs. The figure was adapted from N. Mogharari et al. [39].

In vivo measurements: In order to compare td-DCS performance at shorter (1.5 cm) and larger (2 and 2.5 cm) SDSs in monitoring muscle and cerebral blood flow changes, series of measurements was performed. These measurements included forearm muscle occlusion test and respiratory challenges.

According to figure 3.12 (b), the rBFI changes calculated from the photons detected in the early and late gates, regardless of the SDS, are not significantly different, measured over all subjects. Since the pressure was applied to the entire forearm, it affects both skin and muscles, which leads to the BFI changes detected at both the early and late gates. On the other hand, according to the phantom experiments (figure 3.10 c) in the case of a thin superficial layer thickness (here the forearm skin), the rBFI calculated from the photons detected in early gate at all SDSs is strongly affected by the blood flow changes in the deep layer.

The difference between the hyperaemic response for the PORH peak at different SDSs is more visible (figure 3.12 c). As it was discussed before, an increase in SDS leads to the shift of the DTOF peak to a later time, and based on the proposed gating strategy, it increases the possibility of detecting photons with longer time of flight. The PORH peak from longer SDSs (2 and 2.5 cm) is stronger with statistically significance than from short SDSs (1.5 cm) which might be due to the stronger response originated from the deep layer, the muscle [30].

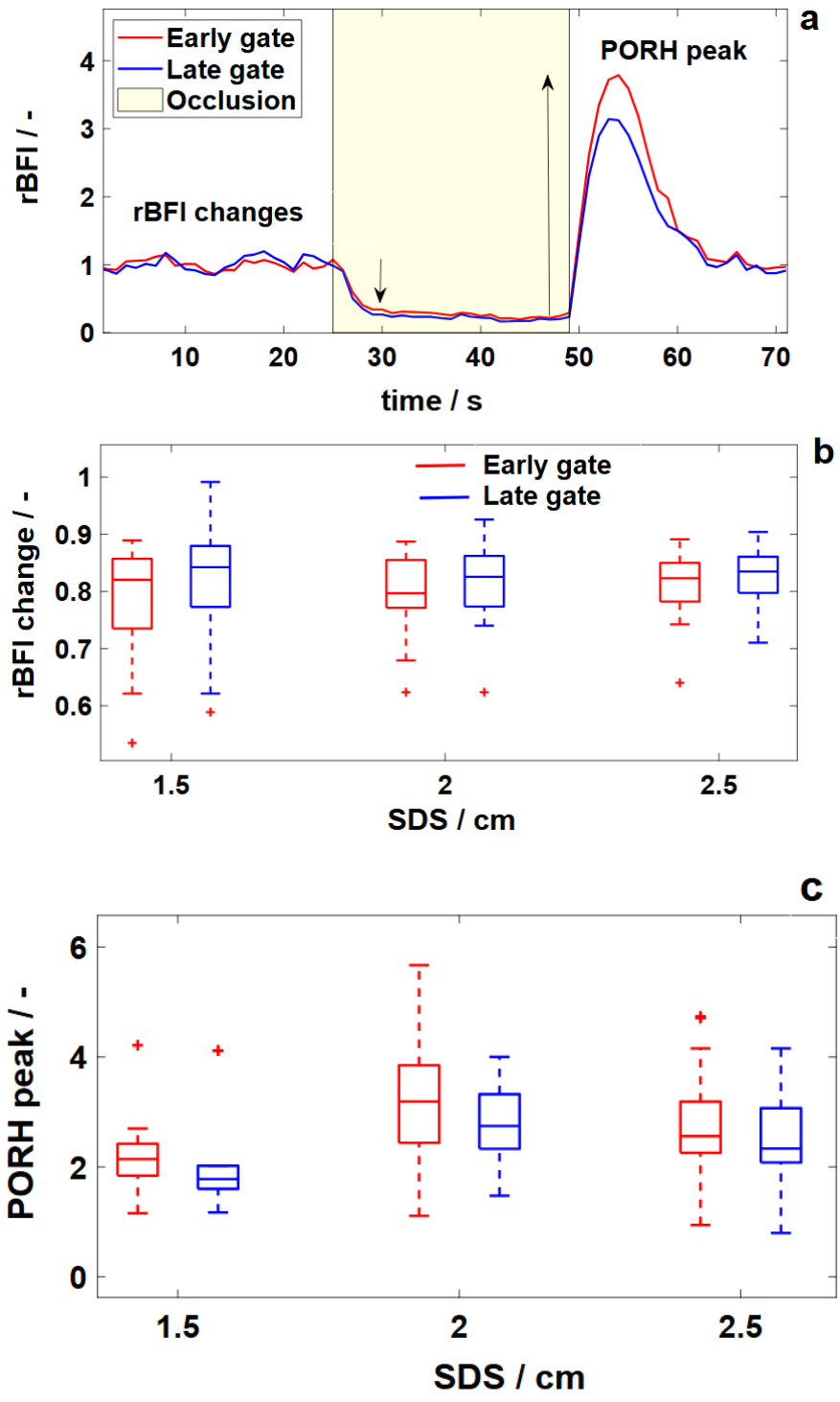


Figure 3.12 a) Schematic of the hemodynamic changes in response to the arterial occlusion (180 mmHg) measured at SDS = 2 cm on a healthy adult volunteer. b) The rBFI change (from baseline to arterial occlusion). c) The PORH peak at three SDSs. The statistics (b, c) are calculated from 16 datasets. In each boxplot, the central line represents the median, and the lower and upper edges indicate the 25th and 75th percentiles. The whiskers extend to the most extreme data points, not considering outliers. Outliers are indicated by plus signs. The figure was adapted from N. Mogharari et al. [39].

To compare the performance of td-DCS at shorter (1.5 cm) and larger (2 and 2.5 cm) SDSs in monitoring the CBF changes, BH and HV respiratory challenges were performed by healthy adult volunteers (protocols detailed in 2.4.2 In vivo experiments protocol - respiratory challenges). Figure 3.13 and 3.14 shows the rBFI changes in response to BH and HV respectively. During the respiratory challenge measurements, data collected from two subjects at SDS = 2.5 cm showed significant noise in the estimated BFI. Moreover, no clear changes were observed in BFI in response to BH and HV challenges. Therefore, these signals were excluded from further averaging and statistical analysis. The rBFI changes at early and late gates were calculating by normalizing the BFI to the baseline value. The increase in response to BH and decrease in response to HV can be seen in rBFI calculated at all SDSs.

BH and HV induce a global response in both extracerebral and intracerebral tissues [31, 172]. According to the phantom experiments (figure 3.11 a, b) in the case of a thick superficial layer thickness (comparable to scalp and skull thicknesses) and its high αD_b, the detected signal is dominated by superficial layer flow. As a result, the rBFI calculated from photons in both the early and late gates, at all SDSs, is strongly influenced by blood-flow changes in the superficial layer. However, still larger SDSs are more capable to minimize the αD_{b} changes in superficial layer and detect the αD_{b} changes in deeper layer. Moreover, these respiratory challenges have most likely different strength [173, 174] in extra and intracerebral layer, leading to different amplitude of rBFI changes at shorter and larger SDSs.

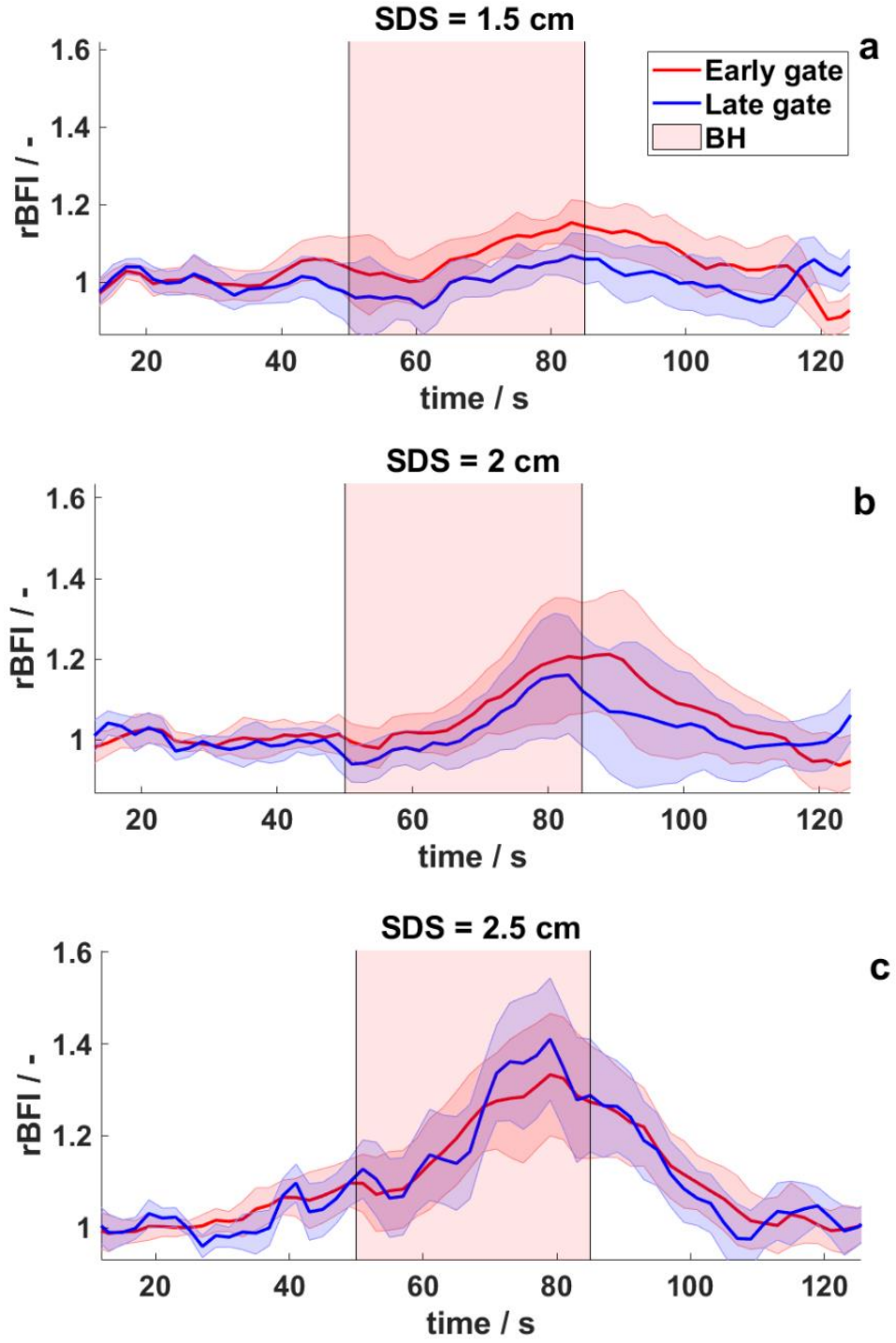


Figure 3.13 rBFI changes during BH at shorter (1.5 cm) and larger (2 and 2.5 cm) SDSs. Solid line and shaded area refer to mean value and standard deviation of the data calculated from 12 datasets at a) SDS = 1.5 and b) SDS=2 cm, and c) 8 datasets at SDS = 2.5 cm (Data from two subjects at SDS=2.5 cm was collected with a significant noise level. This data was excluded from further averaging and statistical analysis). Shaded areas indicate the task period. The figure was adapted from N. Mogharari et al. [39].

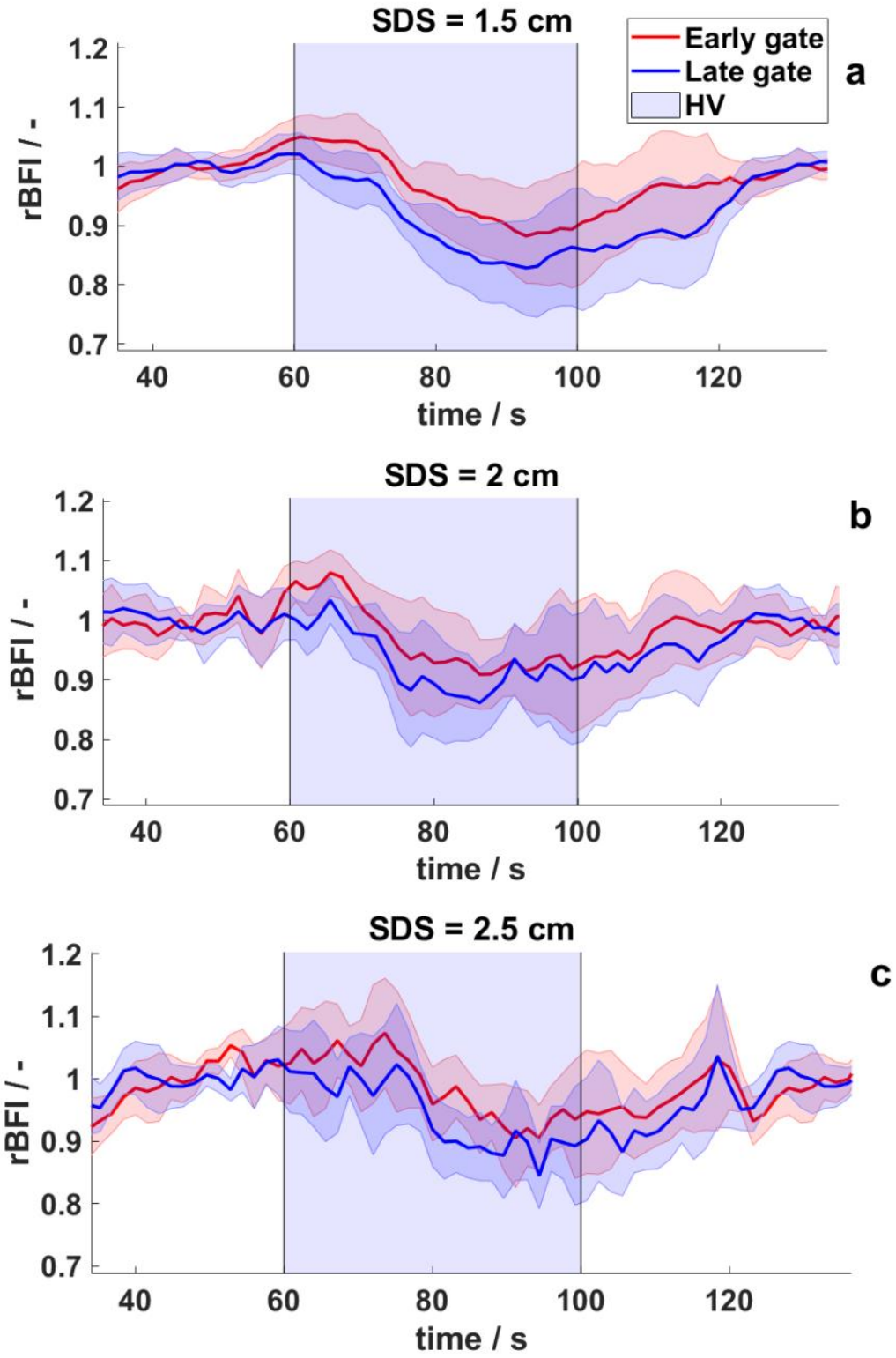


Figure 3.14 rBFI changes during HV at shorter (1.5 cm) and longer (2 and 2.5 cm) SDSs. Solid line and shaded area refer to mean value and standard deviation of the data calculated from 12 datasets at a) SDS = 1.5 and b) SDS=2 cm, and c) 8 datasets at SDS = 2.5 cm (Data from two subjects at SDS=2.5 cm was collected with a significant noise level. This data was excluded from further averaging and statistical analysis). Shaded areas indicate the task period. The figure was adapted from N. Mogharari et al. [39].

Figure 3.15 (a) and (b) show the statistical analyses of the rBFI changes induced by BH and HV. The rBFI changes were calculated from the mean difference between the rBFI of baseline and during the respiratory challenges (from 10 seconds after the start to 10 seconds after the completion of the task). The rBFI change induced by BH (figure 3.15 (a)) increases at larger SDS, while it slightly decreases in response to HV at larger SDS (Figure 3.15 (b)). No statistically significant difference was observed between the rBFI calculated from the photons detected at defined early and late gates at all SDSs. Moreover, only the difference between the rBFI changes during BH measured at 1.5 and 2.5 cm is statistically significant.

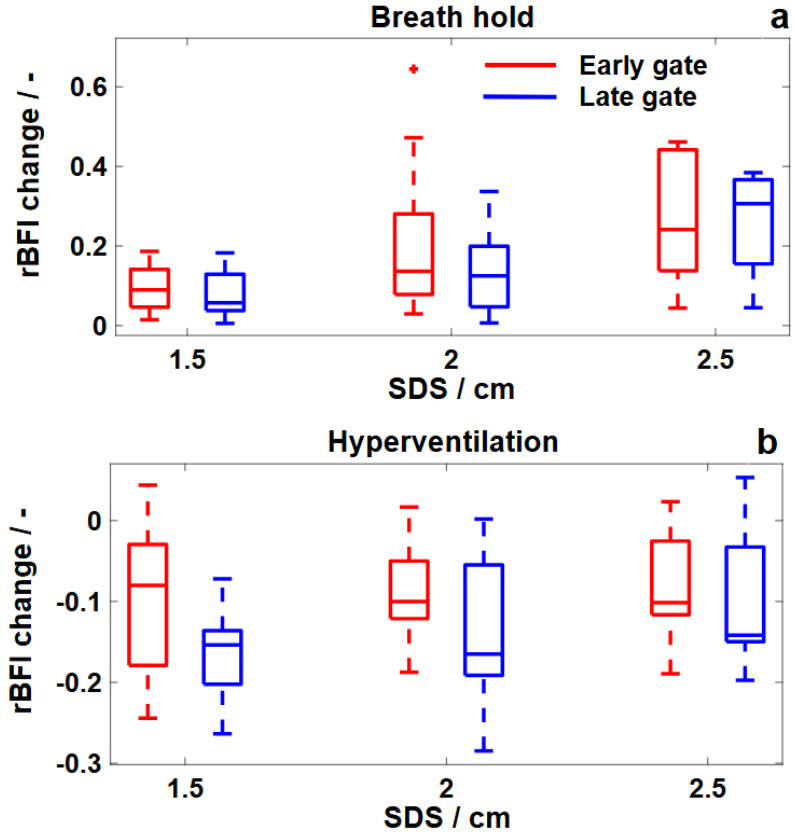


Figure 3.15 The distribution of rBFI changes caused by a) BH and b) HV at three SDSs of 1.5, 2 and 2.5 cm. Each boxplot calculated from 12 datasets at SDS = 1.5 and 2 cm, and 8 datasets at SDS = 2.5 cm (Data from two subjects at SDS of 2.5 cm was collected with a significant noise level and excluded from further averaging and statistical analysis). rBFI change refers to differences between the average rBFI of the baseline and the average rBFI in response to each task (from 10 seconds after the start time to 10 seconds after the completion of the task). In each boxplot, the central line represents the median, the lower and upper edges indicate the 25th and 75th percentiles, respectively. The whiskers extend to the most extreme data points, not considering outliers. Outliers are indicated by plus signs. The figure was adapted from N. Mogharari et al. [39].

In response to the Valsalva manoeuvre, it is expected that rBFI have initial increase, transient and continuous reduction during manoeuvre and rapid recovery or overshoot during the release phase. These trends of rBFI changes are more visible at SDS of 2.5 cm (figure 3.16), whereas SDS of 1.5 cm is predominantly influenced by superficial (skin) blood flow changes.

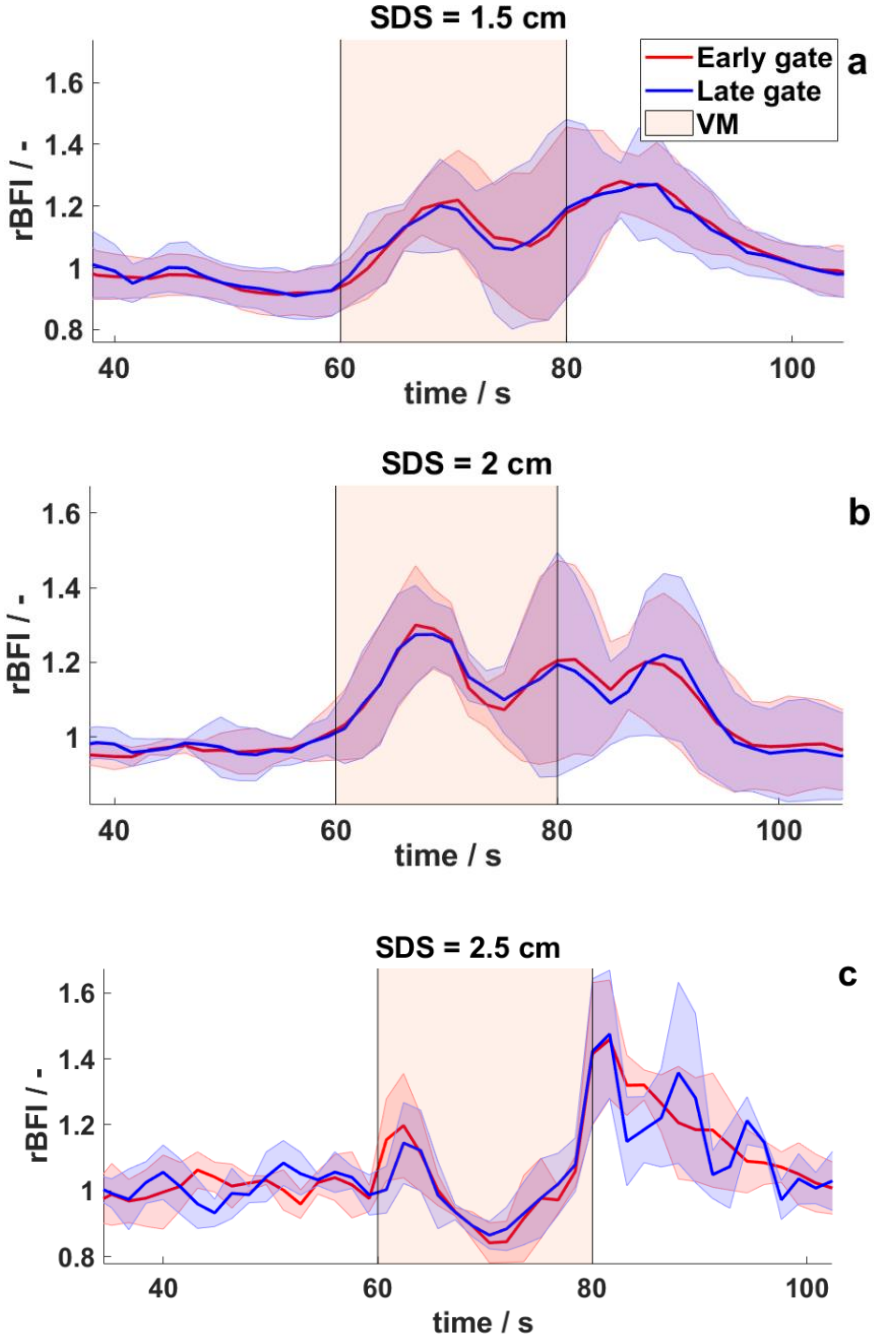


Figure 3.16 rBFI changes during Valsalva manoeuvre (VM) at SDS of a) 1.5, b) 2 (b) and c) 2.5 cm. Solid line and shaded area refer to mean value and standard deviation of data calculated from 8 datasets at SDS = 1.5 and 2 cm, and 6 datasets at SDS = 2.5 cm (Data from one subject at SDS 2.5 cm was collected with a significant noise level. This data was excluded from further averaging and statistical analysis).

3.2 Correlation of Hemodynamic Responses Measured by DCS and BOLD-MRI

In this section, using the optical DCS system, the correlation between the hemodynamic responses measured by DCS and BOLD-MRI in response to respiratory challenges were evaluated.

To do that, first the cw-DCS and td-DCS performance to monitor the αD_{b} of scatterers contained in the superficial and deeper layer of the two-layered phantom were assessed. These data help to understand how BFI measured by each DCS modality reacts to extracerebral and intracerebral blood flow changes.

Then, the correlation of the BFI measured by cw-DCS and td-DCS and BOLD signal changes measured by BOLD-MRI technique were evaluated. Finally, the BFI and BOLD signals changes were combined to estimate the cerebral metabolic rate of oxygen ($CMRO_2$). These results support the potential of DCS to monitor CBF with good temporal resolution as well as the DCS applicability as complementary tool to BOLD-MRI in assessing the $CMRO_2$.

Phantom experiment: To evaluate and compare the performance of cw-DCS and td-DCS in detecting the αD_{b} changes in superficial and deeper layer, series of measurements were performed on two-layered phantom (detailed in 2.4.1 Physical phantom - homogenous and two layered phantoms). The two-layered phantom measurements as a simplified model of human head help to better interpret the signals measured on superficial and deeper layer of human head.

Figure 3.17 presents the β and normalized αD_b ($n\alpha D_{\mathrm{b}}$) (calculated based on data analayses detailed in 2.5.2 DCS technique – normalized αD_{b}) values obtained using two fitting approaches in cw-DCS (detailed in 2.5.2 DCS technique - cw-DCS fitting scenarios) and the early and late gates in td-DCS (detailed in 2.5.2 DCS technique – time gating strategy in td-DCS), measured on homogenous and two-layered phantoms. The lower coherence length of the pulsed laser used in td-DCS (3.8 cm), in contrast to the much longer coherence length of the continuous-wave laser (>10 meters), resulted in a notably reduced β parameter (figure 3.17 a) and greater standard deviation in the $n\alpha D_{\mathrm{b}}$ values.

Figure 3.17 (b) illustrates the $n\alpha D_b$ values obtained during measurements on two-layered phantom (detailed in 2.5.1 Physical phantom - homogenous and two layered phantoms) in which the deeper layer has higher αD_b. In cw-DCS technique where the fitting approach limited fitting range to the $g_1 > 0.7$, yielded significantly higher $n\alpha D_b$ values compared to fitting across the entire g_1 curve, indicating enhanced sensitivity to deep layer. For td-DCS, a statistically significant difference between the $n\alpha D_b$ values derived from the early and late time gates supported the effectiveness of the proposed time-gating strategy [38]. It showed the signals obtained using early gates are more sensitive to changes in αD_b of scatterers distributed in superficial layers of the tissue. While the signals obtained using late gates are more sensitive to changes in αD_b of scatterers distributed in the deeper layers of tissue. However, the increased standard deviation observed in the estimated $n\alpha D_b$ from the signal obtained in late gate, suggests that td-DCS does not substantially improve sensitivity to changes in αD_b of scatterers distributed in deeper layer compared to the cw-DCS technique while employing the $g_1 > 0.7$ fitting scenario.

Figure 3.17 (c) illustrates how higher αD_b of scatterer in the superficial layer affected the detected signals by each DCS modalities. In cw-DCS data, no statistically significant difference ($P > 0.05$) was observed between the $n\alpha D_b$ values derived from two fitting approaches, suggesting limited ability in minimizing the αD_b of scatterers in superficial layer. In contrast, the $n\alpha D_b$ obtained from the late gate of td-DCS was significantly lower than those from the early gate and both cw-DCS fitting scenarios. This finding highlights td-DCS has better capability in reducing the influence of higher αD_b of scatterer within the superficial layer.

Based on the median $n\alpha D_b$ values, the contributions of deep-layer αD_b of scatterer to the detected signals using cw-DCS (when fitting $g_1 > 0.7$) and td-DCS (late gate) were approximately 80%, 30%, and 5% for superficial layer thicknesses of 0.5 cm, 1 cm, and 1.5 cm, respectively. Conversely, the contribution of the αD_b of scatterer in superficial layer measured by cw-DCS (when fitting to whole g_1) and td-DCS (early gate) is approximately 5–10%, 20–30%, and 80% for the same corresponding thicknesses. These results demonstrate the sensitivity characteristics of both modalities under varying conditions. However, for two-layered phantoms with different superficial layer thickness, optical properties and αD_b, these estimations may differ.

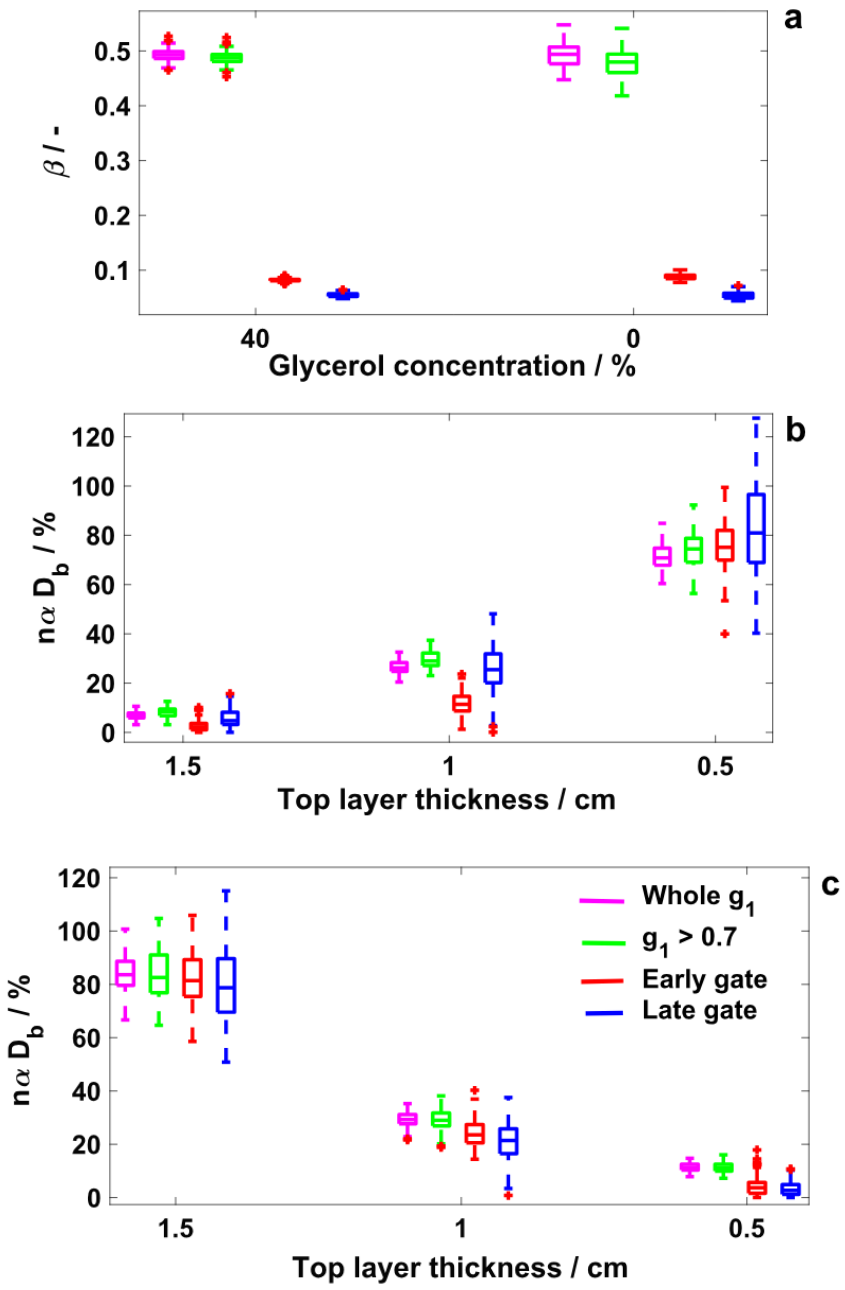


Figure 3.17 a) Calculated β for the homogenous phantom with 40% and 0% Glycerol concentrations. $n\alpha D_b$ represents the sensitivity to detect αD_b changes in b) deep and c) superficial layers measured by cw-DCS and td-DCS techniques on two-layered phantom. For cw-DCS, the metrics have been calculated by fitting the whole g_1 curve as well as $g_1 > 0.7$. For td-DCS the metrics have been calculated from detected photons in defined early and late gates. Each boxplot acquired within 120 g_2 curve with 2.5 s integration time. In each boxplot, the central line represents the median, the lower and upper edges indicate the 25th and 75th percentiles, respectively. The whiskers extend to the most extreme data points, not considering outliers. Outliers are indicated by plus signs. The figure was adapted from N. Mogharari et al. [175].

In vivo experiments: To evaluate the correlation between the hemodynamic response measured by DCS modalities and BOLD-MRI, series of respiratory challenges was performed by volunteers. Figure 3.18 (a) and (b) display the spatial distribution of BOLD signal changes, across different brain regions, averaged over fourteen participants while performing BH and HV respiratory challenges. The group-level image averaging enhances the robustness of the findings and highlights the observed hemodynamic patterns. The maps illustrate both spatial and magnitude of BOLD signal changes caused by respiratory challenges. As shown in Figure 3.18 (c), BOLD signal changes corresponding to the extracerebral layer were derived from segmented scalp and skull regions (represented in blue and green, respectively). While the intracerebral BOLD signal was extracted from the segmented gray matter region (shown in red). These BOLD signal changes were used for further cross-correlation with BFI measured by DCS modalities.

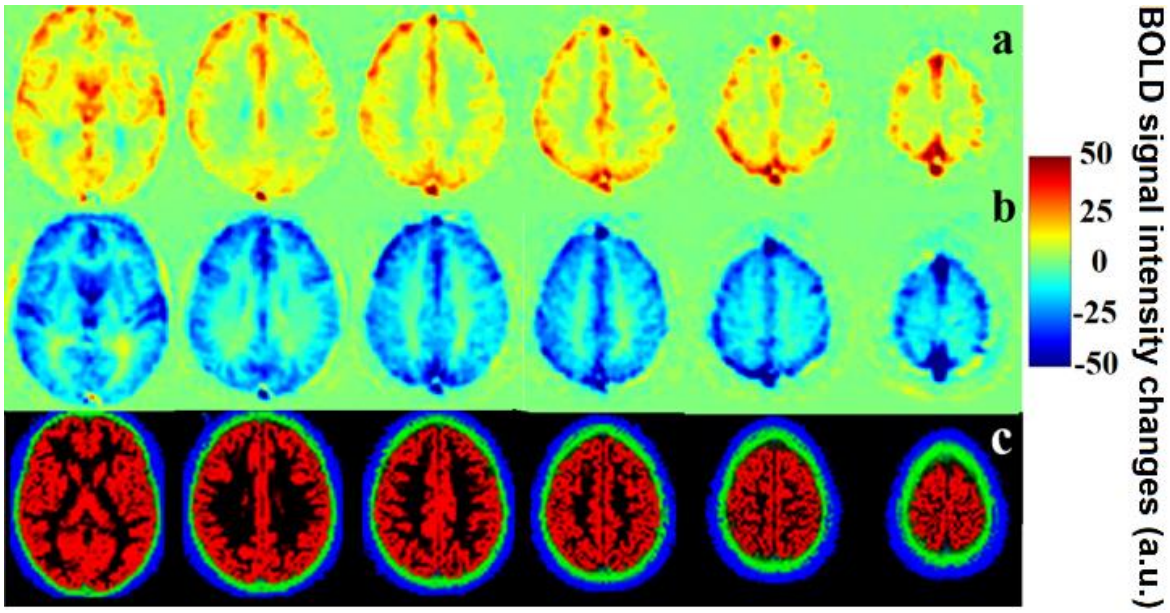


Figure 3.18 Panels a and b show the averaged BOLD signal maps from fourteen subjects during BH and HV respiratory challenges, respectively. The color bar represents the intensity of BOLD signal changes, where green indicates baseline, and red and blue regions correspond to significant increases and decreases in BOLD signal, respectively. The color scale applies exclusively to panels (a) and (b). Panel c displays the segmented tissue masks used for analysis: scalp (blue), skull (green), and gray matter (red). BOLD signals from the intracerebral layer were extracted specifically from the gray matter regions. The image slices were reconstructed with a thickness of 2.5 mm and were spaced at 12.5 mm intervals. The figure was adapted from N. Mogharari et al. [175].

Figures 3.19 and 3.20 present the group-averaged BOLD signal, heart rate (HR), oxygen saturation (SpO_2), and BFI changes recorded during the BH and HV respiratory challenges from region of interest presented in figure 3.18. Additional analysis using smaller regions of interest located directly beneath the DCS probes (figure 2.20 d) yielded similar results, with only minor fluctuations in the extracted BOLD signal that can be considered negligible, consistent with other report [176].

Sixteen healthy volunteers participated in the full protocol; however, data from two participants were excluded. One subject failed to perform the respiratory challenges correctly, resulting in the absence of clear physiological responses across BOLD, HR, SpO_2, and BFI signals. In another case, although BOLD, HR, and SpO_2 responses were evident, BFI changes were not observed, potentially due to poor contact between the optical probe and the scalp.

Each BH and HV trials comprised two repeated sessions. For each participant, the trial showing the most pronounced BFI changes measured by DCS modalities was selected for data analysis. This selection was based on the observation of plotted BFI changes in response to respiratory challenges. The BOLD, HR, SpO_2, and BFI changes were calculated relative to the mean values obtained during a 20-second baseline period preceding each respiratory challenge.

During BH, oxygen depletion causes a rise in HbR. The increase in $PaCO_2$ triggers vasodilation and elevates CBF, which in turn raises the BFI [177, 178] (Figures 3.19 c, d). Increased CBF leads to increase the blood oxygenation level, leading to an enhanced BOLD signal (Figure 3.19 a). It is noteworthy that the magnitude of changes in BFI and BOLD signals can vary across individuals. Additionally, BH-induced hypoxia often leads to a decrease in heart rate as a protective mechanism to reduce systemic oxygen demand, while sustained oxygen consumption results in a gradual drop in SpO_2 levels [179, 180] (Figure 3.19 b).

HV induces a decrease in $PaCO_2$, CBF [181] and as a result BFIs (Figures 3.20 c, d). Decreased CBF leads to decrease the blood oxygenation level and hence decreased BOLD signal [176] (Figure 3.20 a) . As shown in Figure 3.20 (b), there is a minimal difference in SpO_2 changes in responses to HV and only an increase in heart rate is significant [182].

A delay was observed between the onset of BH trial and the rise in BFI and BOLD signals. This delay is consistent with the time required for cerebral vessels to respond to the hypercapnic stimulus, characterized by a gradual increase in $PaCO_2$ [183]. A similar temporal delay was observed following the initiation of the HV trial, which results from the delayed reduction in $PaCO_2$ level, affecting cerebral vasculature and subsequent hemodynamic changes [184].

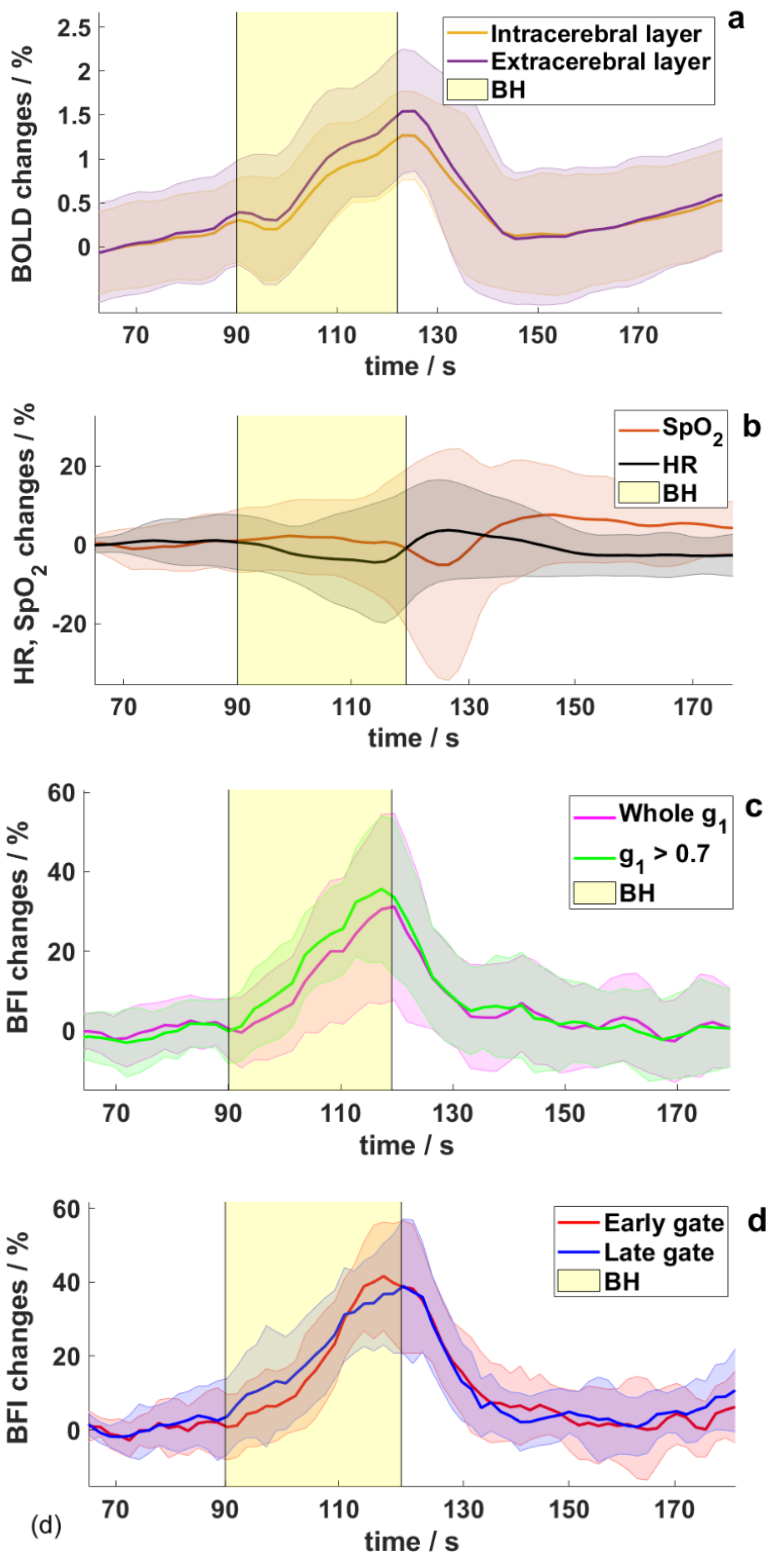


Figure 3.19 The group averaged signals of a) BOLD, b) heart rate (HR) and oxygen saturation (SpO_2), BFI measured by c) cw-DCS and d) td-DCS during BH (breath hold). The mean values (solid lines) and corresponding standard deviations (shaded areas) were obtained over 28 datasets measured from fourteen individual subjects. The vertical lines show the beginning and the end of BH respiratory challenge. The figure was adapted from N. Mogharari et al. [175].

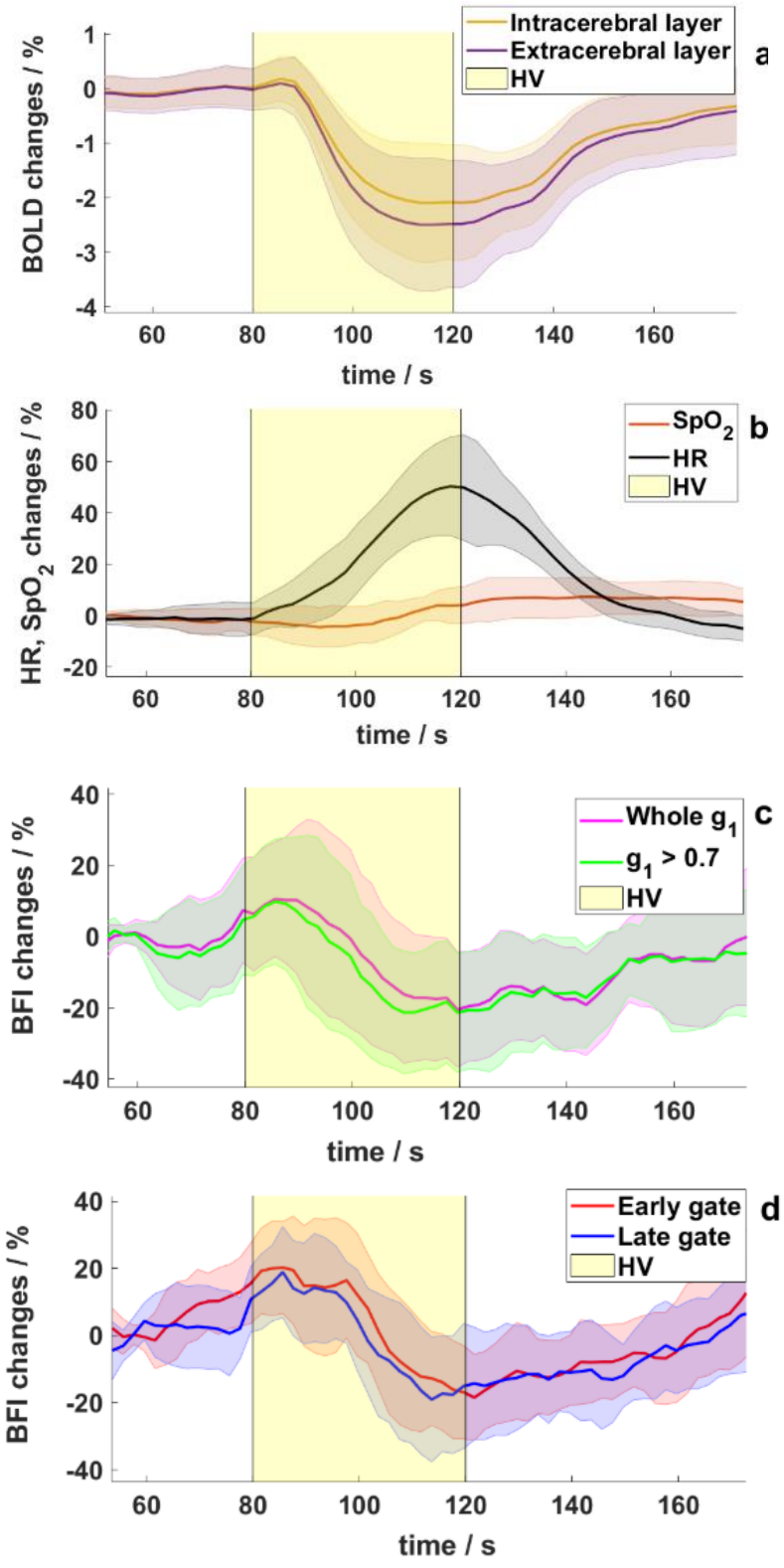


Figure 3.20 The group averaged signals of a) BOLD, b) heart rate (HR) and oxygen saturation (SpO_2), BFI measured by c) cw-DCS and d) td-DCS during HV (Hypertension). The mean values (solid lines) and corresponding standard deviations (shaded areas) were obtained over 28 datasets measured from fourteen individual subjects. The vertical lines show the beginning and the end of respiratory challenge. The figure was adapted from N. Mogharari et al. [175].

Figure 3.21 illustrates the amplitude changes of BFI and BOLD signals during BH and HV. The mean value of each signal has been calculated from 20 s after the beginning of the respiratory challenges' trial, for 20s. This time range was selected to capture the plateau phase of the hemodynamic response. As BH and HV are systemic and not regional or localized respiratory challenges, they affect the hemodynamic reactions in the whole head. Consequently, no statistically significant differences were observed in the BOLD signal amplitude changes between the intracerebral and extracerebral layers [185].

Based on the $n\alpha D_{\mathrm{b}}$ values obtained from the two-layered phantom experiments, signals derived from fitting the whole $g_1(\tau)$ curve in cw-DCS (detailed data analayses in 2.5.2 DCS technique - cw-DCS fitting scenarios) and from the early gate in td-DCS (detailed data analayses in 2.5.2 DCS technique – time gating strategy in td-DCS) are expected to be more influenced by the extracerebral layer. In contrast, fitting $g_1 > 0.7$ in cw-DCS (detailed data analayses in 2.5.2 DCS technique - cw-DCS fitting scenarios) and the late gate in td-DCS (detailed data analayses in 2.5.2 DCS technique – time gating strategy in td-DCS) are expected to showe increased sensitivity to the deeper tissue layers blood flow changes, particularly the intracerebral region. No statistically significant difference was found between the mean BFIs amplitude changes calculated from two fitting scenarios of cw-DCS as well as the mean BFI amplitude changes calculated from the early and late gates of td-DCS which agrees well with the results of BOLD signal changes.

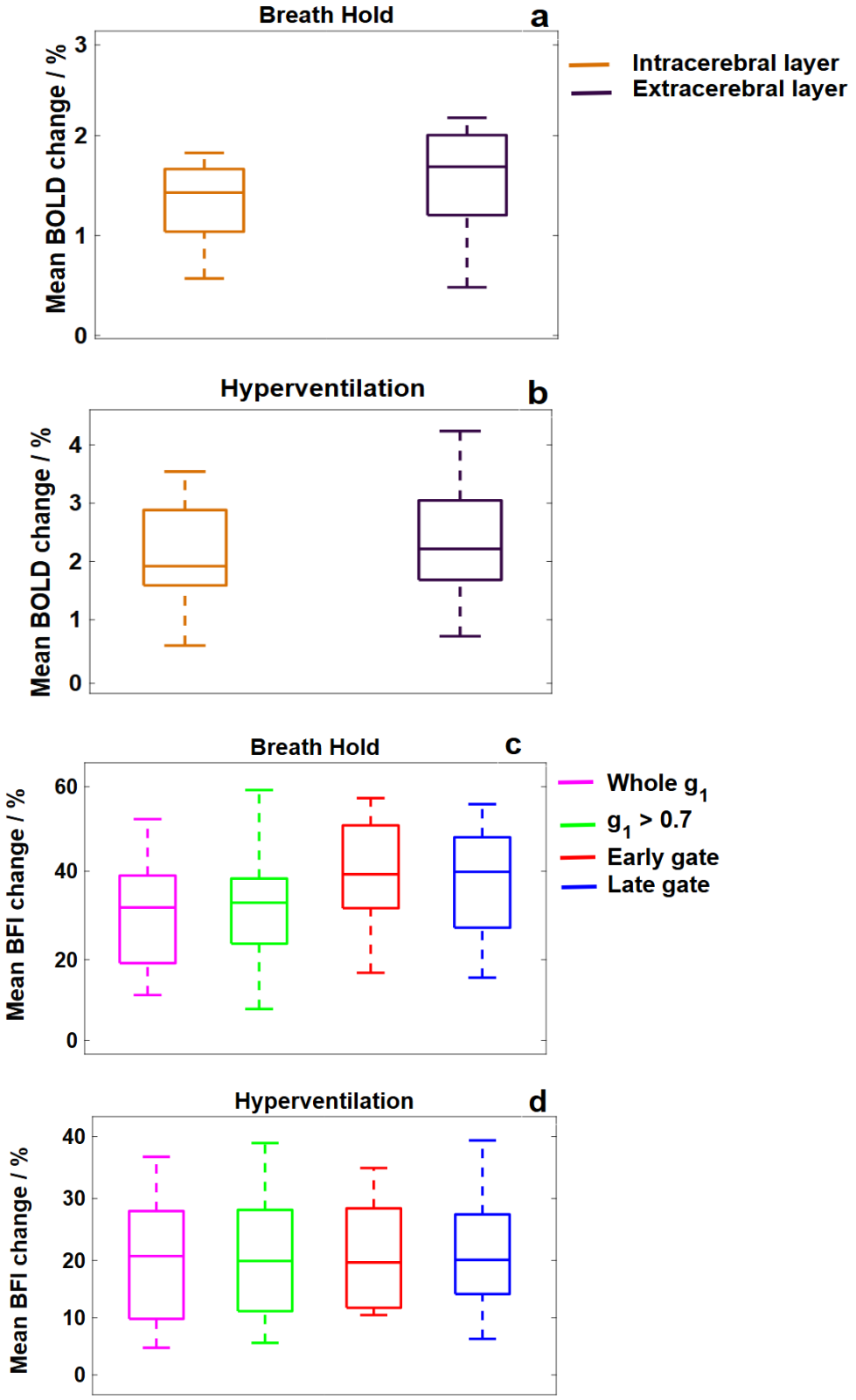


Figure 3.21 a, b) Mean BOLD signal changes and c, d) mean BFI changes calculated for breath hold and hyperventilation respiratory challenges. Each boxplot has been obtained from 28 data point. In each boxplot, the central line represents the median, the lower and upper edges indicate the 25th and 75th percentiles, respectively. The whiskers extend to the most extreme data points, not considering outliers. The figure was adapted from N. Mogharari et al. *[175]*.

To compare the temporal hemodynamic responses measured by DCS modalities and BOLD-MRI technique, hysteresis loops were generated by plotting the group-averaged normalized BFIs versus normalized BOLD signals changes (Figure 3.22). For assessing extracerebral responses, BFIs derived from fitting the whole $g_1(\tau)$ curve in cw-DCS and from the early gate in td-DCS were plotted versus the BOLD signals extracted from the extracerebral layer. Similarly, intracerebral responses were evaluated by plotting BFI values obtained from fitting the early portion of the $g_1(\tau)$ ($g_1(\tau) > 0.7$) curve in cw-DCS and the late gate in td-DCS against BOLD signals from the intracerebral layer. Then the hysteresis the loop directions were determined.

During the BH task, the loops displayed a clockwise direction, suggesting that changes in BFI precede the corresponding BOLD signal changes. This suggested that both intracerebral and extracerebral blood flow responses are initiated more rapidly than the associated oxygenation changes. The asymmetrical loop crossing above and below the unit line (where y=x) showed that BFIs and BOLD signals exhibit different phase relationships at the beginning and the end of the BH, suggesting that BFIs react faster to the BH and return to baseline earlier at the end of this respiratory challenge.

The counterclockwise directions of the hysteresis loop in response to HV is due to the delay of BFIs versus the BOLD signal. Moreover, the asymmetrical loops located under the unity line suggest that BOLD signal may respond faster than BFIs while returning to baseline after the HV respiratory challenge.

These phase relationships highlight distinct temporal characteristics in the vascular blood flow and oxygenation responses during respiratory challenges.

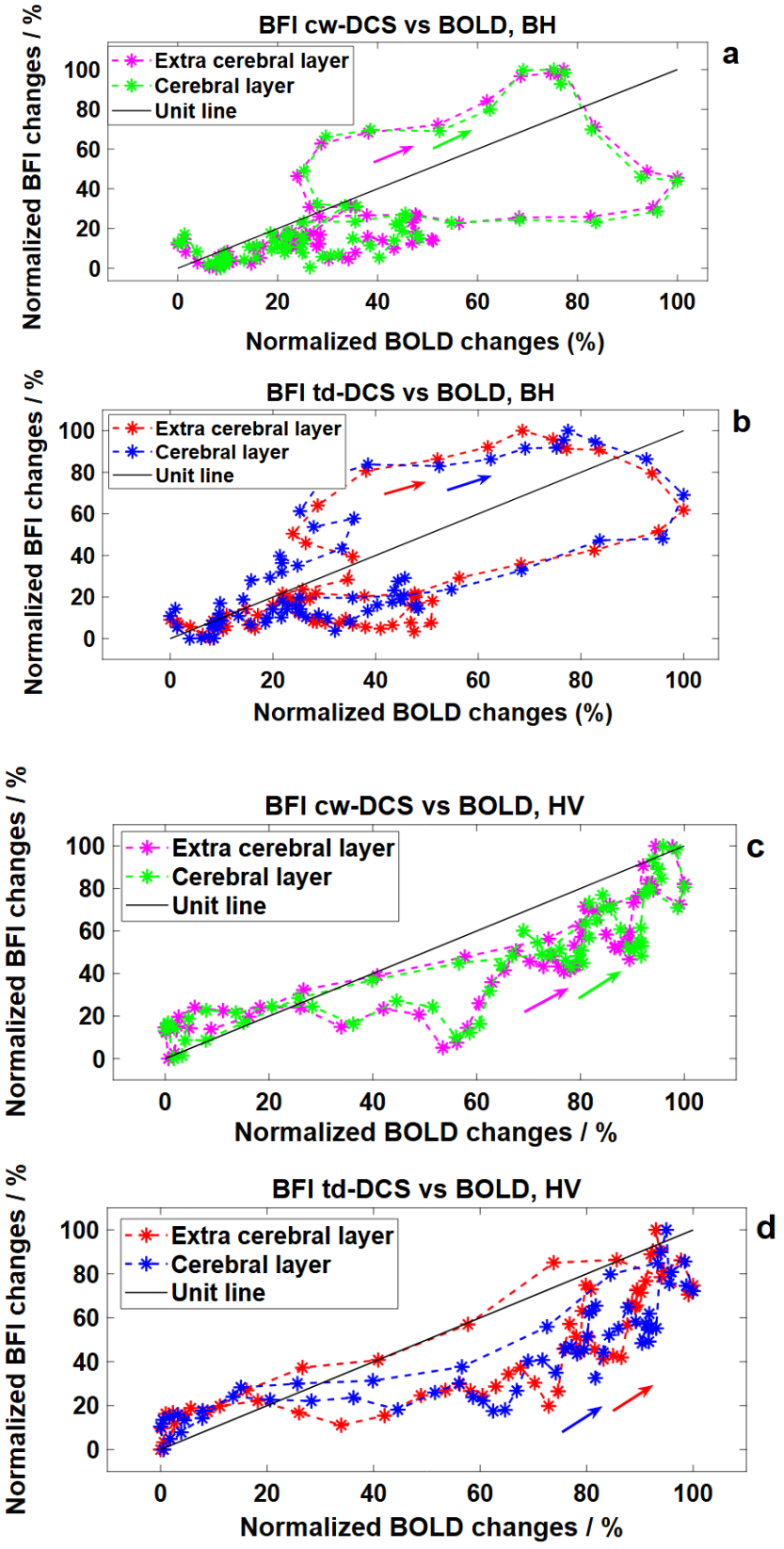


Figure 3.22 The hysteresis loops of the normalized BFIs versus BOLD signal changes during a, b) BH and c, d) HV tasks averaged over fourteen subjects. The arrows represent the loop's direction (clockwise and counter clockwise). The figure was adapted from N. Mogharari et al. [175].

Figure 3.23 presents the histograms (detailed in 2.5.5 Cross-analysis of the signals obtained by DCS, BOLD-MRI and IVIM-MRI) illustrating the delays between the BFI and BOLD signals changes of both intracerebral and extracerebral layers, analysed at the individual subject level. During the BH, BFIs measured using DCS modalities consistently preceded the corresponding BOLD signal changes, with an average time of approximately 2.7 seconds. Conversely, during the HV task, BOLD signals preceded the BFI responses. However, the average delay across subjects was minimal, around 0.2 seconds, indicating a less pronounced delay between the two signals in response to HV.

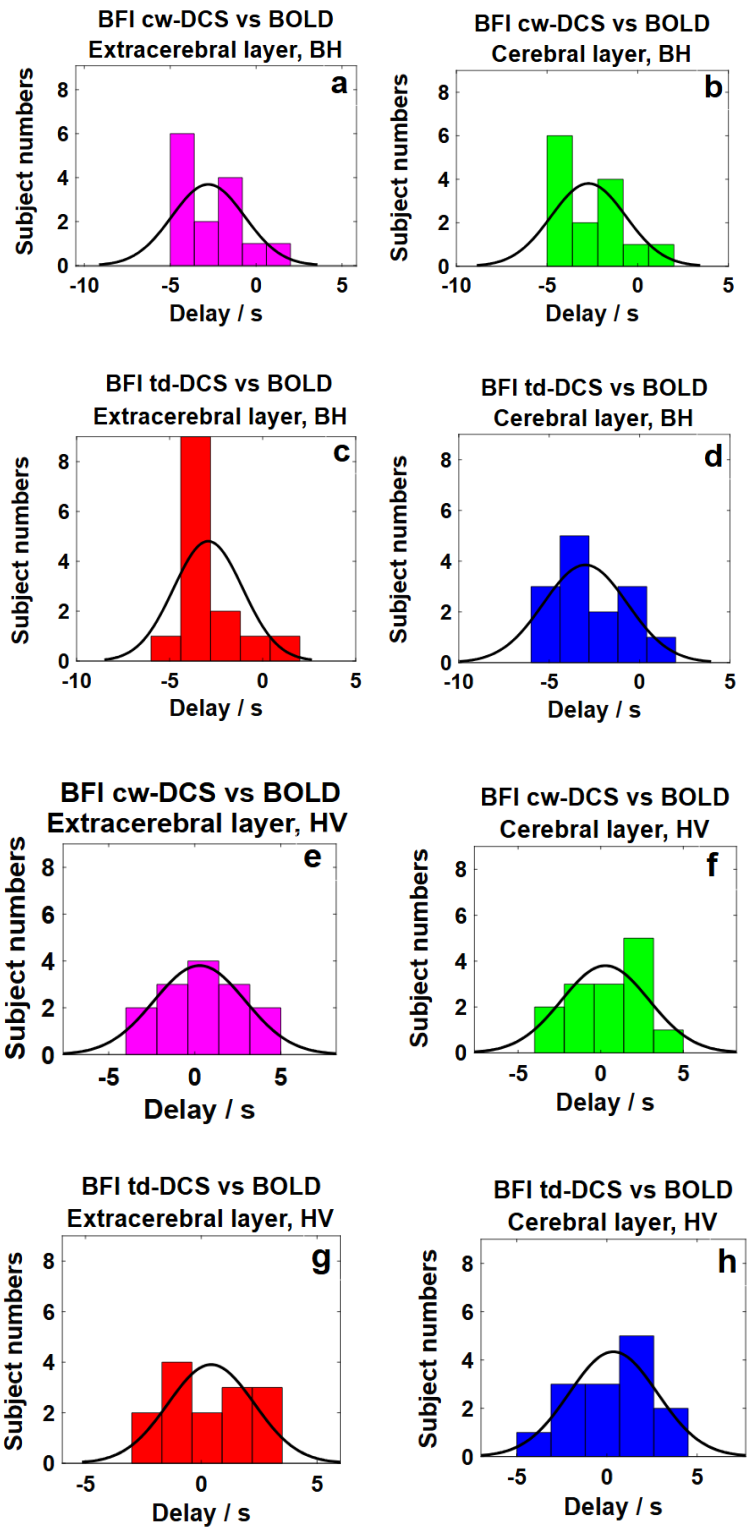


Figure 3.23 Histograms of delays between the hemodynamic responses measured by DCSs and BOLD-MRI techniques calculated for individual subjects. The negative and positive delays refer to the earlier and later appearance of the BFI response versus BOLD signal. The black lines show the center of the histogram and the averaged value of the delay between BFI and BOLD signal. The figure was adapted from N. Mogharari et al. [175].

The temporal correlation between the BFI and BOLD signal responses was analyzed using Pearson correlation coefficient (detailed in 3.4.5 Cross-analysis of the signals obtained by DCS, BOLD-MRI and IVIM-MRI) for both intracerebral and extracerebral layers. Correlations were calculated from the beginning of each respiratory challenges to 20 seconds after the end of BH and 40 seconds after the end of HV. As illustrated in Figure 3.24, a positive correlation ($r > 0.8$) was observed between the temporal response of BFI and BOLD signals for both BH and HV, indicating consistent coupling between blood flow and oxygenation responses during these respiratory challenges.

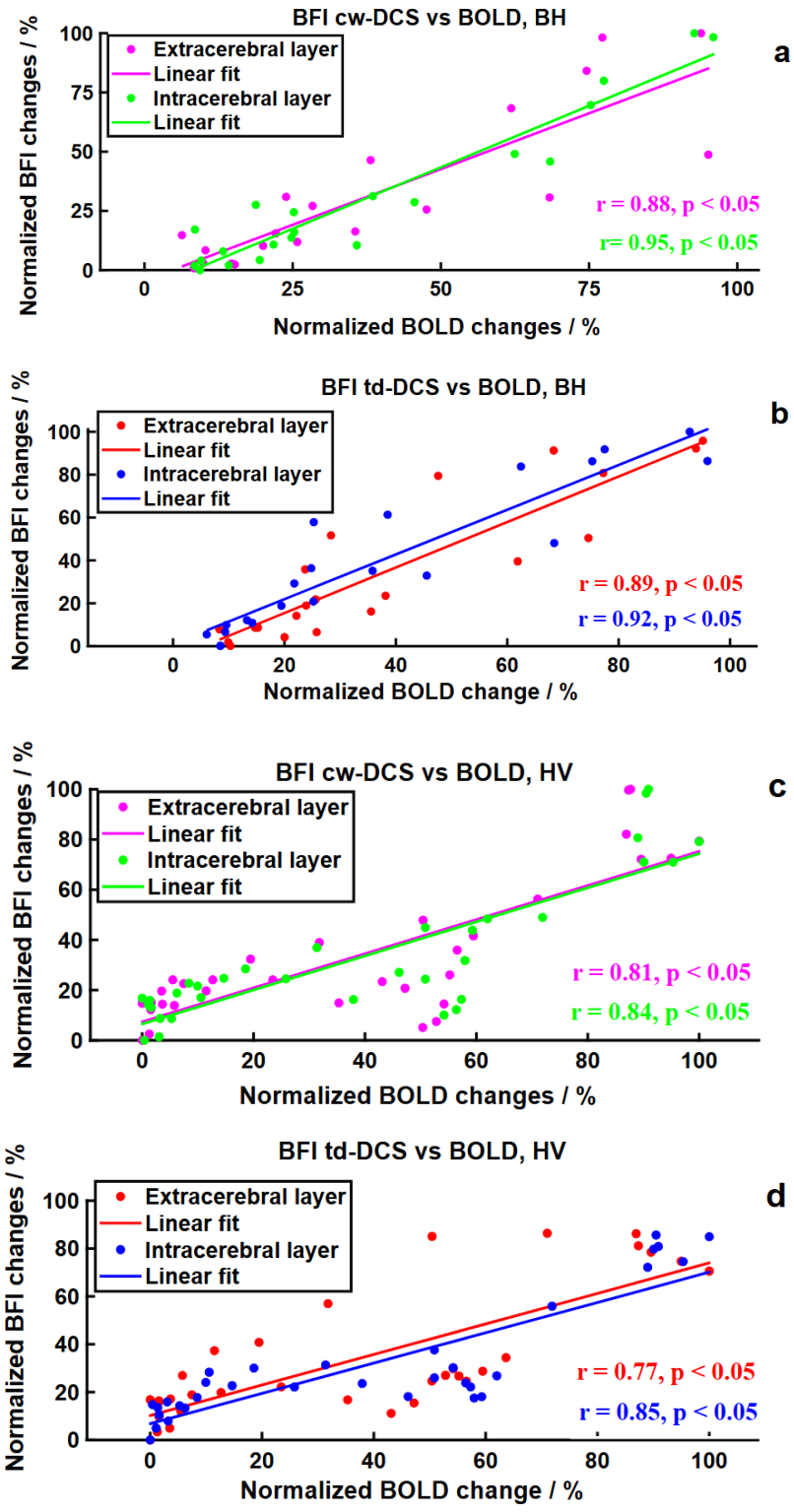


Figure 3.24 Scatterplot to compare the hemodynamic responses measured by a, b) cw-DCS and c, d) td-DCS versus BOLD-MRI techniques in response to BH and HV respiratory challenges. Each regression plot has been calculated for the acquired data from the beginning of the challenges to 20 s and 40 s after the end of the BH and HV, respectively. Y and X axis show percentage changes both from 0 to 100. The figure was adapted from N. Mogharari et al. [175].

Figure 3.25 presents the group-averaged of $rCMRO_2$ signals as the product of the BFI and BOLD signal changes, observed in response to BH (a) and HV (b) respiratory challenges. $CMRO_2$ is important parameter in neuroimaging and neurovascular coupling [139]. The BOLD constant parameter $M \approx 0.04$ has been calculated using equation 2.20. The M parameter has been calculated from the BOLD signal changes of intracerebral layer as well as the early portion of the autocorrelation curve ($g_1 > 0.7$) of cw-DCS and the late gate of td-DCS to estimate BFI changes (figure 3.19 and 3.20). The $rCMRO_2$ changes were also calculated based on these BOLD and BFI signal changes as they were expected to reveal higher sensitivity to intracerebral layer.

During the BH, $rCMRO_2$ raised by approximately 5% on average and then gradually returns to baseline after the respiratory challenge. In contrast, the $rCMRO_2$ decreased by 1% in response to HV. The $rCMRO_2$ showed similar trend of changes when calculated by BFI measured by each DCS modalities.

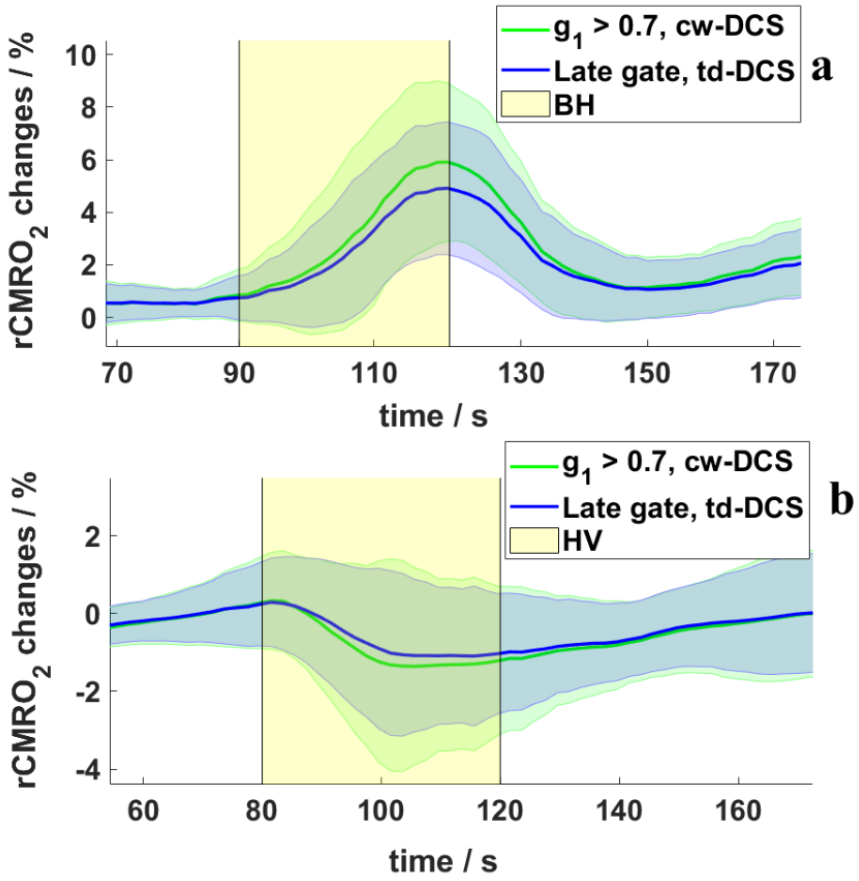


Figure 3.25 The group-averaged signals of $CMRO_2$ obtained in response to a) BH and b) HV. The green line represents the $CMRO_2$ changes calculated from BFI measured by cw-DCS when fitting $g_1 > 0.7$, and the blue line corresponds to BFI calculated from the late gate of td-DCS. The mean values (solid lines) and corresponding standard deviations (shaded areas) were obtained over 28 datasets measured from fourteen individual subjects. The vertical lines show the beginning and the end of respiratory challenges.

3.3 Cross evaluation of IVIM-MRI and DCS in measuring tissue perfusion/blood flow

In this section the correlation of IVIM-MRI derived parameters were evaluated with cw-DCS derived flow index during a series of tissue-mimicking phantom measurements and muscle occlusion tests performed on healthy adult volunteers.

Phantom experiments: To cross evaluate the BFI measured by DCS and perfusion-related motion and flow parameters measured by IVIM-MRI, first, series of measurements was performed on a tissue-mimicking phantom with tubes, designed to mimic the vascular structures within human muscle. The controlled tissue-mimicking phantom simplified the complexities of muscle tissue and provided more clear insight into the parameters measured by the IVIM technique.

Figure 3.26 shows the DWI image of tissue mimicking phantom from three orthogonal views. The highlighted area is the ROI (detailed data analayses in 2.5.4 Intravoxel Incoherent Motion MRI-Region of interest of DWI image) used to calculate the IVIM-derived parameters.

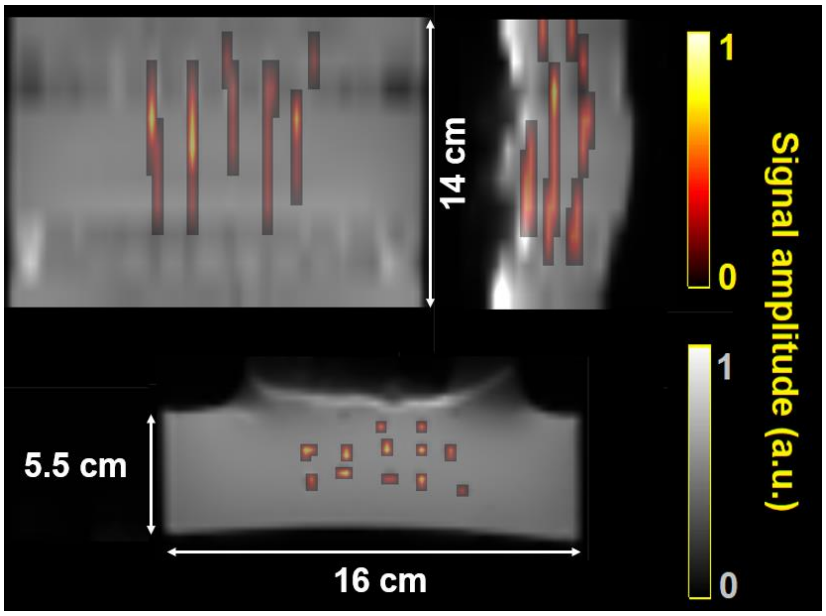


Figure 3.26 The DWI image of tissue mimicking phantom at pump flow rate (F_{pump}) of 2 mm^3/s. The color bars represent the signal amplitudes. The tissue mimicking phantom has the dimension of $16 \times 14 \times 5.5$ cm in length, width, and depth respectively.

Figure 3.27 shows the IVIM-derived parameters and cw-DCS derived flow index (FI_{DCS}) measured at baseline and at six pump flow rates (F_{pump}) from 1 to 6 mm^3/s. This measurement was repeated five times for baseline and each F_{pump}. Thus, each boxplot includes five data points. The experiment has been detailed in "2.4.1 Physical phantom - Tissue Mimicking Phantom". Increasing the F_{pump} led to statistically significant increase of the measured FI_{DCS} and D_{fast}. However, the difference between the measured D_{fast} at F_{pump} from 4 to 6 mm^3/s was not statistically significant. The D_{slow} was relatively unchanged ($\Delta D_{\mathrm{slow}} < 0.05\ 10^{-3}\ \mathrm{mm}^3/\mathrm{s}$) despite an increase in the F_{pump}. At baseline (zero flow), when there is no MR signal attenuation due to fast motion, the estimated f was close to zero, while applying the F_{pump} increased this parameter. The increased F_{IVIM} as the product of $f \cdot D_{\mathrm{fast}}$ can be observed in all flow rates with statistically significant differences except for F_{pump} from 4 to 6 mm^3/s.

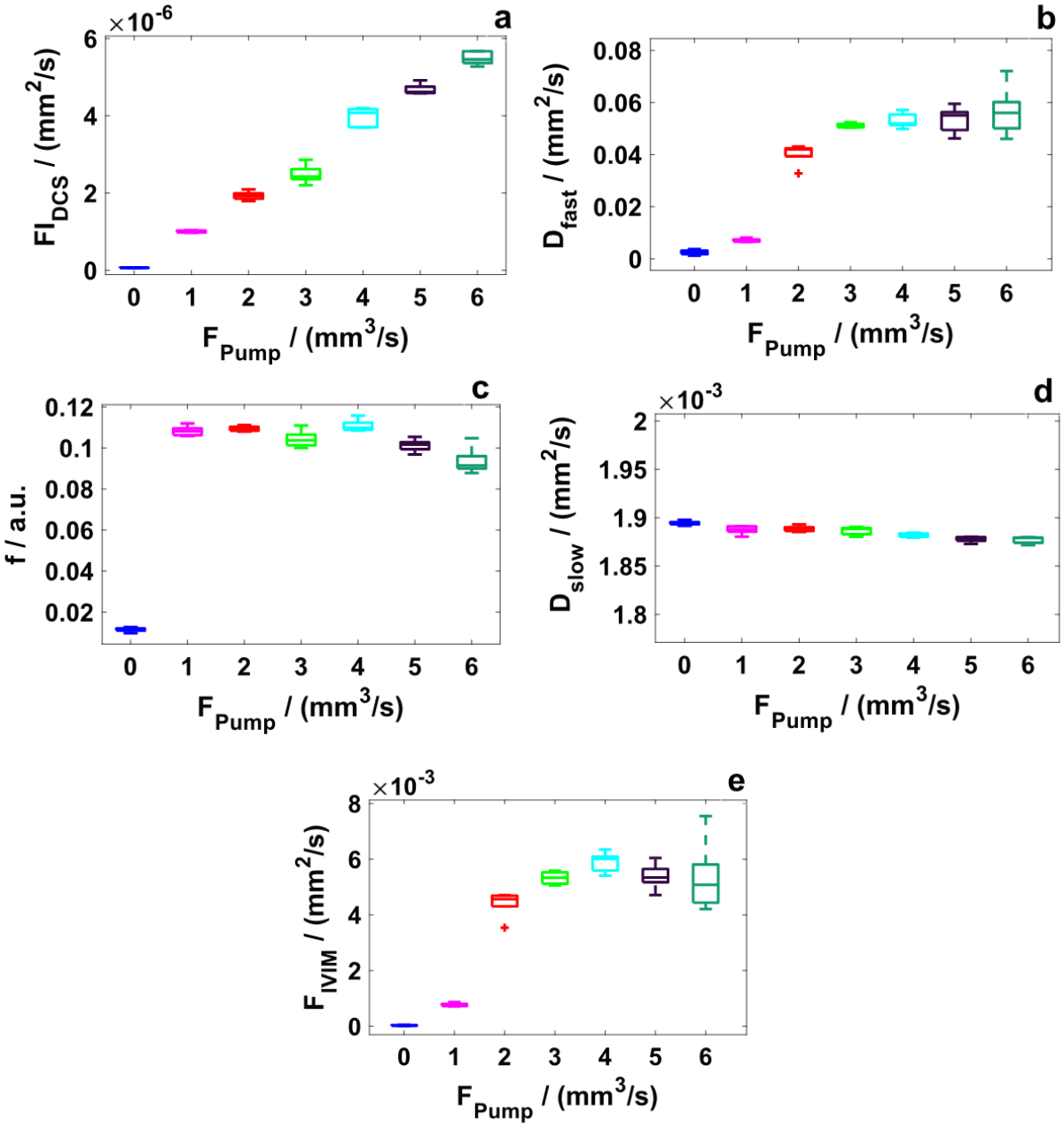


Figure 3.27 a) FI_{DCS} (DCS-derived flow index), b) D_{fast} (IVIM-derived pseudo diffusion coefficient), c) D_{slow} (IVIM-derived diffusion coefficient), d) f (IVIM-derived perfusion fraction), and e) F_{IVIM} (IVIM-derived flow) measured on tissue mimicking phantom at baseline and six F_{pump} (pump flow rate) from 1 to 6 mm^3/s. Each boxplot has been calculated from five data points. In each boxplot, the central line represents the median. The lower and upper edges indicate the 25th and 75th percentiles, respectively. The whiskers extend to the most extreme data points, not considering outliers.

To evaluate the correlation between the IVIM-derived perfusion and flow parameters and BFI measured by cw-DCS, two Pearson correlation coefficients (r) were calculated for acquired data of the tissue mimicking phantom. Each series of measurement was repeated five times at

baseline and each F_{pump}. The $r_{\text{Per measurement}}$ has been calculated by averaging the correlation of each series of measurements. The r_{Overall} has been calculated from the data points of all measurements together. Figure 3.28 (a) shows positive correlations of $r_{\text{Overall}} = 0.85$ and $r_{\text{Per measurement}} = 0.88 \pm 0.09$ between the D_{fast} and FI_{DCS}. The f depends on the volume of the flow changes in each voxel [186, 187], and was relatively constant during the experiment (figure 3.27 d). Therefore, F_{IVIM} correlates with FI_{DCS} (figure 3.28 b) similar way as D_{fast} does. The corresponding correlations are $r_{\text{Overall}} = 0.8$ and $r_{\text{Per measurement}} = 0.81 \pm 0.09$.

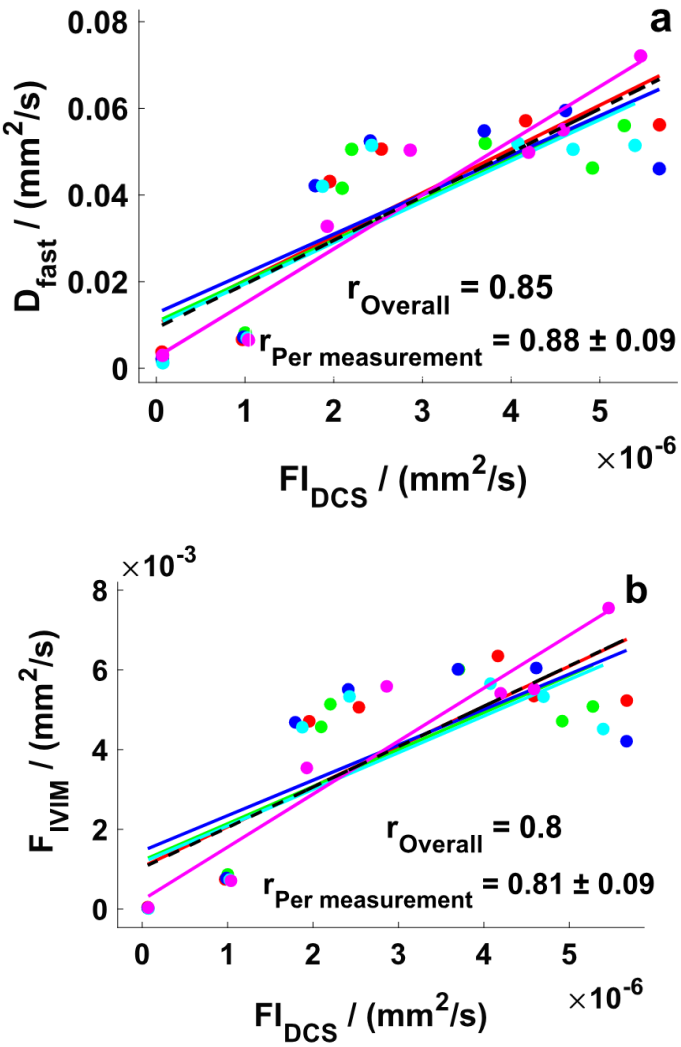


Figure 3.28 Correlation of a) D_{fast} (IVIM-derived pseudo diffusion coefficient), and b) $F_{\text{IVIM}} = f \cdot D_{\text{fast}}$ (IVIM-derived flow) with the FI_{DCS} (DCS-derived flow index) measured on tissue mimicking phantom at baseline and at six F_{pump} (pump flow rate) from 1 to 6 mm^3/s with the step of 1. Each color represents one series of measurements. Due to the small values of the measured FI_{DCS} and IVIM-derived parameters at baseline and the F_{pump} of 1-2 mm^3/s, the corresponding data points overlap.

Muscle occlusions experiments: To cross evaluate the IVIM-derived pseudo-diffusion coefficient and flow parameter with BFI measured by cw-DCS, series of muscle occlusion tests were performed on the healthy adult volunteers' leg and forearm. Figure 3.29 shows the DWI image of a volunteer's leg and forearm during baseline from three sides. The highlighted area is the ROI (detailed data analayses in 2.5.4 Intravoxel incoherent motion MRI - Region of interest of DWI image) used to calculate the IVIM-derived parameters.

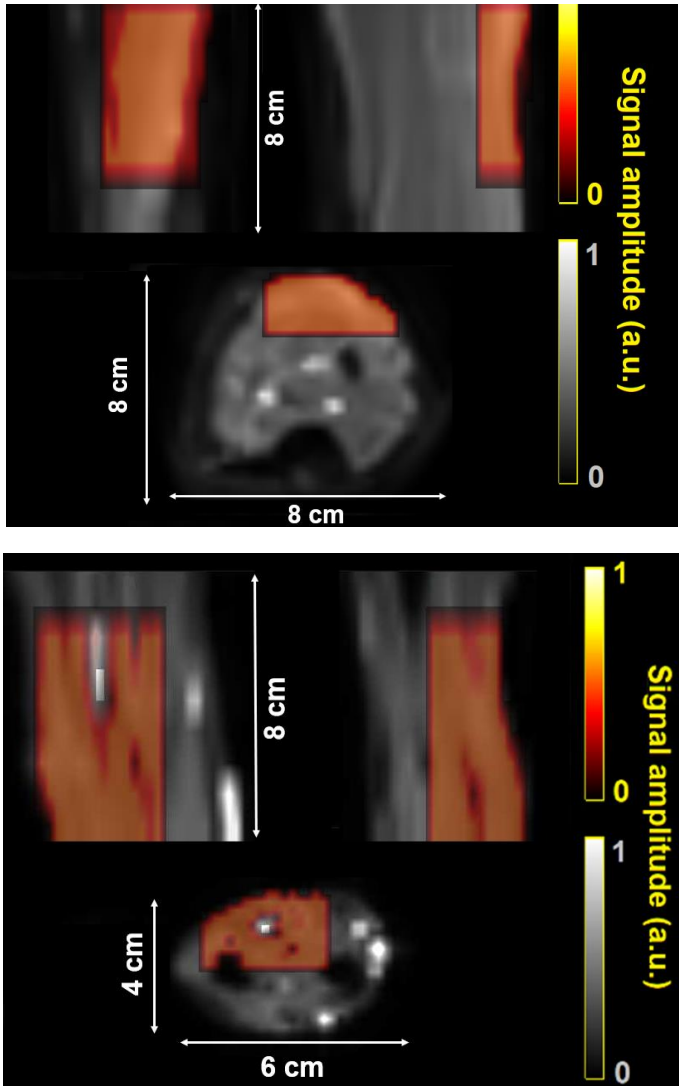


Figure 3.29 The DWI image of a volunteer's a) leg and b) forearm during the baseline. The highlighted area indicates the masks, used to calculate the IVIM-derived parameters. The black-white and colored bars represent the MR signal amplitudes of the entire tissue and the region of interest respectively. Arterial and venous vessels with active blood perfusion show greater signal attenuation and are displayed in dark gray. In contrast, the areas with restricted water molecular motion, such as bones and muscles, exhibit less MR signal attenuation and appear in light gray [30, 127]. Bright spots correspond to voxels occupied mostly by veins or arteries. These voxels were excluded from analayses. To improve image contrast, the MR signal from fat tissue (surrounding the muscles) was suppressed.

Figure 3.30 and 3.31 show the BFI_{DCS} and IVIM-derived parameters measured during baseline, 60 and 180 mmHg pressures. The leg and forearm occlusions were performed on five healthy adult volunteers. However, due to an equipment technical issue, the IVIM data acquired from one of the volunteer's forearm was not saved. Therefore, a total of five leg datasets and four forearm datasets were used for further analyses.

The occlusions resulted in a reduction of the mean values of BFI_{DCS} and D_{slow} measured during leg and forearm occlusions compared to baseline. However, this decrease compared to baseline reached statistical significance only for the BFI_{DCS} at 180 mmHg on leg occlusion and at both 60 and 180 mmHg for forearm occlusion. In contrast, the mean value of the D_{fast} and related standard deviation increased significantly in response to both 60 and 180 mmHg. The mean f increased in response to leg occlusions at 60 and 180 mmHg, with statistically significant difference only at 60 mmHg. For forearm occlusion, the mean f increased with statistical significance difference at 60 mmHg and remained at baseline levels at 180 mmHg. Since BF_{IVIM} is defined as the product of f and D_{fast}, its response to occlusions reflects the corresponding changes in these two parameters.

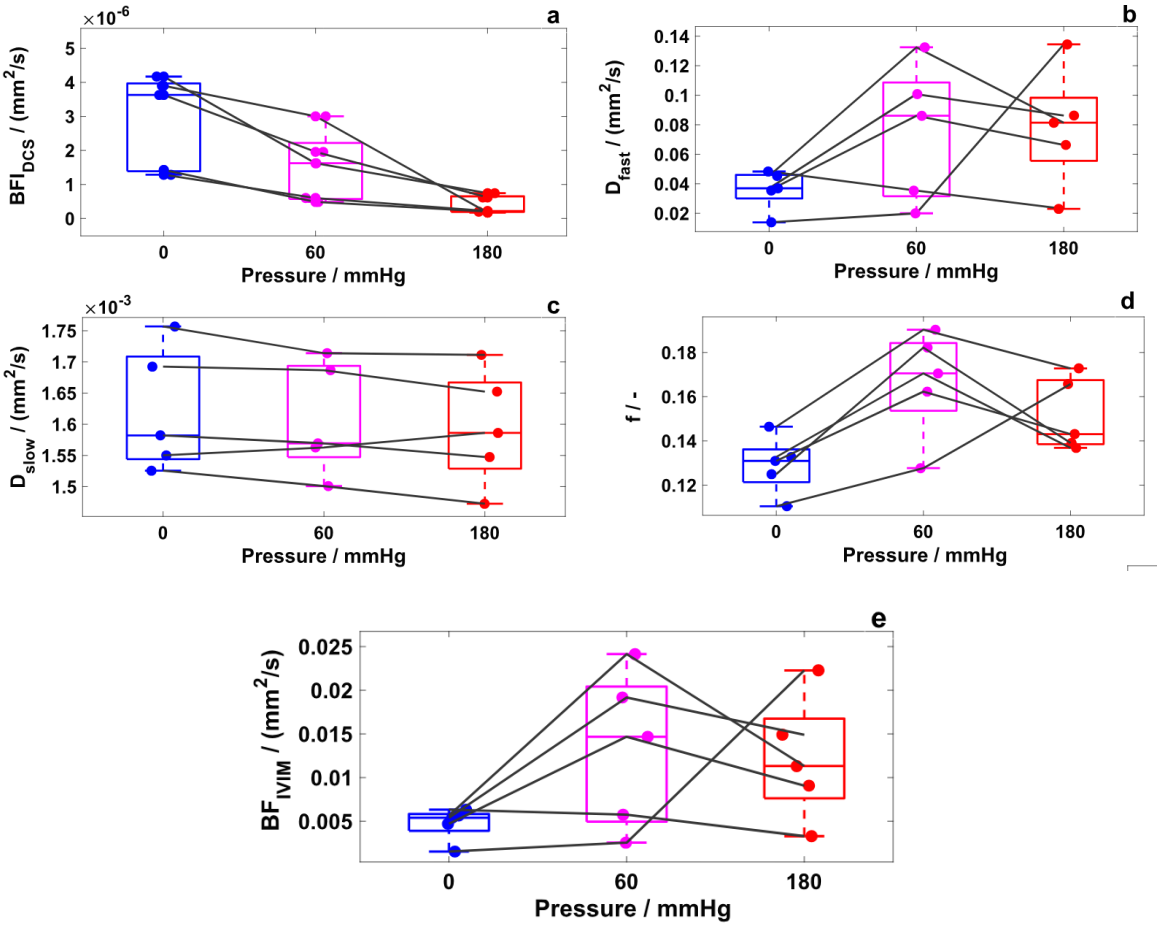


Figure 3.30 a) BFI_{DCS} (DCS-derived blood flow index), b) D_{fast} (IVIM-derived pseudo diffusion coefficient), c) D_{slow} (IVIM-derived diffusion coefficient), d) f (IVIM-derived perfusion fraction) and e) $BF_{IVIM} = f \cdot D_{fast}$ (IVIM-derived blood flow), during baseline, venous, and arterial occlusion measured on 5 healthy adult volunteers' leg. In each boxplot, the central line represents the median. The lower and upper edges indicate the 25th and 75th percentiles, respectively. The whiskers extend to the most extreme data points, not considering outliers.

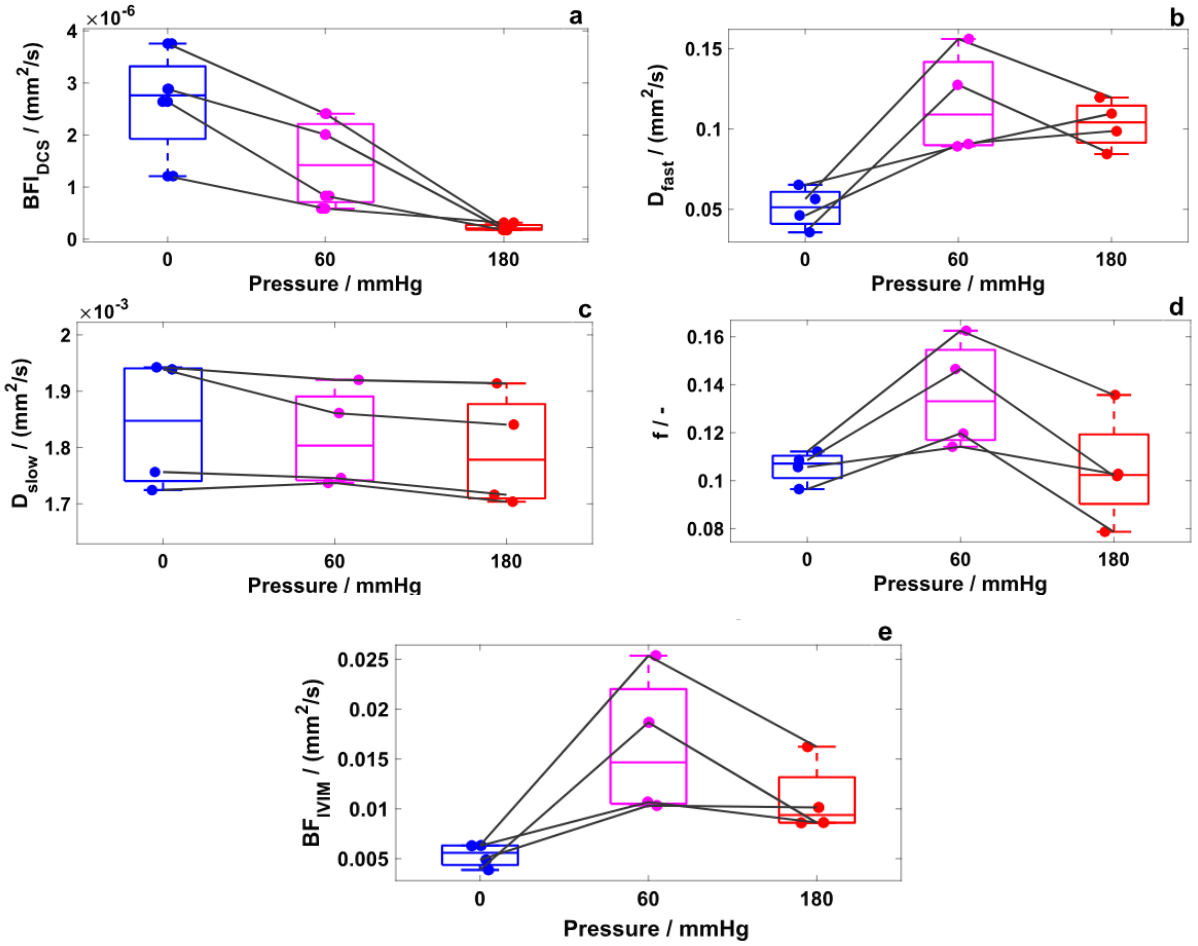


Figure 3.31 a) BFI_{DCS} (DCS-derived blood flow index), b) D_{fast} (IVIM-derived pseudo diffusion coefficient), c) D_{slow} (IVIM-derived diffusion coefficient), d) f (IVIM-derived perfusion fraction) and e) $BF_{IVIM} = f \cdot D_{fast}$ (IVIM-derived blood flow), during baseline, venous, and arterial occlusion measured on 4 healthy adult volunteers' forearm. In each boxplot, the central line represents the median. The lower and upper edges indicate the 25th and 75th percentiles, respectively. The whiskers extend to the most extreme data points, not considering outliers.

The results presented in this part have been discussed in detail and compared to other papers in next chapter.

4 Discussions and conclusions

4.1 Discussions

In the first part of this PhD thesis, the performance of td-DCS at various SDSs to recover the αD_b and BFI has been evaluated. The metrics to characterize and determine the optimal DTOF ranges to recover αD_b and BFI have been described in [89, 133]. Building on this, a combination of metrics based on the measurands of β and αD_b were presented for identifying optimal DTOF ranges in td-DCS technique to recover the αD_b and BFI (see figures 3.3 – 3.8). This optimization was critical to ensure reliable recovery of αD_b and BFI across different SDSs. According to these results and in line with other reports [35, 118], analysing the photons within the time range around DTOF peak improves the estimation of the αD_b and BFI comparing to other DTOF range.

In previous studies, time-gating strategies used fixed the gate start time and gate width across all subjects, despite the variations in individual tissue optical properties [19, 188]. The fixed temporal position of early gate as well as the fixed temporal position of late gates for all subjects, does not account for the inter-subject variability of optical properties. In contrast, the gating strategy proposed in this study, is based on adjusting the gates positions and gate widths individually for each considered medium (phantom or tissue). This gating approach is based on the DTOF parameters (e.g. FWHM) and considers key factors such as SDS and the optical properties (μ_a and μ'_s), ensuring a more adaptive and personalized data analysis strategy.

To successfully apply td-DCS at large SDSs, the increased laser power is necessary. To increase laser power while adhering the safe skin exposure [100], the illumination area was increased using a beam expander. To assess the impact of the beam expander, the $r\alpha D_b$ was calculated from the data obtained on homogeneous phantoms measured with and without the beam expander at the laser fiber's tip. No statistically significant difference was observed between the $r\alpha D_b$ values obtained from the early time gates at each SDS measured with and without beam expander. Similarly, no statistically significant difference was observed between the $r\alpha D_b$ values obtained from the late time gates at each SDS measured with and without beam expander (see figure 3.9). These findings confirm that beam expander enables measurements at large SDS without introducing noticeable bias in td-DCS-derived flow parameters

By analysis of the sensitivity metrics, I assessed the ability of td-DCS at shorter (1.5 cm) and larger (2 and 2.5 cm) SDSs to estimate the changes in αD_b of scatterers within the superficial and deep layers of two-layered phantom. Results of these analyses confirm that increasing SDS improves the sensitivity to recover the αD_b of the deeper layer and reduces the sensitivity to changes in αD_b of scatterers located in superficial layer (see figure 3.10 and 3.11). However, in the case of thick superficial layer (1.5 cm), even at larger SDS (2.5 cm), the td-DCS showed limited ability to detect the αD_b changes in deep layer as well as tp minimize the influence of high αD_b changes appearing in the superficial layer.

The performance of td-DCS at various SDSs to recover the rBFI has been evaluated in response to BH and HV respiratory challenges. The increase of rBFI in response to BH and decrease of rBFI in response to HV was observed at all SDSs (see figures 3.13 and 3.14). The same trend of rBFI during BH and HV has been reported by other authors using the cw-DCS technique [31, 119], interferometric DCS [189] and td-DCS [118]. Based on the result of respiratory challenges measured at three different SDSs, higher rBFI changes during BH was observed at larger SDS (2.5 cm) [190]. Moreover, the higher rBFI changes during HV can be observed at shorter SDS (1.5 cm) [189] (see figure 4.15). In phantom measurements it was noted that use of larger SDSs leads to increase of the sensitivity to flow changes appearing in the deeper layer. Therefore, these results might be due to the larger BFI changes in the intracerebral layer caused by the BH rather than HV. Similar trend was previously reported in [31].

Although td-DCS was successfully applied at large SDSs of 2.5 cm during phantom measurements and the forearm muscle occlusion test, there was limitation when applying it on the human head to detect cerebral blood flow changes. During the respiratory challenge measurements, data collected in two subjects (out of six subjects in total) at SDS = 2.5 cm showed significant noise and were therefore excluded from further averaging and analysis. So, the SDS of 2 cm was considered the optimal source detector separation for td-DCS to monitor CBF changes for further steps of my research.

In the next part of this research, the correlation of hemodynamic response measured by DCS modalities and BOLD-MRI were evaluated. To do that first the performance of cw-DCS and td-DCS in detecting αD_b changes within superficial and deeper layers of two-layered phantom were evaluated and compared. The two-layered phantom as simplified model of the human head helps to interpret the DCS signals measured from intracerebral and extracerebral layer of human head.

The $n\alpha D_b$ was calculated to evaluate each cw-DCS and td-DCS technique's sensitivity to monitor the αD_b of scatterers in superficial and deeper layers. The larger differences in $n\alpha D_b$ were observed between the early and late gates of td-DCS, compared to those derived from the two fitting strategies in cw-DCS, in which the whole and limited part of the g_1 curve were fitted. It suggested that in comparison to cw-DCS, td-DCS offers improved depth discrimination for assessing αD_b changes of superficial and deep layers.

Although the signal obtained at late gate in td-DCS is theoretically more sensitive to changes in αD_b of scatterers distributed in the deeper layer, the short coherence length of the pulsed laser used in this study limits the system's ability to effectively discriminate photons that travelled long path through the medium. As a result, the expected advantage of td-DCS in estimating the deep-layer αD_b change is diminished and this technique does not significantly outperform the cw-DCS method when fitting is limited to early lag time of g_1 ($g_1 > 0.7$). No significant improvements in the mean value and standard devetion of the $n\alpha D_b$ obtained from late gate in td-DCS and the $n\alpha D_b$ obtained using cw-DCS method when fitting is limited to early lag time of g_1 ($g_1 > 0.7$), supports this observation (see figure 3.17 b). Moreover, it has been reported that the IRF of the td-DCS system should not be wider than 200 ps (FWHM) [191]. The broad IRF of the developed td-DCS system (~560 ps) increases the probability of mixing of signals related to the photons arriving at early and late time of flight [37, 133]. This mixing leads to enhanced sensitivity of the signals measured in the early gate to changes in αD_b of scatterers located in the deeper layer and enhanced sensitivity of the signals measured in late gate to changes of αD_b of scatterers located in the superficial layer. Consequently, the td-DCS system developed in this study doesn't yet provide a substantial benefit over the cw-DCS technique because of the limited coherence length of the pulsed laser and wide IRF of the setup [57, 192].

According to results presented in this study, fitting the early portion of autocorrelation function ($g_1 > 0.7$) obtained from theory to the measured g_1 leads to improved sensitivity of cw-DCS to changes in αD_b appearing in deep layer of the tissue. However, it increased the standard deviation of the estimated αD_b and BFI. In other studies, an improved sensitivity to deep-layer hemodynamics changes was reported when multi-layer models, combined with multi-distance cw-DCS measurements were applied [34, 93]. Although this approach is effective, it significantly increases the system complexity and cost. Recent advances in td-DCS technology have led to systems equipped with superconducting nanowire single-photon detectors operating at 1064 nm, offering improved sensitivity to deeper layer hemodynamics'

changes and improvement in the signal-to-noise ratio [35, 118]. However, these systems are bulky and expensive compared to the optical system developed in this study, which provides portability mixed with cost-efficiency.

A critical factor influencing sensitivity of trDCS to intracerebral blood flow changes is the thickness of the extracerebral layer [193-195]. Due to the limited ability of the DCS techniques to distinguish the BFI changes in different layers, it is not feasible to precisely determine the contributions of intracerebral and extracerebral blood flow within the measured signals. In experiments carried out on two-layered phantoms with known optical properties and controlled αD_b changes, I estimated contributions related to each layer in the measured BFI changes. The average scalp and skull thickness among the subjects participated in simultaneous monitoring of hemodynamic response measured by DCS modalities and BOLD-MRI was approximately 1.2 cm. Considering this observation, I developed two-layered phantoms with superficial layer thicknesses of 1 cm and 1.5 cm which modeled the adult human head [106, 107]. Based on the calculated median of $n\alpha D_{\mathrm{b}}$ values (see Figure 3.17), and accounting for inter-subject variability in the skull and scalp thickness, the contribution of intracerebral to the overall BFI was approximately in the range between 5–30%. Moreover, the contribution of extracerebral blood flow to the overall BFI was approximately in the range 20–80%.

In order to assess the correlation between the hemodynamic response measured by DCS modalities and BOLD-MRI techniques in response to CBF and oxygenation-related changes, series of BH and HV respiratory challenges were performed in healthy adult volunteers. The BH caused an increase in both BFI and BOLD signals (see figure 3.19). During HV, the BOLD signal exhibited an initial slight increase, followed by a more sustained decrease [196] (see figure 3.20). This early increase in the signal was more pronounced in the BFIs recorded by DCS. This observation aligns with previous literature [189, 197, 198].

No statistically significant differences were found between the BFI changes calculated using two fitting scenarios in cw-DCS or from the early and late gate in td-DCS in response to BH and HV (see figure 3.21). Similarly, there is no statistically significant differences between the BOLD signal changes obtained from regions of interest located in the intracerebral and extracerebral layers of the head. This observation can be explained by the fact that BH and HV are systemic stimuli rather than regional or localized ones. These respiratory challenges induce physiological changes that affect the hemodynamic responses in both intracerebral and extracerebral layers [173, 174]. Therefore, an in-depth validation of the DCS techniques for evaluation of hemodynamic responses appearing in intra- and extracerebral layers need stimulation paradigms with less effects on the extracerebral layer.

An approximate 1–2% increase and 1.5–3% decrease in the BOLD signal in response to BH and HV, respectively (Figure 3.21) were observed. Correspondingly, the BFIs measured by DCS techniques increased by 20–50% during BH and decreased by 10–30% during HV. These findings align with previously reported studies evaluating the brain hemodynamics using BOLD-MRI and ASL-MRI in response to similar respiratory challenges. Such studies documented BOLD signal increase of 1–4% and the CBF increase of 30–70% following BH, as well as BOLD decrease of 1.5–4.7% and CBF reduction of 40-60% in response to HV [178, 199]. The relatively higher amplitudes of BOLD and CBF reported in other studies might be attributed to variations in the duration and method of execution of respiratory challenges. For instance, instructing subjects to perform BH after expiration for extended periods tends to elicit more immediate and pronounced increases in CBF. Similarly, prolonged deep breathing during HV can affect the magnitude of changes observed in both BOLD and CBF signals [196]. Additionally, the amplitude of BFI changes measured by DCS in this study may be underestimated, a limitation that also noted by Bartlett et al. [200]. Another reason that may potentially contribute to discrepancies between the results reported by other authors and changes in BOLD and BFI measured in this study is the limited sensitivity of DCS-measured signals to intracerebral blood flow changes, and strong influence of the extracerebral hemodynamics on the detected signals.

To evaluate the temporal relation between the BFI and BOLD signals, hysteresis loops of normalized BFI versus normalized BOLD signal changes were analyzed. During BH, the clockwise direction of the loops (see figure 3.22 a, b) indicates that BFI changes precede the BOLD signal. This phenomenon is consistent with the BH-induced vasodilation, which increases vascular diameter and blood inflow. The increased blood flow leads to delaying the subsequent oxygenation changes reflected in the BOLD signal [201]. The average delay between BFI and BOLD signals following BH was approximately 2.7 seconds (see figure 3.23 a-d). This delay was longer than delays reported between CBF measured by ASL-MRI and BOLD signals while performing similar respiratory stimuli [201, 202]. This discrepancy may arise because MRI-based CBF measurements are acquired directly from brain tissue voxels (e.g., gray and white matter), whereas DCS-derived BFIs signals are affected by extracerebral hemodynamics and individual anatomical variations such as scalp and skull thickness. Furthermore, it has been reported that BOLD signals originating from voxel full of micro vessels generally exhibit earlier responses compared to those dominated by macro vessels structures [203, 204]. Since DCS primarily estimates microvascular blood flow, the previously mentioned factors may contribute to the observed timing differences.

The hysteresis loops during HV (see figure 3.22 c, d) showed a counterclockwise direction, suggesting that BOLD signal changes precede those in BFI. The delay between these signals was approximately 0.2 seconds; substantially shorter than the delay observed during BH (see figure 3.23 e-h). This likely reflects the rapid reduction in blood carbon dioxide levels due to hyperventilation, which induces vasoconstriction, decrease of CBF, and reduction of oxygen delivery; thereby directly impacts the BOLD signal [115, 201]. The asymmetrical shape of the hysteresis loop and its location below the unity line reflects that the BOLD response returns to baseline faster than the corresponding BFI changes.

Positive Pearson correlations were observed between the BFI and BOLD signals during BH, indicating a robust coupling between the blood flow and oxygenation hemodynamics under hypercapnic conditions (see figure 3.24 a, b). A lower correlation between the temporal hemodynamic responses following the HV task was observed which is related to a faster return of the BOLD signal to baseline compared to BFI signal (see figure 3.24 c, d). The higher correlation between the BFI and BOLD signal observed during BH compared to HV is consistent with the hysteresis analysis, indicating a more stable coupling between blood flow and oxygenation level changes under hypercapnic conditions.

The $rCMRO_2$ changes were further analyzed in response to the respiratory challenges. $rCMRO_2$ increased by approximately 5% during BH and decreased by around 1% during HV, consistent with some prior studies [205, 206] (see figure 3.25). The high standard deviation can be seen in the calculated $rCMRO_2$. Some other investigations have reported unchanged [207, 208] or decreased [209, 210] $rCMRO_2$ during BH and increases during HV [206]. Consequently, considering the variability in reported $CMRO_2$ responses by different studies and the large standard deviation of this parameter calculated in this study, the estimated $CMRO_2$ changes should be interpreted with caution.

In this study, the BOLD calibration constant (M) was estimated to be 0.04, which is lower than values reported in other studies, approximately 0.079 [142] and 0.098 [211]. The estimation of M and $rCMRO_2$ are linked together, meaning that changes in $rCMRO_2$ affects the estimated M. Moreover miscalculation of M lead to error in estimation of $rCMRO_2$ [212]. As M is calculated before the estimation of $rCMRO_2$ (Equation 2.20), any possible changes in estimation of the later parameter is not considered. This limitation lead to inaccurate estimation of both M and $rCMRO_2$ [213].

The results of simultaneous hemodynamic response measured by DCS and BOLD-MRI techniques underscore the potential of DCS modalities for continuous monitoring of cerebral hemodynamic response and evaluating the neurovascular coupling effects. In particular, beside

cost efficiency and easy transportation of the equipment allowing for bedside monitoring, DCS offers better temporal resolution compared to MRI-based perfusion methods [214, 215].

The IVIM-derived pseudo-diffusion coefficient suffer from misestimation [12, 102]. Thus, in the last part of this study, I carried out series of tissue mimicking phantom measurements and muscle occlusion tests to evaluate the correlation between the IVIM-derived pseudo-diffusion coefficient and flow index measured by cw-DCS.

As expected, increasing the flow in the tubes of the tissue mimicking phantom leads to significant increase of the DCS-derived flow index (see figure 4.27 a). For the cerebral microvascular perfusion with IVIM-derived pseudo diffusion coefficient (D_{fast}) within the range of $\leq 0.02\ \mathrm{mm}^2/\mathrm{s}$ [216], the estimation of the D_{fast} is expected to be more reliable [155]. While for muscle capillaries with $D_{\mathrm{fast}} > 0.02\ \mathrm{mm}^2/\mathrm{s}$ [217], the error in the estimated D_{fast} (see figures 3.27 b) is increased. This is due to the fact that the signal estimated using single-exponential model (Equation 2.21) at high *b*-values not only indicate Brownian related diffusion motion of water molecules, but also perfusion-related motion of water molecules [218]. These results suggest that flow index measured by cw-DCS is more accurate at the higher blood flow compared to D_{fast}.

Although the IVIM-derived diffusion coefficient and perfusion fraction were not directly compared to the cw-DCS derived flow index and BFI, their accurate estimation is essential for reliable IVIM-derived pseudo-diffusion coefficient and flow quantification. Therefore, these parameters were also subjected to detailed data interpretation. Relatively constant IVIM-derived diffusion coefficient (D_{slow}) was observed while increasing F_{pump} in to the tubes of the tissue mimicking phantom (see figure 3.27 c). This result supports that D_{slow} originates from Brownian motion of water molecules [218, 219].

IVIM-derived perfusion fraction (f) refers to the volume of the perfusion in each voxel [186, 187]. The low f value when there is no flow, confirms the capability of the IVIM-MRI technique to distinguish the MR signal attenuation caused by diffusion and perfusion-related motion of water molecules (see figure 3.27 d). In all F_{pump}, the cross section of tissue mimicking phantom's tubes remained unchanged, leading to relatively constant f for all F_{pump} [218]. However, due to the lower accuracy of the IVIM technique in measuring the IVIM-derived parameters at higher flows, the f might be misestimated.

Here some limitations of the tissue mimicking phantom measurements are noted. The bigger inner diameter of tubes compared to the tissues' microcapillaries, leads to the absence of shear stress effects [220] in tubes. Moreover, the tubes were rigid in size, whereas tissue's

microcapillaries exhibit a compliance. In tissue the capillaries might be affected by blood pressure which may lead to additional perfusion related motion than what was observed in the rigid structure of tissue mimicking phantom. Additionally, the flow in tubes of the tissue mimicking phantom occurred only in one direction, while in vivo capillary networks are not linear in geometry. However, in DCS studies it has been reported that the single-direction of the flow in tubes of the tissue-mimicking phantom introduces only a small bias in results compared to a truly random orientation of microcapillaries in tissue [220].

To cross-evaluate the IVIM-derived perfusion and flow parameters and BFI_{DCS}, series of muscle occlusion tests were performed on the healthy adult volunteers' leg and forearm. The tissue blood perfusion is expected to decrease in response to the 60 and 180 mmHg occlusions [221, 222]. This decrease can be seen in BFI_{DCS} measured during leg and forearm occlusions (see figures 3.30 (a) and 3.31 (a)). In contrast, there was an increase in the mean value and standard deviation of the perfusion-related motion derived by IVIM, averaged over all subjects (see figures 3.30 (b) and 3.31 (b)). This is possibly related to decrease of the blood perfusion in response to occlusions and consequently increased error in estimation of the D_{fast} [105, 223]. It has been reported that, the D_{fast} parameter estimation is highly sensitive to signal to noise ratio (SNR) changes [102, 224], and is overestimated at low SNR [225].

The muscle occlusions led to decrease of D_{slow} (see figure 3.30 (c) and 3.31 (c)) which reflects the tissue's extravascular water molecules diffusion [150, 153]. This decrease was observed in measurements carried out on both leg and forearm and is in agreement with [226]. However, the observed decrease was not statistically significant. Although extravascular tissue influences the DCS signal, its contribution to the estimated BFI_{DCS} is minimal [166, 220]. Thus D_{slow} and BFI_{DCS} are considered independent, leading to no correlation between these parameters.

Parameter f represents the volume fraction of the blood flowing in the microcapillary network and is influenced by the size, density, and the spatial orientation of the microcapillaries [186, 187]. In response to 60 mm Hg pressure, venous occlusion is expected, leading to reduction the venous outflow while arterial inflow remains unchanged [227, 228]. Although this effect may depend on the diastolic blood pressure of the volunteers, it has been reported that venous occlusion at 60 mmHg pressure occurs in most adults [113, 229]. The venous occlusion is expected to lead to an increase of blood volume [230, 231] in both leg and forearm and consequently an increase in the mean value of the f. The f averaged over all subjects was significantly increased in response to occlusion carried out at 60 mm Hg pressure (see figure

3.30 d and 3.31 d). In response to 180 mmHg pressure, the complete arterial occlusion is typically assumed to occur [127, 232]. Many factors may affect the blood pressure [226], leading to inter-subject differences of the f parameter in response to 180 mmHg pressure. However, the differences between the averaged f over all subjects measured during baseline and 180 mmHg pressure was not statistically significant.

The IVIM model assumes that microvascular capillaries are randomly oriented within a voxel. In response to the venous occlusions and increased blood volume [230, 231], voxels are likely to contain larger vessels. In such cases, blood perfusion within the tissue microcapillaries network doesn't fulfill the IVIM model assumption that D_{fast} is originated from randomly oriented capillary network. In this condition the microvascular perfusion is attributed to the D_{slow} instead of D_{fast} leading to misestimation of f and D_{fast} [155, 225].

In IVIM-MRI, misestimation of D_{fast} referring to microvascular perfusion-related motion limits the clinical application of this technique [233]. This condition leads to necessity to use an additional technique for assessing the measured D_{fast}. Altough no corelation was found between the D_{fast} and BFI_{DCS} in response to muscle occlusion, the tissue mimicking phantom results showed a positive correlation ($r > 0.8$) between the D_{fast} and FI_{DCS} (see figure 3.28 a). Consequently, DCS can be considered as an additional technique to IVIM-MRI to assess the D_{fast}. The D_{fast} and BFI_{DCS} are measured based on mean square displacements of water molecoules and RBCs per time respectively expressed by mm^2/s [220, 234]. Moreover, both parameters are affected by the heart rate and the viscosity of the perfusing fluid which contains both water molecules and RBCs [104, 235].

The differences in the physical properties of RBCs and water molecules may limit direct comparison of D_{fast} and BFI_{DCS}. RBCs are much larger (≈ 7 μm) than water molecules ($\approx 10^{-4}$ μm) and have a deformable disk-like shape [236, 237], leading to the different shear stress within the microcapillaries [166, 238]. As a result, the DCS-derived diffusion coefficient of RBCs is significantly lower ($\approx 10^{-6}\ \text{mm}^2/\text{s}$) [166, 238] than the D_{fast} ($\approx 10^{-3}\ \text{mm}^2/\text{s}$) [103]. The tissues' microstructure can affect the measured D_{fast} and BFI_{DCS} parameters. D_{fast} depends on the random orientation of the capillary network in the considered voxel of tissue [150, 153]. While BFI_{DCS} depends on the spatial distribution of the tissue's micro vessels located under the optical probe on the volume between source and detector [166, 220]. Muscles with increased fat fraction can also affects both measured D_{fast} and BFI_{DCS}. In IVIM, increased fat fraction influences microvascular structure of tissues and microvascular perfusion. This leads to decrease in D_{fast} and misestimation of this parameter [217]. In DCS, increased fat

fraction leads to decreased the estimated μ_a and BFI, while increasing the estimated μ_s' of the tissue [25]. IVIM-MRI is very sensitive to the motion of organs related to respiratory movements [150, 153]. DCS is also affected by motion artifacts caused by vibrations of the MRI bed, which occurs due to the strong gradient pulses during the DWI scanning. Thus, experimental conditions can affect the measured D_{fast} and BFI_{DCS} and consequently lead to misestimation of these parameters.

The results of my investigations showed, no correlation between the D_{fast} and IVIM-derived blood flow ($BF_{\text{IVIM}} = f.D_{\text{fast}}$) with BFI_{DCS} during muscle occlusion test. The lack of correlation between the BF_{IVIM} and BFI_{DCS} is related to the large standard deviation of the estimated D_{fast}, which has also been reported in other studies in which IVIM was validated using other techniques [53, 225]. Thus, the misestimation of IVIM-MRI technique to quantify the microvascular perfusion may limits its clinical application.

4.2 Conclusions

Results of measurements carried out on two-layered phantom as well as estimations of muscle blood flow changes following muscle occlusion test and CBF changes during respiratory challenges show that an increase in SDS leads to improvement of the sensitivity of the signals measured by td-DCS to the changes of αD_{b} and BFI in deep layers of the tissues. These results show that the first hypothesis is true.

Positive correlation between the BFI changes measured by DCS techniques and the BOLD signals during respiratory challenges, confirm the potential of DCS techniques in monitoring cerebral hemodynamic responses specially for which the good temporal resolution is necessary. Moreover, DCS can be used as a complementary tool alongside BOLD-MRI technique to monitor the $CMRO_2$. A positive correlation was also found between the IVIM-derived microvascular perfusion-related motion and DCS-derived flow index measured in series of experiments carried out on tissue mimicking phantom. It was also confirmed in analysis of correlation of in-vivo measured DCS signals that IVIM-MRI suffers from high uncertainty in estimating blood perfusion-related parameters.

Results presented in this thesis show good correlation between the hemodynamic responses measured by DCS and MRI techniques. Thus, DCS can be considered as a non-invasive portable tool for bed side monitoring of microvascular blood flow changes. These findings provide proof for the second hypothesis.

The study carried out suggest that further improvements in data analysis approach as well as in instrumentation for DCS are necessary in order to make this technique more practically useful in clinical applications.

References

1 de Lima EP, Tanaka M, Lamas CB, Quesada K, Detregiachi CRP, Araújo AC *et al*. Vascular Impairment, Muscle Atrophy, and Cognitive Decline: Critical Age-Related Conditions. *Biomedicines* 2024; 12.

2 McCully KK, Posner JD. The application of blood flow measurements to the study of aging muscle. *J Gerontol A Biol Sci Med Sci* 1995; 50 Spec No: 130-136.

3 Ghirardini F, Martini R. Current Opinion on Diagnosis of Peripheral Artery Disease in Diabetic Patients. *Medicina (Kaunas)* 2024; 60.

4 Aguirre GK, Zarahn E, D'Esposito M. The Variability of Human, BOLD Hemodynamic Responses. *NeuroImage* 1998; 8: 360-369.

5 Zauner A, Daugherty WP, Bullock MR, Warner DS. Brain Oxygenation and Energy Metabolism: Part I—Biological Function and Pathophysiology. *Neurosurgery* 2002; 51: 289-302.

6 Buckley EM. Diffuse correlation spectroscopy for measurement of cerebral blood flow: future prospects. In: Parthasarathy AB (ed), vol. 1(1). PubMed: Neurophotonics, 2014, pp 1-7.

7 Xiong L, Liu X, Shang T, Smielewski P, Donnelly J, Guo ZN *et al*. Impaired cerebral autoregulation: measurement and application to stroke. *J Neurol Neurosurg Psychiatry* 2017; 88: 520-531.

8 ter Laan M, van Dijk JMC, Elting JWJ, Staal MJ, Absalom AR. Sympathetic regulation of cerebral blood flow in humans: a review. *BJA: British Journal of Anaesthesia* 2013; 111: 361-367.

9 Purkayastha S, Sorond F. Transcranial Doppler ultrasound: technique and application. *Seminars in neurology* 2012; 32: 411-420.

10 Sturgess J, Matta B. Chapter 46 - Transcranial Doppler Ultrasonography and Other Measures of Cerebral Blood Flow. In: Gupta AK, Gelb AW (eds). *Essentials of Neuroanesthesia and Neurointensive Care*. W.B. Saunders: Philadelphia, 2008, pp 296-300.

11 Al-Sharify ZT, Al-Sharify TA, Al-Sharify NT, Yahya naser H. A critical review on medical imaging techniques (CT and PET scans) in the medical field. *IOP Conference Series: Materials Science and Engineering* 2020; 870: 012043.

12 Liao Y-P, Urayama S-i, Isa T, Fukuyama H. Optimal Model Mapping for Intravoxel Incoherent Motion MRI. *Frontiers in Human Neuroscience* (Original Research) 2021; Volume 15 - 2021.

13 Yang L, Wu X, Wang Y, Shi G, Hu H, Duan X. Comparison of image quality and quantitative parameters in intravoxel incoherent motion imaging at 3-T based on turbo spin-echo and echo-planar imaging in patients with oral cancer. *Diagn Interv Radiol* 2023; 29: 786-793.

14 Sordillo LA, Pu Y, Pratavieira S, Budansky Y, Alfano RR. Deep optical imaging of tissue using the second and third near-infrared spectral windows. *J Biomed Opt* 2014; 19: 056004.

15 Jobsis-vander Vliet F, Joebsis P. Biochemical and physiological basis of medical near-infrared spectroscopy. *Journal of Biomedical Optics* 1999; 4.

16 Dehghani H, Eames ME, Yalavarthy PK, Davis SC, Srinivasan S, Carpenter CM *et al*. Near infrared optical tomography using NIRFAST: Algorithm for numerical model and image reconstruction. *Communications in Numerical Methods in Engineering* 2009; 25: 711-732.

17 Benaron DA, Benitz WE, Ariagno RL, Stevenson DK. Noninvasive Methods for Estimating In Vivo Oxygenation. *Clinical Pediatrics* 1992; 31: 258-273.

18 Habazettl H, Athanasopoulos D, Kuebler WM, Wagner H, Roussos C, Wagner PD *et al*. Near-infrared spectroscopy and indocyanine green derived blood flow index for noninvasive measurement of muscle perfusion during exercise. *Journal of Applied Physiology* 2010; 108: 962-967.

19 Ozana N, Lue N, Renna M, Robinson MB, Martin A, Zavriyev AI *et al*. Functional Time Domain Diffuse Correlation Spectroscopy. *Front Neurosci* 2022; 16: 932119.

20 Boas DA, Dunn AK. Laser speckle contrast imaging in biomedical optics. *J Biomed Opt* 2010; 15: 011109.

21 Pi S, Li Y, Lin C, Li G, Wen H, Peng H *et al*. Arterial spin labeling and diffusion-weighted MR imaging: quantitative assessment of renal pathological injury in chronic kidney disease. *Abdom Radiol (NY)* 2023; 48: 999-1010.

22 Espes D, Manell E, Rydén A, Carlbom L, Weis J, Jensen-Waern M *et al*. Pancreatic perfusion and its response to glucose as measured by simultaneous PET/MRI. *Acta Diabetol* 2019; 56: 1113-1120.

23 Durduran T. Diffuse correlation spectroscopy for non-invasive, micro-vascular cerebral blood flow measurement2014; 85: 51-63.

24 Bartlett MF, Akins JD, Oneglia AP, Brothers RM, Wilkes D, Nelson MD. Impact of cutaneous blood flow on NIR-DCS measures of skeletal muscle blood flow index. *J Appl Physiol (1985)* 2021; 131: 914-926.

25 Gómez C, Roblyer D. Effects of skin tone and adipose thickness on frequency domain near-infrared spectroscopy and diffuse correlation spectroscopy. *Biophotonics Discovery* 2024; 2: 012503.

26 Rolf BS, Andrew JB. Measurement of layer-like hemodynamic trends in scalp and cortex: implications for physiological baseline suppression in functional near-infrared spectroscopy. *Journal of Biomedical Optics* 2008; 13: 034017.

27 Gagnon L, Desjardins M, Jehanne-Lacasse J, Bherer L, Lesage F. Investigation of diffuse correlation spectroscopy in multi-layered media including the human head. *Opt Express* 2008; 16: 15514-15530.

28 Durduran T, Yu G, Burnett MG, Detre JA, Greenberg JH, Wang J *et al*. Diffuse optical measurement of blood flow, blood oxygenation, and metabolism in a human brain during sensorimotor cortex activation. *Opt Lett* 2004; 29: 1766-1768.

29 Sutin JDB, Zimmerman B, Tyulmankov D, Tamborini D, Wu K-C, Selb J *et al*. Time-domain diffuse correlation spectroscopy. *Optica* 2016; 3 9: 1006-1013.

30 Yu G, Durduran T, Lech G, Zhou C, Chance B, Mohler E *et al*. Time-dependent blood flow and oxygenation in human skeletal muscles measured with noninvasive near-infrared diffuse optical spectroscopies. *Journal of Biomedical Optics* 2005; 10: 024027.

31 Mesquita RC, Schenkel SS, Minkoff DL, Lu X, Favilla CG, Vora PM *et al*. Influence of probe pressure on the diffuse correlation spectroscopy blood flow signal: extra-cerebral contributions. *Biomedical Optics Express* 2013; 4.

32 Buckley EM, Hance D, Pawlowski T, Lynch J, Wilson FB, Mesquita RC *et al*. Validation of diffuse correlation spectroscopic measurement of cerebral blood flow using phase-encoded velocity mapping magnetic resonance imaging. *J Biomed Opt* 2012; 17: 037007.

33 Wu MM, Chan ST, Mazumder D, Tamborini D, Stephens KA, Deng B *et al*. Improved accuracy of cerebral blood flow quantification in the presence of systemic physiology cross-talk using multi-layer Monte Carlo modeling. *Neurophotonics* 2021; 8: 015001.

34 Carp SA, Boas DA, Sajjadi AY, Selb J. Recovery of brain blood flow changes from diffuse correlation spectroscopy data using a layered Monte Carlo forward model. *Biomedical Optics 2014*, 2014.

35 Parfentyeva V, Colombo L, Lanka P, Pagliazzi M, Brodu A, Noordzij N *et al*. Fast time-domain diffuse correlation spectroscopy with superconducting nanowire single-photon detector: system validation and in vivo results. *Sci Rep* 2023; 13: 11982.

36 Colombo L, Pagliazzi M, Sekar SKV, Contini D, Mora AD, Spinelli L *et al*. Effects of the instrument response function and the gate width in time-domain diffuse correlation spectroscopy: model and validations. *Neurophotonics* 2019; 6: 035001.

37 Cheng X, Tamborini D, Carp SA, Shatrovoy O, Zimmerman B, Tyulmankov D *et al*. Time domain diffuse correlation spectroscopy: modeling the effects of laser coherence length and instrument response function. *Opt Lett* 2018; 43: 2756-2759.

38 Mogharari N, Samaei S, Wojtkiewicz S, Liebert A, Kacprzak M. Time-domain diffuse correlation spectroscopy performance at different source-detector separation. *Diffuse Optical Spectroscopy and Imaging IX*. Optica Publishing Group: Munich, 2023, p 1262816.

39 Mogharari N, Wojtkiewicz S, Borycki D, Liebert A, Kacprzak M. Time-domain diffuse correlation spectroscopy at large source detector separation for cerebral blood flow recovery. *Biomedical Optics Express* 2024; 15: 4330-4344.

40 Yu G, Durduran T, Zhou C, Wang H-W, Putt ME, Saunders HM *et al*. Noninvasive Monitoring of Murine Tumor Blood Flow During and After Photodynamic Therapy Provides Early Assessment of Therapeutic Efficacy. *Clinical Cancer Research* 2005; 11: 3543-3552.

41 Culver JP, Durduran T, Furuya D, Cheung C, Greenberg JH, Yodh AG. Diffuse optical tomography of cerebral blood flow, oxygenation, and metabolism in rat during focal ischemia. *Journal of cerebral blood flow and metabolism : official journal of the International Society of Cerebral Blood Flow and Metabolism* 2003; 23: 911-924.

42 Kim MN, Durduran T, Frangos S, Edlow BL, Buckley EM, Moss HE *et al*. Noninvasive measurement of cerebral blood flow and blood oxygenation using near-infrared and diffuse correlation spectroscopies in critically brain-injured adults. *Neurocrit Care* 2010; 12: 173-180.

43 Blanco I, Zirak P, Dragojevic T, Castellvi C, Durduran T, Justicia C. Longitudinal, transcranial measurement of functional activation in the rat brain by diffuse correlation spectroscopy. *Neurophotonics* 2017; 4: 045006.

44 Yu G, Floyd TF, Durduran T, Zhou C, Wang J, Detre JA *et al*. Validation of diffuse correlation spectroscopy for muscle blood flow with concurrent arterial spin labeled perfusion MRI. *Opt Express* 2007; 15: 1064-1075.

45 Carp SA, Dai GP, Boas DA, Franceschini MA, Kim YR. Validation of diffuse correlation spectroscopy measurements of rodent cerebral blood flow with simultaneous arterial spin labeling MRI; towards MRI-optical continuous cerebral metabolic monitoring. *Biomed Opt Express* 2010; 1: 553-565.

46 Shoemaker LN, Samaei S, Deller G, Wang DJJ, Milej D, St Lawrence K. All-optics technique for monitoring absolute cerebral blood flow: validation against magnetic resonance imaging perfusion. *Neurophotonics* 2024; 11: 045002.

47 Tagliabue S, Kacprzak M, Rey-Perez A, Baena J, Riveiro M, Maruccia F *et al*. How the heterogeneity of the severely injured brain affects hybrid diffuse optical signals: case examples and guidelines. *Neurophotonics* 2024; 11: 045005.

48 Tagliabue S, Lindner C, da Prat IC, Sanchez-Guerrero A, Serra I, Kacprzak M *et al*. Comparison of cerebral metabolic rate of oxygen, blood flow, and bispectral index under general anesthesia. *Neurophotonics* 2023; 10: 015006.

49 Ogawa S, Tank DW, Menon R, Ellermann JM, Kim SG, Merkle H *et al*. Intrinsic signal changes accompanying sensory stimulation: functional brain mapping with magnetic resonance imaging. *Proceedings of the National Academy of Sciences of the United States of America* 1992; 89: 5951-5955.

50 Ogawa S, Lee TM, Kay AR, Tank DW. Brain magnetic resonance imaging with contrast dependent on blood oxygenation. *Proceedings of the National Academy of Sciences of the United States of America* 1990; 87: 9868-9872.

51 Leontiev O, Buracas GT, Liang C, Ances BM, Perthen JE, Shmuel A *et al*. Coupling of cerebral blood flow and oxygen metabolism is conserved for chromatic and luminance stimuli in human visual cortex. *NeuroImage* 2013; 68: 221-228.

52 Griffeth VEM, Perthen JE, Buxton RB. Prospects for quantitative fMRI: Investigating the effects of caffeine on baseline oxygen metabolism and the response to a visual stimulus in humans. *NeuroImage* 2011; 57: 809-816.

53 Zabel WJ, Contreras-Sánchez H, Foltz W, Flueraru C, Taylor E, Vitkin A. Quantifying tumour microvasculature with optical coherence angiography and intravoxel incoherent motion diffusion MRI. *IEEE Transactions on Medical Imaging* 2025: 1-1.

54 Chung SH, Yu H, Su MY, Cerussi AE, Tromberg BJ. Molecular imaging of water binding state and diffusion in breast cancer using diffuse optical spectroscopy and diffusion weighted MRI. *J Biomed Opt* 2012; 17: 071304.

55 Hsiang D, Shah N, Yu H, Su MY, Cerussi A, Butler J *et al*. Coregistration of dynamic contrast enhanced MRI and broadband diffuse optical spectroscopy for characterizing breast cancer. *Technol Cancer Res Treat* 2005; 4: 549-558.

56 Helton M, Rajasekhar S, Zerafa S, Vishwanath K, Mycek MA. Numerical approach to quantify depth-dependent blood flow changes in real-time using the diffusion equation with continuous-wave and time-domain diffuse correlation spectroscopy. *Biomed Opt Express* 2023; 14: 367-384.

57 Huang W, Hu Y, Zhang T, Li J. Comparison between time domain and continuous wave diffuse correlation spectroscopy at 830 nm on functional detection of human brain by a simulation approach. *Optics & Laser Technology* 2024; 177.

58 Haskell RC, Svaasand LO, Tsay T-T, Feng T-C, McAdams MS, Tromberg BJ. Boundary conditions for the diffusion equation in radiative transfer. *J Opt Soc Am A* 1994; 11: 2727-2741.

59 Patterson MS, Madsen SJ, Moulton JD, Wilson BC. Diffusion equation representation of photon migration in tissue. *1991 IEEE MTT-S International Microwave Symposium Digest*, 1991, pp 905-908 vol.902.

60 Bigio IJ, Fantini S. *Quantitative Biomedical Optics: Theory, Methods, and Applications*. Cambridge University Press: Cambridge, 2016.

61 Boas DA. Diffuse photon probes of structural and dynamical properties of turbid media: theory and biomedical applications, University of Pennsylvania, 1996.

62 Kienle A, Patterson MS. Improved solutions of the steady-state and the time-resolved diffusion equations for reflectance from a semi-infinite turbid medium. *J Opt Soc Am A* 1997; 14: 246-254.

63 Arridge SR. Optical tomography in medical imaging. *Inverse Problems* 1999; 15: R41.

64 Rupawala M, Dehghani H, Lucas SJE, Tino P, Cruse D. Shining a Light on Awareness: A Review of Functional Near-Infrared Spectroscopy for Prolonged Disorders of Consciousness. *Frontiers in Neurology* (Review) 2018; Volume 9 - 2018.

65 Patterson MS, Chance B, Wilson BC. Time resolved reflectance and transmittance for the non-invasive measurement of tissue optical properties. *Applied optics* 1989; 28: 2331-2336.

66 Arridge SR, Cope M, Delpy DT. The theoretical basis for the determination of optical pathlengths in tissue: temporal and frequency analysis. *Physics in medicine and biology* 1992; 37: 1531-1560.

67 Bolt RA, Rinzema KR, Bosch JJt. Path-length distributions of photons re-emitted from turbid media illuminated by a pencil-beam. *Pure and Applied Optics: Journal of the European Optical Society Part A* 1995; 4: 123.

68 Inc TM. MATLAB version: 9.13.0 (R2022b), vol. 2022, 2022.

69 Patterson MS, Chance B, Wilson BC. Time resolved reflectance and transmittance for the noninvasive measurement of tissue optical properties. *Appl Opt* 1989; 28: 2331-2336.

70 Liebert A, Wabnitz H, Grosenick D, Möller M, Macdonald R, Rinneberg H. Evaluation of optical properties of highly scattering media by moments of distributions of times of flight of photons. *Appl Opt* 2003; 42: 5785-5792.

71 Boas DA, Gaudette T, Strangman G, Cheng X, Marota JJ, Mandeville JB. The accuracy of near infrared spectroscopy and imaging during focal changes in cerebral hemodynamics. *Neuroimage* 2001; 13: 76-90.

72 Torricelli A, Contini D, Pifferi A, Caffini M, Re R, Zucchelli L *et al*. Time domain functional NIRS imaging for human brain mapping. *Neuroimage* 2014; 85 Pt 1: 28-50.

73 Biswas A, Moka S, Muller A, Parthasarathy AB. Fast diffuse correlation spectroscopy with a low-cost, fiber-less embedded diode laser. *Biomed Opt Express* 2021; 12: 6686-6700.

74 Shapiro B. Large Intensity Fluctuations for Wave Propagation in Random Media. *Physical Review Letters* 1986; 57: 2168-2171.

75 Colombo L, Samaei S, Lanka P, Ancora D, Pagliazzi M, Durduran T *et al*. Coherent fluctuations in time-domain diffuse optics. *APL Photonics* 2020; 5.

76 Boas DA, Yodh AG. Spatially varying dynamical properties of turbid media probed with diffusing temporal light correlation. *J Opt Soc Am A* 1997; 14: 192-215.

77 Lemieux PA, Durian DJ. Investigating non-Gaussian scattering processes by using nth-order intensity correlation functions. *J Opt Soc Am A* 1999; 16: 1651-1664.

78 Liu B, Postnov D, Boas DA, Cheng X. Dynamic light scattering and laser speckle contrast imaging of the brain: theory of the spatial and temporal statistics of speckle pattern evolution. *Biomedical Optics Express* 2024; 15: 579-593.

79 Wu MM, Perdue K, Chan ST, Stephens KA, Deng B, Franceschini MA *et al*. Complete head cerebral sensitivity mapping for diffuse correlation spectroscopy using subject-specific magnetic resonance imaging models. *Biomed Opt Express* 2022; 13: 1131-1151.

80 Robinson MB, Renna M, Otic N, Kierul OS, Muldoon A, Franceschini MA *et al*. Pathlength-selective, interferometric diffuse correlation spectroscopy. *bioRxiv* 2025.

81 Li J, Dietsche G, Iftime D, Skipetrov S, Maret G, Elbert T *et al*. Noninvasive detection of functional brain activity with near-infrared diffusing-wave spectroscopy. *Journal of Biomedical Optics* 2005; 10: 044002.

82 Zhou C. In-vivo optical imaging and spectroscopy of cerebral hemodynamics, 2007.

83 Durduran T, Choe R, Baker WB, Yodh AG. Diffuse Optics for Tissue Monitoring and Tomography. *Rep Prog Phys* 2010; 73.

84 Irwin D, Dong L, Shang Y, Cheng R, Kudrimoti M, Stevens SD *et al*. Influences of tissue absorption and scattering on diffuse correlation spectroscopy blood flow measurements. *Biomed Opt Express* 2011; 2: 1969-1985.

85 Wax A, Backman V, Verdecchia K, Diop M, St. Lawrence K. Investigation of the best model to characterize diffuse correlation spectroscopy measurements acquired directly on the brain. *Biomedical Applications of Light Scattering IX*, 2015.

86 Carp S, Tamborini D, Mazumder D, Wu KC, Robinson M, Stephens K *et al*. Diffuse correlation spectroscopy measurements of blood flow using 1064 nm light. *J Biomed Opt* 2020; 25.

87 Samaei S, Sawosz P, Kacprzak M, Pastuszak Z, Borycki D, Liebert A. Time-domain diffuse correlation spectroscopy (TD-DCS) for noninvasive, depth-dependent blood flow quantification in human tissue in vivo. *Sci Rep* 2021; 11: 1817.

88 Siegert AJF. *On the fluctuations in signals returned by many independently moving scatterers*. Radiation Laboratory, Massachusetts Institute of Technology [Cambridge, Mass.]: [Cambridge, Mass.], 1943.

89 Samaei S, Colombo L, Borycki D, Pagliazzi M, Durduran T, Sawosz P *et al*. Performance assessment of laser sources for time-domain diffuse correlation spectroscopy. *Biomed Opt Express* 2021; 12: 5351-5367.

90 Pagliazzi M, Sekar SKV, Di Sieno L, Colombo L, Durduran T, Contini D *et al*. In vivo time-gated diffuse correlation spectroscopy at quasi-null source-detector separation. *Opt Lett* 2018; 43: 2450-2453.

91 Colombo L, Pagliazzi M, Konugolu Venkata Sekar S, Contini D, Durduran T, Pifferi A. In vivo time-domain diffuse correlation spectroscopy above the water absorption peak. *Opt Lett* 2020; 45: 3377-3380.

92 Galvan-Miyoshi J, Delgado J, Castillo R. Diffusing wave spectroscopy in Maxwellian fluids. *The European Physical Journal E* 2008; 26: 369-377.

93 Farzam P, Durduran T. Multidistance diffuse correlation spectroscopy for simultaneous estimation of blood flow index and optical properties. *J Biomed Opt* 2015; 20: 55001.

94 Tamborini D, Farzam P, Zimmermann B, Wu KC, Boas DA, Franceschini MA. Development and characterization of a multidistance and multiwavelength diffuse correlation spectroscopy system. *Neurophotonics* 2018; 5: 011015.

95 Tamborini D, Stephens KA, Wu MM, Farzam P, Siegel AM, Shatrovoy O *et al*. Portable System for Time-Domain Diffuse Correlation Spectroscopy. *IEEE Trans Biomed Eng* 2019; 66: 3014-3025.

96 Stabilized Compact Red CrystaLaser.

97 PDM Series, Single Photon Avalanche Diodes.

98 Becker W. Advanced Time-Correlated Single Photon Counting Applications, 2005.

99 Pirovano I, Re R, Candeo A, Contini D, Torricelli A, Spinelli L. Instrument response function acquisition in reflectance geometry for time-resolved diffuse optical measurements. *Biomed Opt Express* 2020; 11: 240-250.

100 Institute ANS. *American National Standard for Safe Use of Lasers in Health Care*. Laser Institute of America, 2018.

101 Selb J, Wu KC, Sutin J, Lin PI, Farzam P, Bechek S *et al*. Prolonged monitoring of cerebral blood flow and autoregulation with diffuse correlation spectroscopy in neurocritical care patients. *Neurophotonics* 2018; 5: 045005.

102 Lipiński K, Bogorodzki P. Evaluation of Whole Brain Intravoxel Incoherent Motion (IVIM) Imaging. *Diagnostics* 2024; 14: 653.

103 Le Bihan D, Breton E, Lallemand D, Grenier P, Cabanis E, Laval-Jeantet M. MR imaging of intravoxel incoherent motions: application to diffusion and perfusion in neurologic disorders. *Radiology* 1986; 161: 401-407.

104 Le Bihan D. What can we see with IVIM MRI? *NeuroImage* 2019; 187: 56-67.

105 Paganelli C, Zampini MA, Morelli L, Buizza G, Fontana G, Anemoni L *et al*. Optimizing b-values schemes for diffusion MRI of the brain with segmented Intravoxel Incoherent Motion (IVIM) model. *Journal of Applied Clinical Medical Physics* 2023; 24: e13986.

106 Strangman GE, Zhang Q, Li Z. Scalp and skull influence on near infrared photon propagation in the Colin27 brain template. *Neuroimage* 2014; 85 Pt 1: 136-149.

107 Doulgerakis M, Eggebrecht A, Wojtkiewicz S, Culver J, Dehghani H. Toward real-time diffuse optical tomography: accelerating light propagation modeling employing parallel computing on GPU and CPU. *J Biomed Opt* 2017; 22: 1-11.

108 Skouroliakou M, Kountouri AM, Hatziantoniou S, Koutri K, Chiou A. Physicochemical stability assessment of all-in-one parenteral emulsion for neonates containing SMOFlipid. *European Journal of Hospital Pharmacy: Science and Practice* 2012; 19: 514-518.

109 Sudakou A, Wabnitz H, Liemert A, Wolf M, Liebert A. Two-layered blood-lipid phantom and method to determine absorption and oxygenation employing changes in moments of DTOFs. *Biomedical Optics Express* 2023; 14.

110 Cortese L, Presti GL, Pagliazzi M, Contini D, Mora AD, Pifferi A *et al*. Liquid phantoms for near-infrared and diffuse correlation spectroscopies with tunable optical and dynamic properties. *Biomed Opt Express* 2018; 9: 2068-2080.

111 Vlachopoulos C, O'Rourke, M., & Nichols, W.W. *McDonald's Blood Flow in Arteries: Theoretical, Experimental and Clinical Principles*, 2011.

112 Shthialingam E. Hematocrit significantly confounds diffuse correlation spectroscopy measurements of blood flow. *Biomedical Optics Express* 2020; 11(8/1): 4786-4799.

113 Wilkinson IB, Webb DJ. Venous occlusion plethysmography in cardiovascular research: methodology and clinical applications. *Br J Clin Pharmacol* 2001; 52: 631-646.

114 Langham MC, Floyd TF, Mohler ER, 3rd, Magland JF, Wehrli FW. Evaluation of cuff-induced ischemia in the lower extremity by magnetic resonance oximetry. *J Am Coll Cardiol* 2010; 55: 598-606.

115 Godoy DA, Seifi A, Garza D, Lubillo-Montenegro S, Murillo-Cabezas F. Hyperventilation Therapy for Control of Posttraumatic Intracranial Hypertension. *Front Neurol* 2017; 8: 250.

116 Brandi G, Stocchetti N, Pagnamenta A, Stretti F, Steiger P, Klinzing S. Cerebral metabolism is not affected by moderate hyperventilation in patients with traumatic brain injury. *Crit Care* 2019; 23: 45.

117 Stocchetti N, Maas AI, Chieregato A, van der Plas AA. Hyperventilation in head injury: a review. *Chest* 2005; 127: 1812-1827.

118 Ozana N, Lue N, Renna M, Robinson MB, Martin A, Zavriyev AI *et al*. Functional Time Domain Diffuse Correlation Spectroscopy. *Frontiers in Neuroscience* (Original Research) 2022; 16.

119 Ozana N, Zavriyev AI, Mazumder D, Robinson M, Kaya K, Blackwell M *et al*. Superconducting nanowire single-photon sensing of cerebral blood flow. *Neurophotonics* 2021; 8.

120 MacIntosh BJ, Klassen LM, Menon RS. Transient hemodynamics during a breath hold challenge in a two part functional imaging study with simultaneous near-infrared spectroscopy in adult humans. *Neuroimage* 2003; 20: 1246-1252.

121 Durduran T. Diffuse correlation spectroscopy for non-invasive, micro-vascular cerebral blood flow measurement2014; 85: 51-63.

122

122 Delahoche J, Delapille P, Lemaître F, Verin E, Tourny-Chollet C. Arterial oxygen saturation and heart rate variation during breath-holding: comparison between breath-hold divers and controls. *Int J Sports Med* 2005; 26: 177-181.

123 Hawkins SM, Guensch DP, Friedrich MG, Vinco G, Nadeshalingham G, White M *et al*. Hyperventilation-induced heart rate response as a potential marker for cardiovascular disease. *Scientific Reports* 2019; 9: 17887.

124 Jha RK, Acharya A, Nepal O. Autonomic Influence on Heart Rate for Deep Breathing and Valsalva Maneuver in Healthy Subjects. *JNMA J Nepal Med Assoc* 2018; 56: 670-673.

125 Weckesser M, Posse S, Olthoff U, Kemna L, Dager S, M�ller-G�rtner HW. Functional imaging of the visual cortex with bold-contrast MRI: Hyperventilation decreases signal response. *Magnetic resonance in medicine* 1999; 41: 213-216.

126 Thomason ME, Burrows BE, Gabrieli JD, Glover GH. Breath holding reveals differences in fMRI BOLD signal in children and adults. *Neuroimage* 2005; 25: 824-837.

127 Li Z, Baker WB, Parthasarathy AB, Ko TS, Wang D, Schenkel S *et al*. Calibration of diffuse correlation spectroscopy blood flow index with venous-occlusion diffuse optical spectroscopy in skeletal muscle. *J Biomed Opt* 2015; 20: 125005.

128 Liu H, Chance B, Hielscher AH, Jacques SL, Tittel FK. Influence of blood vessels on the measurement of hemoglobin oxygenation as determined by time-resolved reflectance spectroscopy. *Medical physics* 1995; 22: 1209-1217.

129 Favilla CG, Carter S, Hartl B, Gitlevich R, Mullen MT, Yodh AG *et al*. Validation of the Openwater wearable optical system: cerebral hemodynamic monitoring during a breath hold maneuver. *medRxiv : the preprint server for health sciences* 2023.

130 Hillman EMC, Hebden JC, Schmidt FEW, Arridge SR, Schweiger M, Dehghani H *et al*. Calibration techniques and datatype extraction for time-resolved optical tomography. *Review of Scientific Instruments* 2000; 71: 3415-3427.

131 Liebert A, Wabnitz H, Steinbrink J, Obrig H, Möller M, Macdonald R *et al*. Time-resolved multidistance near-infrared spectroscopy of the adult head: intracerebral and extracerebral absorption changes from moments of distribution of times of flight of photons. *Appl Opt* 2004; 43: 3037-3047.

132 Szkulmowski M, Wojtkowski M. Averaging techniques for OCT imaging. *Opt Express* 2013; 21: 9757-9773.

133 Mazumder D, Wu MM, Ozana N, Tamborini D, Franceschini MA, Carp SA. Optimization of time domain diffuse correlation spectroscopy parameters for measuring brain blood flow. *Neurophotonics* 2021; 8: 035005.

134 Buxton RB, Wong EC, Frank LR. Dynamics of blood flow and oxygenation changes during brain activation: the balloon model. *Magn Reson Med* 1998; 39: 855-864.

135 Friston KJ, Mechelli A, Turner R, Price CJ. Nonlinear Responses in fMRI: The Balloon Model, Volterra Kernels, and Other Hemodynamics. *NeuroImage* 2000; 12: 466-477.

136 Logothetis NK, Pauls J, Augath M, Trinath T, Oeltermann A. Neurophysiological investigation of the basis of the fMRI signal. *Nature* 2001; 412: 150-157.

137 Neuroimaging WTCf. SPM12: Statistical Parametric Mapping. University College London, 2014.

138 Evans AC, Collins DL, Mills SR, Brown ED, Kelly RL, Peters TM. 3D statistical neuroanatomical models from 305 MRI volumes. *1993 IEEE Conference Record Nuclear Science Symposium and Medical Imaging Conference*, 1993, pp 1813-1817 vol.1813.

139 Liu P, Huang H, Rollins N, Chalak LF, Jeon T, Halovanic C *et al*. Quantitative assessment of global cerebral metabolic rate of oxygen (CMRO2) in neonates using MRI. *NMR Biomed* 2014; 27: 332-340.

140 Alderliesten T, De Vis JB, Lemmers PMA, van Bel F, Benders MJNL, Hendrikse J *et al*. Simultaneous quantitative assessment of cerebral physiology using respiratory-calibrated MRI and near-infrared spectroscopy in healthy adults. *NeuroImage* 2014; 85: 255-263.

141 Hashem M, Zhang Q, Wu Y, Johnson TW, Dunn JF. Using a multimodal near-infrared spectroscopy and MRI to quantify gray matter metabolic rate for oxygen: A hypothermia validation study. *NeuroImage* 2020; 206: 116315.

142 Davis TL, Kwong KK, Weisskoff RM, Rosen BR. Calibrated functional MRI: Mapping the dynamics of oxidative metabolism. *Proceedings of the National Academy of Sciences of the United States of America* (Article) 1998; 95: 1834-1839.

143 Hoge RD, Atkinson J, Gill B, Crelier GR, Marrett S, Pike GB. Linear coupling between cerebral blood flow and oxygen consumption in activated human cortex. *Proceedings of the National Academy of Sciences of the United States of America* (Article) 1999; 96: 9403-9408.

144 Fernández-Seara MA, Rodgers ZB, Englund EK, Wehrli FW. Calibrated bold fMRI with an optimized ASL-BOLD dual-acquisition sequence. *NeuroImage* 2016; 142: 474-482.

145 Rodgers ZB, Detre JA, Wehrli FW. MRI-based methods for quantification of the cerebral metabolic rate of oxygen. *Journal of Cerebral Blood Flow & Metabolism* 2016; 36: 1165-1185.

146 Gauthier CJ, Madjar C, Tancredi FB, Stefanovic B, Hoge RD. Elimination of visually evoked BOLD responses during carbogen inhalation: Implications for calibrated MRI. *NeuroImage* 2011; 54: 1001-1011.

147 Blockley NP, Griffeth VE, Simon AB, Buxton RB. A review of calibrated blood oxygenation level-dependent (BOLD) methods for the measurement of task-induced changes in brain oxygen metabolism. *NMR Biomed* 2013; 26: 987-1003.

148 Custo A, Wells Iii WM, Barnett AH, Hillman EMC, Boas DA. Effective scattering coefficient of the cerebral spinal fluid in adult head models for diffuse optical imaging. *Appl Opt* 2006; 45: 4747-4755.

149 Ashburner J, Friston KJ. Unified segmentation. *NeuroImage* 2005; 26: 839-851.

150 Bihan DL, Breton E, Lallemand D, Aubin ML, Vignaud J, Laval-Jeantet M. Separation of diffusion and perfusion in intravoxel incoherent motion MR imaging. *Radiology* 1988; 168: 497-505.

151 Alison M, Chalouhi GE, Autret G, Balvay D, Thiam R, Salomon LJ *et al*. Use of Intravoxel Incoherent Motion MR Imaging to Assess Placental Perfusion in a Murine Model of Placental Insufficiency. *Investigative Radiology* 2013; 48: 17-23.

152 Einstein A. *Investigations on the Theory of the Brownian Movement*. Dover Publications, 1956.

153 Shiraishi T, Chikui T, Inadomi D, Kagawa T, Yoshiura K, Yuasa K. Evaluation of diffusion parameters and T2 values of the masseter muscle during jaw opening, clenching, and rest. *Acta Radiologica* 2012; 53: 81-86.

154 Bihan DL, Turner R. The capillary network: a link between ivim and classical perfusion. *Magnetic Resonance in Medicine* 1992; 27: 171-178.

155 Lipiński K, Domański G, Bogorodzki P. Coherent flow effects on IVIM-based perfusion measurements: A phantom study in 3 T. *Magnetic Resonance Imaging* 2025: 110533.

156 Cordero-Grande L, Christiaens D, Hutter J, Price AN, Hajnal JV. Complex diffusion-weighted image estimation via matrix recovery under general noise models. *NeuroImage* 2019; 200: 391-404.

157 Veraart J, Novikov DS, Christiaens D, Ades-aron B, Sijbers J, Fieremans E. Denoising of diffusion MRI using random matrix theory. *NeuroImage* 2016; 142: 394-406.

158 Kellner E, Dhital B, Kiselev VG, Reisert M. Gibbs-ringing artifact removal based on local subvoxel-shifts. *Magnetic Resonance in Medicine* 2016; 76: 1574-1581.

159 Tournier JD, Smith R, Raffelt D, Tabbara R, Dhollander T, Pietsch M *et al*. MRtrix3: A fast, flexible and open software framework for medical image processing and visualisation. *NeuroImage* 2019; 202: 116137.

160 Jenkinson M, Beckmann CF, Behrens TEJ, Woolrich MW, Smith SM. FSL. *NeuroImage* 2012; 62: 782-790.

161 Tustison NJ, Avants BB, Cook PA, Zheng Y, Egan A, Yushkevich PA *et al*. N4ITK: Improved N3 Bias Correction. *IEEE Transactions on Medical Imaging* 2010; 29: 1310-1320.

162 Song BAaNTaG. Advanced Normalization Tools. *The Insight Journal* 2009; V1.0.

163 Bihan DL, Turner R, Macfall JR. Effects of intravoxel incoherent motions (IVIM) in steady-state free precession (SSFP) imaging: application to molecular diffusion imaging. *Magnetic Resonance in Medicine* 1989; 10: 324-337.

164 Le Bihan D. Intravoxel Incoherent Motion Perfusion MR Imaging: A Wake-Up Call. *Radiology* 2008; 249: 748-752.

165 Pires T, Priyanka, Kadavigere R, Solomon JM, Pendem S, S PP *et al*. Quantitative estimation of intravoxel incoherent motion parameters in acute ischemic stroke: A Systematic review and meta-analysis. *BMC Med Imaging* 2025; 25: 462.

166 Carp SA, Roche-Labarbe N, Franceschini MA, Srinivasan VJ, Sakadžić S, Boas DA. Due to intravascular multiple sequential scattering, Diffuse Correlation Spectroscopy of tissue primarily measures relative red blood cell motion within vessels. *Biomed Opt Express* 2011; 2: 2047-2054.

167 Rosner B, Glynn RJ, Lee ML. The Wilcoxon signed rank test for paired comparisons of clustered data. *Biometrics* 2006; 62: 185-192.

168 Simon AB, Buxton RB. Understanding the dynamic relationship between cerebral blood flow and the BOLD signal: Implications for quantitative functional MRI. *NeuroImage* 2015; 116: 158-167.

169 Chiacchiaretta P, Cerritelli F, Bubbico G, Perrucci MG, Ferretti A. Reduced Dynamic Coupling Between Spontaneous BOLD-CBF Fluctuations in Older Adults: A Dual-Echo pCASL Study. *Frontiers in Aging Neuroscience* (Original Research) 2018; 10.

170 van der Zande FHR, Hofman PAM, Backes WH. Mapping hypercapnia-induced cerebrovascular reactivity using BOLD MRI. *Neuroradiology* 2005; 47: 114-120.

171 Sleight E, Stringer MS, Marshall I, Wardlaw JM, Thrippleton MJ. Cerebrovascular Reactivity Measurement Using Magnetic Resonance Imaging: A Systematic Review. *Frontiers in Physiology* (Systematic Review) 2021; 12.

172 Rashid A, Santarcangelo EL, Roatta S. Cerebral Blood Flow in Healthy Subjects with Different Hypnotizability Scores. *Brain Sci* 2022; 12.

173 Moroz T, Banaji M, Tisdall M, Cooper CE, Elwell CE, Tachtsidis I. Development of a model to aid NIRS data interpretation: results from a hypercapnia study in healthy adults. *Advances in experimental medicine and biology* 2012; 737: 293-300.

174 Viola S, Viola P, Litterio P, Buongarzone MP, Fiorelli L. Correlation between the arterial pulse wave of the cerebral microcirculation and CBF during breath holding and hyperventilation in human. *Clinical neurophysiology : official journal of the International Federation of Clinical Neurophysiology* 2012; 123: 1931-1936.

175 Mogharari N, Kacprzak M, Lipinski K, Liebert A, Wojtkiewicz S. Correlation of Hemodynamic Responses Measured on Human Head by Diffuse Correlation Spectroscopy and BOLD MRI. *IEEE Journal of Selected Topics in Quantum Electronics* 2025; 31: 1-15.

176 Posse S, Olthoff U, Weckesser M, Jäncke L, Müller-Gärtner HW, Dager SR. Regional dynamic signal changes during controlled hyperventilation assessed with blood oxygen level-dependent functional MR imaging. *AJNR Am J Neuroradiol* 1997; 18: 1763-1770.

177 Kastrup A, Li TQ, Takahashi A, Glover GH, Moseley ME. Functional magnetic resonance imaging of regional cerebral blood oxygenation changes during breath holding. *Stroke* 1998; 29: 2641-2645.

178 Li TQ, Kastrup A, Takahashi AM, Moseley ME. Functional MRI of human brain during breath holding by BOLD and FAIR techniques. *Neuroimage* 1999; 9: 243-249.

179 Solich-Talanda M, Żebrowska A, Mikołajczyk R, Kostorz-Nosal S, Ziora D, Jastrzębski D *et al*. Effect of Apnea-Induced Hypoxia on Cardiovascular Adaptation and Circulating Biomarkers of Oxidative Stress in Elite Breath-Hold Divers. *Frontiers in Physiology* (Original Research) 2021; 12.

180 Ratmanova P, Semenyuk R, Popov D, Kuznetsov S, Zelenkova I, Napalkov D *et al*. Prolonged dry apnoea: effects on brain activity and physiological functions in breath-hold divers and non-divers. *European Journal of Applied Physiology* 2016; 116: 1367-1377.

181 Naganawa S, Norris DG, Zysset S, Mildner T. Regional differences of fMR signal changes induced by hyperventilation: Comparison between SE-EPI and GE-EPI at 3-T. *Journal of Magnetic Resonance Imaging* (Article) 2002; 15: 23-30.

182 Haddon A, Kanhai J, Nako O, Smith TG, Hodkinson PD, Pollock RD. Cardiorespiratory Responses to Voluntary Hyperventilation During Normobaric Hypoxia. *Aerospace Medicine and Human Performance* 2023; 94: 59-65.

183 Solis-Barquero SM, Echeverria-Chasco R, Calvo-Imirizaldu M, Cacho-Asenjo E, Martinez-Simon A, Vidorreta M *et al*. Breath-Hold Induced Cerebrovascular Reactivity Measurements Using Optimized Pseudocontinuous Arterial Spin Labeling. *Frontiers in Physiology* (Original Research) 2021; 12.

184 Vogt KM, Ibinson JW, Schmalbrock P, Small RH. Comparison between end-tidal CO_2 and respiration volume per time for detecting BOLD signal fluctuations during paced hyperventilation. *Magn Reson Imaging* 2011; 29: 1186-1194.

185 Chen JJ, Pike GB. MRI measurement of the BOLD-specific flow-volume relationship during hypercapnia and hypocapnia in humans. *Neuroimage* 2010; 53: 383-391.

186 Paschoal AM, Leoni RF, dos Santos AC, Paiva FF. Intravoxel incoherent motion MRI in neurological and cerebrovascular diseases. *NeuroImage: Clinical* 2018; 20: 705-714.

187 Podgórska J, Pasicz K, Skrzyński W, Gołębiewski B, Kuś P, Jasieniak J *et al*. Perfusion-Diffusion Ratio: A New IVIM Approach in Differentiating Solid Benign and Malignant Primary Lesions of the Liver. *Biomed Res Int* 2022; 2022: 2957759.

188 Sudakou A, Yang L, Wabnitz H, Wojtkiewicz S, Liebert A. Performance of measurands in time-domain optical brain imaging: depth selectivity versus contrast-to-noise ratio. *Biomed Opt Express* 2020; 11: 4348-4365.

189 Robinson MB, Renna M, Ozana N, Martin AN, Otic N, Carp SA *et al*. Portable, high speed blood flow measurements enabled by long wavelength, interferometric diffuse correlation spectroscopy (LW-iDCS). *Sci Rep* 2023; 13: 8803.

190 Selb J, Boas DA, Chan S-T, Evans KC, Buckley EM, Carp SA. Sensitivity of near-infrared spectroscopy and diffuse correlation spectroscopy to brain hemodynamics: simulations and experimental findings during hypercapnia. *Neurophotonics* 2014; 1.

191 Pagliazzi M, Sekar SKV, Colombo L, Martinenghi E, Minnema J, Erdmann R *et al*. Time domain diffuse correlation spectroscopy with a high coherence pulsed source: in vivo and phantom results. *Biomed Opt Express* 2017; 8: 5311-5325.

192 Cheng X, Chen H, Sie EJ, Marsili F, Boas DA. Development of a Monte Carlo-wave model to simulate time domain diffuse correlation spectroscopy measurements from first principles. *J Biomed Opt* 2022; 27.

193 Re R, Contini D, Zucchelli L, Torricelli A, Spinelli L. Effect of a thin superficial layer on the estimate of hemodynamic changes in a two-layer medium by time domain NIRS. *Biomed Opt Express* 2016; 7: 264-278.

194 Zucchelli L, Contini D, Re R, Torricelli A, Spinelli L. Method for the discrimination of superficial and deep absorption variations by time domain fNIRS. *Biomedical Optics Express* 2013; 4: 2893-2910.

195 Okada E, Delpy DT. Near-infrared light propagation in an adult head model. II. Effect of superficial tissue thickness on the sensitivity of the near-infrared spectroscopy signal. *Appl Opt* 2003; 42: 2915-2921.

196 Sousa I, Vilela P, Figueiredo P. Reproducibility of hypocapnic cerebrovascular reactivity measurements using BOLD fMRI in combination with a paced deep breathing task. *Neuroimage* 2014; 98: 31-41.

197 Mesquita RC, Schenkel SS, Minkoff DL, Lu X, Favilla CG, Vora PM *et al*. Influence of probe pressure on the diffuse correlation spectroscopy blood flow signal: extra-cerebral contributions. *Biomed Opt Express* 2013; 4: 978-994.

198 Ozana N, Zavriyev AI, Mazumder D, Robinson M, Kaya K, Blackwell M *et al*. Superconducting nanowire single-photon sensing of cerebral blood flow. *Neurophotonics* 2021; 8: 035006.

199 Makiranta MJ, Ruohonen J, Suominen K, Sonkajarvi E, Salomaki T, Kiviniemi V *et al*. BOLD-contrast functional MRI signal changes related to intermittent rhythmic delta activity in EEG during voluntary hyperventilation-simultaneous EEG and fMRI study. *Neuroimage* 2004; 22: 222-231.

200 Bartlett MF, Oneglia AP, Ricard MD, Siddiqui A, Englund EK, Buckley EM *et al*. DCS blood flow index underestimates skeletal muscle perfusion in vivo: rationale and early evidence for the NIRS-DCS perfusion index. *J Biomed Opt* 2024; 29: 020501.

201 Halani S, Kwinta JB, Golestani AM, Khatamian YB, Chen JJ. Comparing cerebrovascular reactivity measured using BOLD and cerebral blood flow MRI: The effect of basal vascular tension on vasodilatory and vasoconstrictive reactivity. *NeuroImage (Orlando, Fla)* 2015; 110: 110-123.

202 Shen Q, Ren H, Duong TQ. CBF, BOLD, CBV, and CMRO2 fMRI signal temporal dynamics at 500-msec resolution. *Journal of Magnetic Resonance Imaging* 2008; 27: 599-606.

203 van Horen TWP, Siero JCW, Bhogal AA, Petridou N, Báez-Yáñez MG. Microvascular Specificity of Spin Echo BOLD fMRI: Impact of EPI Echo Train Length. *bioRxiv* 2023.

204 Yu X, Glen D, Wang S, Dodd S, Hirano Y, Saad Z *et al*. Direct imaging of macrovascular and microvascular contributions to BOLD fMRI in layers IV-V of the rat whisker-barrel cortex. *Neuroimage* 2012; 59: 1451-1460.

205 Jones M, Berwick J, Hewson-Stoate N, Gias C, Mayhew J. The effect of hypercapnia on the neural and hemodynamic responses to somatosensory stimulation. *NeuroImage* 2005; 27: 609-623.

206 Tsuda Y, Kimura K, Yoneda S, Hartmann A, Etani H, Hashikawa K *et al*. Effect of Hypocapnia on Cerebral Oxygen Metabolism and Blood Flow in Ischemic Cerebrovascular Disorders. *European Neurology* 2008; 27: 155-163.

207 Chen JJ, Pike GB. Global cerebral oxidative metabolism during hypercapnia and hypocapnia in humans: implications for BOLD fMRI. *Journal of cerebral blood flow and metabolism : official journal of the International Society of Cerebral Blood Flow and Metabolism* 2010; 30: 1094-1099.

208 Durduran T, Zhou C, Buckley E, Kim M, Yu G, Choe R *et al*. Optical measurement of cerebral hemodynamics and oxygen metabolism in neonates with congenital heart defects. *Journal of Biomedical Optics* 2010; 15: 037004.

209 Zappe AC, Uludağ K, Oeltermann A, Uğurbil K, Logothetis NK. The Influence of Moderate Hypercapnia on Neural Activity in the Anesthetized Nonhuman Primate. *Cerebral Cortex* 2008; 18: 2666-2673.

210 Hua J, Stevens RD, Huang AJ, Pekar JJ, van Zijl PC. Physiological origin for the BOLD poststimulus undershoot in human brain: Vascular compliance versus oxygen metabolism. *Journal of Cerebral Blood Flow & Metabolism* 2011; 31: 1599-1611.

211 Lin A-L, Fox PT, Yang Y, Lu H, Tan L-H, Gao J-H. Evaluation of MRI models in the measurement of CMRO2 and its relationship with CBF. *Magnetic Resonance in Medicine* 2008; 60: 380-389.

212 Jones M, Berwick J, Mayhew J. Changes in Blood Flow, Oxygenation, and Volume Following Extended Stimulation of Rodent Barrel Cortex. *NeuroImage* 2002; 15: 474-487.

213 Chiarelli PA, Bulte DP, Piechnik S, Jezzard P. Sources of systematic bias in hypercapnia-calibrated functional MRI estimation of oxygen metabolism. *NeuroImage* 2007; 34: 35-43.

214 Ferré JC, Bannier E, Raoult H, Mineur G, Carsin-Nicol B, Gauvrit JY. Arterial spin labeling (ASL) perfusion: Techniques and clinical use. *Diagnostic and Interventional Imaging* 2013; 94: 1211-1223.

215 Mueller BA, Lim KO, Hemmy L, Camchong J. Diffusion MRI and its Role in Neuropsychology. *Neuropsychol Rev* 2015; 25: 250-271.

216 Chabert S, Verdu J, Huerta G, Montalba C, Cox P, Riveros R *et al*. Impact of b-Value Sampling Scheme on Brain IVIM Parameter Estimation in Healthy Subjects. *Magnetic Resonance in Medical Sciences* 2020; 19: 216-226.

217 Englund EK, Reiter DA, Shahidi B, Sigmund EE. Intravoxel Incoherent Motion Magnetic Resonance Imaging in Skeletal Muscle: Review and Future Directions. *J Magn Reson Imaging* 2022; 55: 988-1012.

218 Cho GY, Kim S, Jensen JH, Storey P, Sodickson DK, Sigmund EE. A versatile flow phantom for intravoxel incoherent motion MRI. *Magnetic Resonance in Medicine* 2012; 67: 1710-1720.

219 Müller MF, Prasad PV, Edelman RR. Can the IVIM model be used for renal perfusion imaging? *European Journal of Radiology* 1998; 26: 297-303.

220 Boas DA, Sakadzic S, Selb J, Farzam P, Franceschini MA, Carp SA. Establishing the diffuse correlation spectroscopy signal relationship with blood flow. *Neurophotonics* 2016; 3: 031412.

221 Englund EK, Rodgers ZB, Langham MC, Mohler ER, 3rd, Floyd TF, Wehrli FW. Measurement of skeletal muscle perfusion dynamics with pseudo-continuous arterial spin labeling (pCASL): Assessment of relative labeling efficiency at rest and during hyperemia, and comparison to pulsed arterial spin labeling (PASL). *J Magn Reson Imaging* 2016; 44: 929-939.

222 Hornikel B, Saffold KS, Mota JA, Esco MR, Fedewa MV, Wind SA *et al*. Acute Blood Flow Responses to Varying Blood Flow Restriction Pressures in the Lower Limb. *Int J Exerc Sci* 2023; 16: 118-128.

223 Meeus EM, Novak J, Withey SB, Zarinabad N, Dehghani H, Peet AC. Evaluation of intravoxel incoherent motion fitting methods in low-perfused tissue. *J Magn Reson Imaging* 2017; 45: 1325-1334.

224 Jalnefjord O, Björkman-Burtscher IM. Comparison of methods for intravoxel incoherent motion parameter estimation in the brain from flow-compensated and non-flow-compensated diffusion-encoded data. *Magnetic Resonance in Medicine* 2024; 92: 303-318.

225 Wu W-C, Chen Y-F, Tseng H-M, Yang S-C, My P-C. Caveat of measuring perfusion indexes using intravoxel incoherent motion magnetic resonance imaging in the human brain. *European Radiology* 2015; 25: 2485-2492.

226 Suo S, Zhang L, Tang H, Ni Q, Li S, Mao H *et al*. Evaluation of skeletal muscle microvascular perfusion of lower extremities by cardiovascular magnetic resonance arterial spin labeling, blood oxygenation level-dependent, and intravoxel incoherent motion techniques. *Journal of Cardiovascular Magnetic Resonance* 2018; 20: 18.

227 Loenneke JP, Pujol TJ. The Use of Occlusion Training to Produce Muscle Hypertrophy. *Strength & Conditioning Journal* 2009; 31: 77-84.

228 Junejo RT, Ray CJ, Marshall JM. Cuff inflation time significantly affects blood flow recorded with venous occlusion plethysmography. *Eur J Appl Physiol* 2019; 119: 665-674.

229 Fortrat J-O, de Holanda A, Zuj K, Gauquelin-Koch G, Gharib C. Altered Venous Function during Long-Duration Spaceflights. *Frontiers in Physiology* (Original Research) 2017; Volume 8 - 2017.

230 Kamshilin AA, Zaytsev VV, Mamontov OV. Novel contactless approach for assessment of venous occlusion plethysmography by video recordings at the green illumination. *Scientific Reports* 2017; 7: 464.

231 Jones S, Chiesa ST, Chaturvedi N, Hughes AD. Recent developments in near-infrared spectroscopy (NIRS) for the assessment of local skeletal muscle microvascular function and capacity to utilise oxygen. *Artery Res* 2016; 16: 25-33.

232 Hunt JE, Stodart C, Ferguson RA. The influence of participant characteristics on the relationship between cuff pressure and level of blood flow restriction. *Eur J Appl Physiol* 2016; 116: 1421-1432.

233 Zhang Q, Wang YX, Ma HT, Yuan J. Cramér-Rao bound for Intravoxel Incoherent Motion Diffusion Weighted Imaging fitting. *2013 35th Annual International Conference of the IEEE Engineering in Medicine and Biology Society (EMBC)*, 2013, pp 511-514.

234 Englund EK, Berry DB, Behun JJ, Ward SR, Frank LR, Shahidi B. IVIM Imaging of Paraspinal Muscles Following Moderate and High-Intensity Exercise in Healthy Individuals. *Frontiers in Rehabilitation Sciences* (Original Research) 2022; Volume 3 - 2022.

235 Le Bihan D, Johansen-Berg H. Diffusion MRI at 25: exploring brain tissue structure and function. *Neuroimage* 2012; 61: 324-341.

236 Diez-Silva M, Dao M, Han J, Lim CT, Suresh S. Shape and Biomechanical Characteristics of Human Red Blood Cells in Health and Disease. *MRS Bull* 2010; 35: 382-388.

237 Higgins JM, Eddington DT, Bhatia SN, Mahadevan L. Statistical Dynamics of Flowing Red Blood Cells by Morphological Image Processing. *PLOS Computational Biology* 2009; 5: e1000288.

238 Mesquita RC, Durduran T, Yu G, Buckley EM, Kim MN, Zhou C *et al*. Direct measurement of tissue blood flow and metabolism with diffuse optics. *Philosophical transactions Series A, Mathematical, physical, and engineering sciences* 2011; 369: 4390-4406.